Dynamically responsive scaffolds produced by additive manufacturing

Henry Wynand Huysamen

Dissertation submitted in fulfilment of the requirements for the degree Master of Engineering in Mechanical Engineering in the Department of Mechanical and Mechatronics Engineering, Faculty of Engineering, Built Environment and Information Technology at Central University of Technology, Free State

Supervisor: **Dr Ina Yadroitsava, Ph.D.**

Co-supervisors: **Prof Ihar Yadroitsau, D.Eng.**

Prof. Anton du Plessis. Ph.D.

Bloemfontein

January 2022

DECLARATION OF INDEPENDENT WORK

I, Henry Wynand Huysamen, identity number _____ and student number _____, do hereby declare that this research project submitted to Central University of Technology, Free State for the Master of Engineering in Mechanical Engineering degree, is my own independent work; and complies with the Code of Academic Integrity, as well as other relevant policies, procedures, rules and regulations of Central University of Technology, Free State; and has not been submitted previously to any institution by myself or any other person in fulfilment of the requirements for the attainment of any qualification.

Signature of student: 

Date: 22 June 2022

ACKNOWLEDGEMENTS

I would like to express my deepest thanks to Prof Ihar Yadroitsau and Dr Ina Yadroitsava for their assistance, guidance, and support for this dissertation. I am truly grateful to have worked with them and for all that I learnt from them. I would also like to thank Prof Anton du Plessis and Miss Muofhe Tshibalanganda from Stellenbosch University for their guidance and assistance with the CT scanning and data processing of samples.

My sincere thanks to the staff at CRPM, PDTS and CUT for allowing me to learn from them, assisting me with my specimens and giving me time to work on my dissertation. A special thanks to Dr Dean-Paul Kouprianoff for assisting with the tensile testing of the specimens.

A special word of appreciation to the following funding sources without which this research would not have been possible: The South African Research Chairs Initiative of the Department of Science and Innovation and the National Research Foundation of South Africa (Grant № 97994) and the Collaborative Program in Additive Manufacturing (Contract № CSIR-NLC-CPAM-15-MOA-CUT-01) of the Department of Science and Innovation.

I would also like to thank my family and friends for their continued love and support, which carried me through. I would like to especially thank my mother, Hannelie Huysamen, for always believing in me, supporting me and pushing me to do greater things. My sincere thanks to Allan Kinnear for his mentorship and guidance.

"With man this is impossible, but with God all things are possible."

-Matthew 19:26-

ABSTRACT

Additive manufacturing (AM) and design methodology of compliant mechanisms, topology optimisation, lattice structures, metamaterials, etc. allows for the production of complex customised components with very specific properties. One of these types of components is dynamically responsive scaffolds (DRS), made of thin geometric structures that adjust mechanical behaviour to the required loading and direction. This work presents design, numerical simulation, production, and testing of DRS structures as two-dimensional scaffoldings. The scaffoldings were printed in different directions to compare the isotropic behaviour of the AM samples for tensile tests. The methodology for DRS physical testing was demonstrated. The auxetic behaviour of the samples were also studied. Auxetic behaviour will be highly beneficial for DRS as it would allow the DRS to distribute the force more evenly in the event of an impact on the scaffolding. Three series of experiments and numerical simulations were done. First, the scaffoldings were produced from ABS (acrylonitrile butadiene styrene) filament using fused deposition modelling (FDM) system to obtain a basic understanding of DRS mechanical behaviour. Second, the polyamide (PA 2200) specimens were produced with selective laser sintering (SLS) machine. The SLS scaffolding specimens were tensile tested that gave a reading on the tensile force experienced by the specimens during elongation. The data from the tensile tests were then processed into force-over-displacement graphs, and the results were studied. Videos of the tensile tests were also taken to examine the deformation of the specimens as they elongated. Finally, two of the most promising designs were selected and fabricated in a metallic material (Ti6Al4V alloy) by laser powder bed fusion (L-PBF). The physical testing and numerical simulations of Ti6Al4V DRS samples were compared and discussed.

This study aims to lay a foundation for the development of DRS, which could one day be used as medical implants that require specific mechanical properties and behaviour that would otherwise not be possible. An essential application for designed DRS could be a cranial implant that can grow with the patient removing the need for future surgeries to replace the implant due to the growth of the skull until it is fully developed. The compliance of the scaffolding, the stiffness, and the support perpendicular to the growth direction make designed DRS especially promising for this application.

Keywords: Additive manufacturing; laser powder bed fusion; implants; dynamically responsive scaffolds; tensile tests; auxetic behaviour.

TABLE OF CONTENTS

LIST OF FIGURES

LIST OF TABLES

GLOSSARY

ABS	Acrylonitrile Butadiene Styrene
AI	Artificial Intelligence
AM	Additive Manufacturing
CAD	Computer-aided Design
CNC	Computer Numerical Controlled
CT	Computer Tomography
DMLS	Direct Laser Metal Sintering
DRS	Dynamically Responsive Scaffolding
ELI	Extra Low Interstitials
EOS	Electro Optical System
FEA	Finite Element Analysis
HA	Hydroxyapatite
IM	Injection Moulding
L-PBF	Laser Powder Bed Fusion
MEM	Melted Extrusion Modelling
PA	Polyamide
RP	Rapid Prototyping
SEM	Scanning Electron Microscope
SLA	Stereolithography
SLM	Selective Laser Melting
SLS	Selective Laser Sintering
UTS	Ultimate Tensile Strength
YS	Yield Strength

CHAPTER 1: INTRODUCTION

1.1. Background

From the birth of the second industrial revolution, people have been building machines to increase the productivity and efficiency of the industries and increase the quality of life for people worldwide. However, the capabilities of these machines were limited by the complexity of the object that they could fabricate. Even with the advancement of computer numerical controlled (CNC) machines, there were still physical restrictions. For this reason, complicated parts needed to be divided into more parts that could be manufactured by these machines. With the development of Additive Manufacturing (AM), the capability to fabricate objects with highly complex geometries was made possible. This manufacturing process allowed for mechanisms that once consisted of hundreds of parts to be fabricated with as little as one part; this is also commonly known as part consolidation. The reduction in part count also reduces the weight and cost of mechanisms and increases their lifespan as there are fewer moving parts.

This capability of AM to fabricate complex structures with the help of computer-aided design (CAD) proved to be very promising in the manufacturing, aerospace, and medical industries. In the manufacturing and aerospace industries, this allowed parts to be optimised using computer algorithms and artificial intelligence (AI), which reduces the weight of the part even more and can, in some cases, increase the strength of the part. In the medical industry, this significantly increased the number of high-quality patient-specific implants that could be fabricated at a lower cost in most cases. By combining computer tomography (CT) scans with CAD software, pre-operational models and jigs could be fabricated before the surgery resulting in a process that reduces the time of the surgery, as the doctors would not have to modify a generic implant to fit a specific patient or to guess where to drill the screw holes or to cut the bone; they would have made the decisions prior to the procedure and under less pressure and with more time.

Laser powder bed fusion (L-PBF), also known as selective laser melting (SLM), direct metal laser sintering (DMLS), LaserCusing and selective laser sintering (SLS), melts powder material layer by layer with a laser beam.

SLS is one of the powder bed fusion AM processes most commonly used for rapid prototyping, and the term is mainly used for plastic materials (Kumar, 2003). It was conceptualised in 1979 by R.F. Housholder, who described the process as depositing a planar layer of the material,

then solidifying a portion of the area of the layer by using a controlled heat scanning process and then repeating the process sequentially to form a 3D object (Housholder, 1981). The SLS process was patented by Dr Carl Deckard and Dr Joe Beaman in 1986; they were later involved in the start-up company DTM which was established to design and build the first commercial SLS machine (Deckard, 1989). The same process applied to metals, called selective laser melting (SLM), was patented in 1995 by the Fraunhofer Institute for Laser Technology ILT (Meiners, 1998; Yadroitsev et al., 2021).

1.2. The aim of the study

The study aims to examine different L-PBF scaffoldings with specific geometries. These geometries allow the scaffolding to behave in such a manner that it can expand or contract in a two-dimensional (2D) plane while remaining rigid in the axis perpendicular to that plane. It thus creates a dynamically responsive structure (DRS) that can adapt to its surroundings, taking the form that is required within limits while at the same time remaining rigid enough to provide support or protection. This study aims to create a fundamental understanding of designing DRS for L-PBF.

1.3. The scope of the study

This research study is concerned with the development and validation of a scaffolding design that can behave dynamically as described above.

1.4. Research methodology

In the study, polyamide specimens were first used to observe the behaviour of different geometries; the most promising designs were then fabricated from Ti6Al4V to obtain the final design. Polymer test specimens were tensile tested to obtain accurate mechanical properties of the PA 2200 material (Figure 1). The specimens were manufactured using a specific batch of PA 2200 powder, machine and machine parameters to fabricate the specimens; the same process was later followed to fabricate the polymer prototypes. This ensures consistency in the tensile test data.

Several different patterns and structures were researched and conceptualised. These concepts were derived from metamaterial, mainly negative Poisson's ratio theory and compliant mechanisms theory. The concepts were drawn using SolidWorks 2019 CAD software to create

a 3D model used for the 3D printing. Subsequently, five designs were chosen to be fabricated from polymer on an EOS machine from PA 2200. The polymer prototypes were manufactured in multiple directions and tensile tested to obtain the mechanical properties.

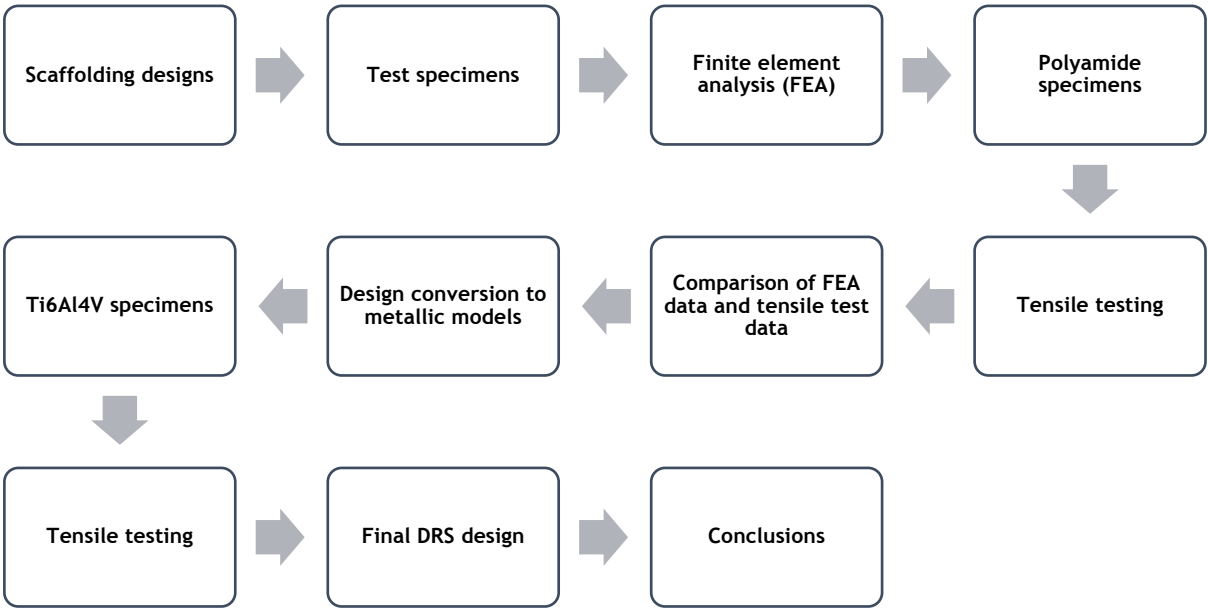

Figure 1. Layout of the research methodology.

The mechanical property data obtained from the tensile testing of the test specimens were then used to run finite element analysis (FEA) on the 3D model designs. The numerical simulation data from the FEA was compared to the data obtained from the tensile testing of the polymer prototypes. This assisted in making modifications to the designs to optimise the scaffolding structures. The behaviour observed in the polymer prototypes will also be beneficial in creating newer and improved scaffolding designs.

The mechanical properties of the L-PBF Ti6Al4V alloy were then applied to the 3D models using FEA to simulate two selected DRS designs. Once the Ti6Al4Vscaffoldings were fabricated, they underwent the same tensile testing as the polymer prototypes. This data was then used to compare the FEA data and the actual scaffolding behaviour to investigate the accuracy of the FEA data. The tensile testing of the Ti6Al4V also provided the scaffoldings' mechanical properties, allowing for more accurate conclusions to be reached on the benefits and disadvantages of the DRS L-PBF scaffolding.

1.5. Overview of the dissertation

The following outline defines the dissertation structure:

- Chapter 1 gives an introduction and background to the study and describes the aim, scope, and research methodology.
- Chapter 2 is an in-depth review conducted on the conception of AM, compliant mechanisms and metamaterials and how they can be combined to create DRS.
- Chapter 3 describes the materials utilised in the study and elaborates further on the research methodology and design of experiments.
- Chapter 4 highlights the conceptualisation, material property validation and numerical simulation of the initial plastic scaffolding designs and optimising the designs for fabrication.
- Chapter 5 describes the numerical simulations, characterisation and mechanical properties of the Ti6Al4V scaffoldings.
- Chapter 6 concludes the study. This chapter summarises and discusses the investigation and highlights the future work.

1.6. Expected contributions

This study validates the concept of DRS produced by AM and lays the fundamental understanding of designing DRS. The experimental procedures and preliminary results of this study will guide future developments in applications of DRS and further in-depth studies on DRS objects manufactured by AM.

1.7. Publications and presentations to date

Journal paper

- H.W. Huysamen, W.A. Kinnear, T.E. Fonternel, E.W. Turton, I. Yadroitsava and I. Yadroitsev. 3D printed laryngoscope for endotracheal intubation. *South African Journal of Industrial Engineering*, November 2020 Vol 31(3) Special Edition, pp 209-217. http://dx.doi.org/10.7166/31-3-2446

Presentations

- H.W. Huysamen, I. Yadroitsava, A. du Plessis and I. Yadroitsev. Dynamically responsive scaffolds produced by additive manufacturing. Pre-conference seminar, 21st

RAPDASA Annual International Conference, 4–6 November 2020, Bloemfontein-Stellenbosch, South Africa.

- H.W. Huysamen, W.A. Kinnear and D.J. de Beer. Optimization of fused deposition modelling (FDM) production strategies of plastic components. 21st RAPDASA Annual International Conference, 4–6 November 2020, Bloemfontein-Stellenbosch, South Africa.

CHAPTER 2: LITERATURE REVIEW

2.1. Additive manufacturing

AM is a fitting name to describe a manufacturing process where the material is added to fabricate a 3D object, as opposed to subtractive manufacturing, where a solid block of pre-processed material is taken and machined away to form the final object. Generally, AM works by building an object by taking raw material and processing it into the required shape layer-by-layer, whether extruding or solidifying the pre-deposited raw material. Due to the AM layer-upon-layer manufacturing process, sections that consist of a multitude of parts can be consolidated into one part – resulting in a reduction of weight as well as increasing its lifespan as there are fewer moving parts (Yang et al., 2015; Chen & Frank, 2019; Szymczyk et al., 2020). Commonly, AM technologies use numerical data to construct objects using CAD software or CT scans. AM permits the reduction of weight, cost, and fabrication time. Furthermore, it can change the infill percentage of a part or optimise its topology to give it the most effective strength-to-weight ratio.

AM was first used for rapid prototyping due to the remarkable flexibility of the process. However, these prototypes generally were only used to get a basic idea of the part and its size, shape and feel because the AM layer-upon-layer fabrication process results in different mechanical properties to that of more commonly used large scale production processes such an injection moulded part (Vayre et al., 2012; Kruth et al., 1998). As consumer AM machines have become accessible, more service providers are using them to fabricate parts for their creations, regardless of the drawbacks of the layer-upon-layer part strength, to take advantage of the ease of fabrication and producing intricate parts very accurately (Bourell, 2016). The aerospace, medical and other industries have turned to AM to fabricate usable parts as the AM process can produce parts that no other manufacturing process can do (Vayre et al., 2012; Dana et al., 2019). Production of AM parts by independent service providers is growing each year (Figure 2), and estimated revenue of $5.3 billion was generated in this sector in 2020 (Wohlers Report, 2021).

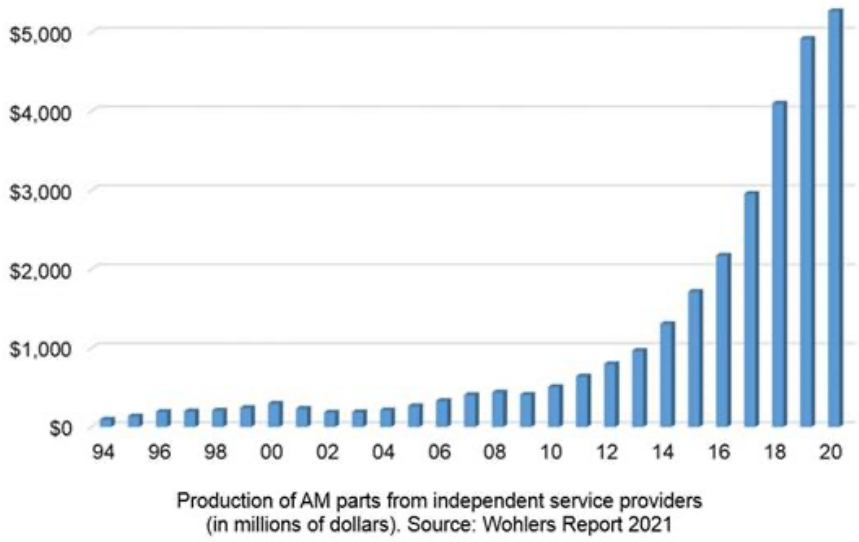

Figure 2. Production of AM parts from independent service providers (in millions of dollars) (Wohlers Report, 2021).

2.1.1. AM of polymer materials

There are seven broad categories of AM: material jetting, binder jetting, directed energy deposition, sheet lamination, vat photopolymerisation, powder bed fusion and material extrusion (ASTM, 2015; Szymczyk et al., 2020). The three most used processes for polymer printing are:

- Material extrusion (also commonly known as fused deposition modelling, FDM) selectively extrudes plastic filament in adjacent lines to form a layer. Once the layer is completed, it extrudes the plastic filament onto the previously extruded layer, thus forming a three-dimensional (3D) object layer upon layer.
- Vat photopolymerisation, also commonly referred to as stereolithography (SLA), is the process whereby light is used to solidify liquid in a vat onto a base. The base is then either submerged into the vat or retracted away to facilitate the light solidifying the next layer.
- Powder bed fusion of polymers is commonly referred to as selective laser sintering (SLS). The term powder bed fusion refers to the process whereby the entire build area is filled with the raw material a layer at a time. A heat source is used between layers to fuse adjacent particles into a specific shape/area. This process is then repeated between each layer to form the 3D object. The SLS process uses a laser explicitly to selectively sinter particles to fuse adjacent particles, as suggested in the name.

Unlike most metal AM, the SLS process does not require supports to print features that pass a certain angle as the entire build volume is filled with material and the raw material that is left acts as the support structure. SLS machines also heat the powder material to a point below the melting temperature. This makes it easier for the laser to melt the raw powder and reduces the thermal warpage. Thermal warpage is the deformation of a part caused by internal stresses resulting from heating and cooling of different areas of the part. The advantages of the SLS process, such as preheating and non-support manufacturing, allow for more complex parts to be fabricated than most other AM processes and does not cost more in material and power to run the machine (Bose et al., 2019; Szymczyk et al., 2020).

Initially, AM used plastics as it proved the simplest to heat and fuse. In the process, the material is heated to a semi-melted state allowing the material to bind with adjacent material as polymers generally have a lower melting temperature than most materials. As a result, polymer parts fabricated by the AM process are mainly used for rapid prototyping (RP) and not for final usable parts. Also, parts have built-in weaknesses due to the fabrication process; the material does not entirely fuse between layers because of the layer-upon-layer process, allowing for delamination. Delamination is when parts linearly split/fail between two layers, resulting in a part that does not have the same properties in all directions counter to a part that was, for example, injection moulded (Zindani et al., 2019).

Through the years, material science has resulted in materials used for AM having much better mechanical, thermal and dimensional properties and a large variety of AM materials that can imitate a range of different properties. Combining different materials with polymers, for example, carbon nanofibres could substantially increase the strength of the material without considerably increasing the weight of the fabricated part (Szymczyk et al., 2020; Zindani et al., 2019). With the development of more eco-friendly and biocompatible polymers (biopolymers), plastic AM parts nowadays are widely used in the biomedical field (Daminabo et al., 2020). 3D printing has progressed to a point where living cells are being used to print complex 3D functional parts. This technology could open the possibility of reducing the need for organ donors as organs can be bioprinted with the patient's own living cells eliminating the risk of the new organ being rejected by the body (Ghilan et al., 2020). This technology is still a long way from being implemented but could save millions of lives when implemented one day.

The implementation of AM and RP in the biomedical field made revolutionary changes to how surgeries are performed and implants are fabricated. The implications include developing biocompatible, biodegradable and bioadaptable materials, commonly known as biopolymers.

These biopolymers can increase the success of an operation and reduce the chance of the body rejecting the implant (Bansal et al., 2020). The advantages of using AM for implants also include higher dimensional accuracy, especially when using CAD and CT scans to create a patient-specific implant that can fit close to perfect (Javaid & Haleem, 2018).

Biopolymers can be broadly classified into two categories: natural and synthetic. They are most commonly used for biomedical scaffolding and tissue engineering in restoration, regeneration or replacement of damaged or defective tissue or even living organs. Table 1 shows some commonly used biopolymer materials. Common examples of tissue engineering are highly porous structures that allow for migration and transportation of oxygen and nutrition, which promote growth (Yaragatti & Patnaik, 2020), bone substitute implants (Bobbert & Zadpoor, 2017), as well as utilising AM to assist with drug delivery (Rovira et al., 2021). Natural biopolymers have excellent biocompatibility and degradability properties, but high cost and mediocre physical, chemical and mechanical properties and their immunogenicity limit their applications (Bose et al., 2019). Biocompatibility is the most important factor when discussing synthetic polymer-based implants.

Table 1: Some common biopolymer materials used in medical applications (Wohlers Report, 2019; Van der Walt & Nsengimana, 2016; Patel et al., 2018; Borzan et al., 2016)

Abbreviation	Biopolymer	Biocompatible/ biodegradable	Usage
PCL/HA	Polycaprolactone/ Hydroxyapatite	Long-term biodegradable	Has excellent biocompatibility and growth promotion for bone cells
PEEK	Polyetheretherketone	Biocompatible	Very strong with excellent mechanical and chemical resistance properties
PMMA	Polymethyl methacrylate	Biocompatible	Transparent thermoplastic that is compatible with human tissue
PA	Polyamide	Biocompatible	Widely used in medical devices

2.1.2. Metal laser powder bed fusion

Metal laser powder bed fusion (L-PBF) is an AM process of fabricating 3D objects and parts from metals and alloys. At the laser beam, the powder materials melt to bind with the adjacent particles. The L-PBF machine scans the laser over the raw material to fuse specific particles into the required shape. After the required shape has been melted, a new layer of raw material is moved onto the previously scanned layer, and the process is repeated with each layer. The smaller the material particles, the thinner the layers, which result in greater detail on the final part. During the laser scanning process, several physical phenomena occur that influence the outcome of the part (Figure 3). The phenomena included the absorption, reflection, radiation and transfer of heat from the laser to the raw powder, the transformation from powder to a liquid phase, the flow of the molten pool due to surface tension and mass transportation, the chemical reactions and gases released (Yadroitsau, 2008).

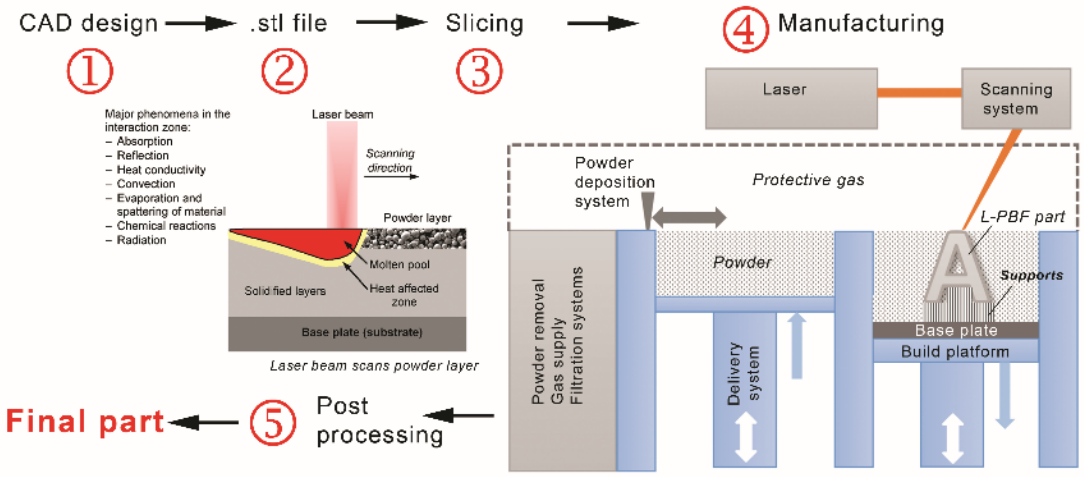

Figure 3. Processes of laser-material interaction in selective laser melting (Yadroitsev et al., 2021).

Due to these phenomena, there are limitations in manufacturing parts with fine detail, such as L-PBF lattice structures. Firstly, the minimum size depends on the laser beam spot size and energy and powder material. Increasing the power can lead to a larger melt pool and deeper penetration, causing the melting process to affect the previous layer. Also, of primary importance is to use optimal process parameters to establish a stable single track. If the laser power is too low or the beam moves too fast, the track will not be continuous and form beads. The formation of the beads is due to the surface tension phenomenon, referred to as the balling effect and can negatively affect the porosity and surface quality of the part (Yadroitsau, 2008; Pal et al., 2019; Zhang et al., 2020). The spot size of the laser and the melting area mainly determine the thickness of the feature. The layer thickness also plays a role in the stability of a

track since having a layer that is too high means the powder will not melt through, and the track will not fuse with the previous layer resulting in a lack of fusion porosity. When printing multiple consecutive tracks (single layer), the correct setup of the hatch distance is essential. The hatch distance is the distance between the centre lines of two tracks (the distance that the laser shifts in printing the next track). If the hatch distance is too small, the tracks are too close. The second track will not have enough powder to melt, and the post-melted material absorbs less of the heat than the raw powder, which can cause the track to dip down at an angle from the first track. This can also influence the properties of the part, result in a longer manufacturing time and impact the cost of production. If the hatch distance is too large, the tracks will not join, and the part density will be low, affecting the mechanical properties (Yadroitsau, 2008; Zhou et al., 2020).

For the fabrication of finely detailed parts, the optimisation of single-track scanning is required. Knowledge about the geometry of single tracks is helpful for fabricating parts with thin walls, but defects can have a more significant impact on these features. It is crucial when designing for L-PBF to take into account that the fine features and dimensions (for example, lattice struts) can vary in the vertical and horizontal direction, and it depends on process parameters, scanning and building strategies (Vilardell et al., 2019). In L-PBF, microstructural defects can occur due to various build environments, processing temperatures, etc. (Kok et al., 2018). It is of utmost importance to ensure that the part is fabricated correctly, as small defects can affect the mechanical properties of the parts (Szymczyk et al., 2020). Thus, producing regular metal lattice structures or fine structures with designed properties using L-PBF requires optimal process parameters and building and scanning strategies to ensure the part meets the required specifications.

L-PBF has drawbacks and limitations, such as the surface quality being quite rough and high residual stress thus requiring post-processing on parts (Yadroitsev et al., 2021; Bellini et al., 2021). The fabrication method of a layer-by-layer process also affects the final mechanical properties resulting in different properties in the vertical and horizontal directions, meaning the parts will be anisotropic. Furthermore, due to the high thermal conductivity of metals and thermal stresses, L-PBF does require supports. In polymer L-PBF, preheating the raw material prevents deformation caused by shrinkage and stresses, and the polymer powder acts as support for overhanging structures. Due to the forces produced by the thermal stresses in metal L-PBF, the parts and the supports need to be fixed to the base while printing is in progress. Therefore, the parts must be removed from the base and the supports, which can be difficult in some cases.

However, the benefits of AM metal parts outweigh the drawbacks in specific cases, particularly for use in aerospace, automotive industries and medical applications. In the aerospace industry, new methods of fabricating lighter and stronger parts are constantly being developed (Blakey-Milner et al., 2021). For this reason, utilising AM to fabricate parts with a higher strength-to-weight ratio are necessary despite the high cost of fabrication. AM can be used for part consolidation in the automotive industry, thus reducing costs. L-PBF is especially promising in the medical field where AM can be used for various applications, from drill guides with hole locations determined prior to surgery to patient-specific surgical implants.

L-PBF parts can be designed with a specific porosity that will promote cell growth, and as a result, implants can promote bone growing into the porosity of the implant, allowing for a stronger bond between the implant and the patient's bone. Implants can also be designed to let blood pass through the implant, thus promoting tissue recovery and growth (Patterson et al., 2017; López-Castro et al., 2017; Yadroitsava et al., 2019).

2.2. Topology-optimised structures and lattices

Topology optimisation, by definition, is a mathematical method that optimises material layout within a given design space for a given set of loads, boundary conditions, and constraints to maximise the performance of the system. For engineering applications, simulation-driven design involves structural optimisation (also termed topology optimisation or generative design). It uses an iterative simulation and material removal process to optimise the required material distribution or stiffness for a given set of expected load cases (Du Plessis et al., 2019). The optimisation of the material distribution of an object plays a significant role in the lightweight structures with optimal mechanical properties and lower cost (Liu et al., 2019; Yu et al., 2018; López-Castro et al., 2017).

Objects developed by topology optimisation, sandwich, cellular and lattice structures can be used to alter the dynamic behaviour of a material, allowing it to have shock-absorbing and potential energy storage capabilities. Parts with the highest strength-to-weight ratios are most commonly fabricated by AM and optimised for the best result (Sigmund, 1994; Dede & Hulbert, 2008; Dong, 2020; Benedetti et al., 2021). The process of optimising a part to have a high strength-to-weight ratio comes at the cost of the maximum strength of the part; however, the weight of the part will be substantially reduced. Parts can also be optimised to have specific mechanical properties; for example, the part can have shock-absorption properties, thus removing the need for extra shock-absorption parts to be added to the assembly. Studies have

also shown that as a result of the large surface-area-to-weight ratio of lattice structures, it can also be utilised for thermal management; a higher surface area allows for more heat to be conducted or radiated (Peng et al., 2020; Lu et al., 2005; Dong, 2020).

Various materials benefit differently from topology optimisation. In AM, the most common is infill optimisation – the process whereby the AM machine fabricates the outside of the part as a shell and then only fills a specific percentage of the total inner density of the part. As a result of infill being a "grid" or a pattern structure, it can easily be incorporated into the slicing software of AM machines. It can thus be adapted to any part at any percentage (Culbreath et al., 2020; Wu et al., 2017). Infill-optimised parts mainly benefit from faster printing times and less material used. Therefore, AM polymer parts will be optimised to just above the required mechanical properties to reduce the part cost and printing time. Infill comes in a range of different shapes and sizes. Various patterns can have different advantages and disadvantages. For example, honeycomb structures are robust in the vertical direction and print relatively fast but are weak in the horizontal direction.

Another example is a gyroid infill that is numerically generated to be robust in all directions but takes longer to print; however, not as long as other infill patterns with similar robustness. The most basic infill pattern is the rectilinear pattern which is a square grid made of thin walls that go straight up. Other infill patterns are triangles, zig-zag, concentric, Hilbert curve and Archimean chords, to name a few. Figure 4 illustrates some of these patterns.

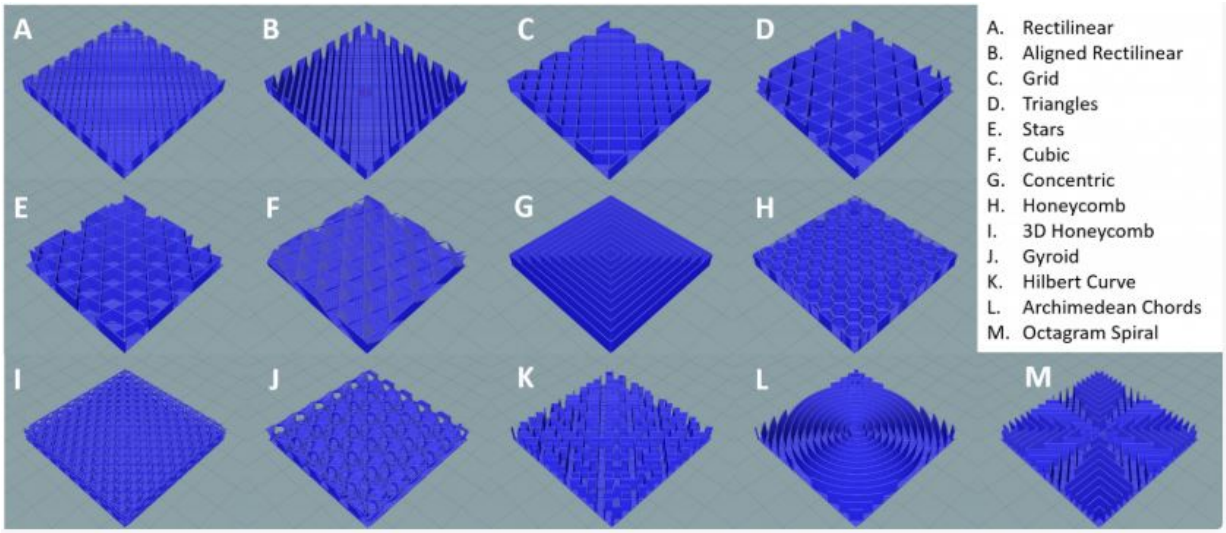

Figure 4. A range of infill patterns (allevi3d.com, 2020).

The nodes play an important role in mechanical properties of a lattice structure. These nodes have specific shapes and designs that behave differently depending on the design. The lattice

structure can consist of a single node design that is repeated, or a variety of nodes arranged in a specific manner to act together to give the lattice structure a specific mechanical behaviour. Increasing the strength of the nodes will increase the strength of the lattice structure, similarly, decreasing the node density will decrease the density of the lattice structure (Nagesha et al., 2020; Portela et al., 2018).

As a result of the complexity involved with fabricating lattice structures, AM processes proved to be the best means of fabricating these parts. The development and advancement of CAD and AM have made it more feasible for industries to fabricate functional parts that incorporate simulation-driven design, lattice structures, topology optimization, etc. The specific feature of AM to fabricate parts is that the limited build space (chamber). The machine settings also make a difference to the final parts and, if done incorrectly, can result in the failure of the part or even the fabrication process. However, as indicated by Du Plessis et al. (2018), when done correctly, the performance of these AM parts has been validated in various tests. Some limitations on the practical use of the AM technique are overhang angle, support removal, residual stress, build quality, high roughness and challenges in software tools that must be resolved for its more widespread industrial adoption.

The use of AM and lattice structures allows for the customisation of part mechanical properties, which could be beneficial in reducing bone resorption around implants. Bone resorption is the process whereby osteoclasts break down bone. The human body is continually in a state of bone remodelling to keep bones strong and healthy. Due to the higher stiffness of metals and alloys than bone, bone resorption can occur at the anchor points of metal and alloy implants, often referred to as stress shielding. Furthermore, the implants become loose and require surgery to fix or replace the implants (Mierzejewska et al., 2019; Yoon et al., 2018). A possible solution to bone resorption is fabricating implants from polymer materials. However, polymer implants cannot be used when the implant needs to support a significant amount of weight or stress. A viable alternative is using topology optimisation on metal or alloy implants to reduce the stiffness of the material closer to that of bone. By utilising topology optimisation on a metallic implant, it can be fabricated with a much lower elastic modulus allowing for better force distribution, reducing the chance of bone resorption due to stress shielding (Rahimizadeh et al., 2018; Peto et al., 2019).

Lattice structures can also promote bone growth and ingrowth into the scaffolding allowing for a superior merger between the implant and the bone. As AM allows for complex structures, implants can be fabricated with intentional porous surfaces or structures for tissue to penetrate

and grow into the implant. This can result in an interwoven bone and implant mesh which can significantly improve the bond between the implant and the bone (Chang et al., 2016; Li et al., 2020). Additionally, the implant's lattice structure can be designed to focus and enhance the effect of drugs and growth factors by concentrating the drugs at the implantation locations to ensure maximum effectiveness. This will also be effective against resorption, caused by the release of metal ions and particles from metallic implants, by injecting and concentrating stimuli-sensitive hydrogels between the implant and the bone, thereby blocking pro-inflammatory proteins, and preventing the progression of inflammation (Li et al., 2020; Bijukumar et al., 2018).

2.3. Compliant mechanisms

Unlike conventional mechanisms with moving parts and sliding surfaces, compliant mechanisms consist of a single solid body that uses elastic deformation to transfer motion, force or energy. By taking advantage of the elastic properties of a material and making long, thin features, the material will not be strong enough to oppose much force and will deform. Theoretically, if the deformation of the feature stays well below the material's yield point, the feature can have an infinite life cycle. The part can be transitionally thickened to prevent it from deforming at undesirable locations. By combining thick and thin features, thin features where deformation is desired, and thick features for where it is not, a relatively simple compliant part can be formulated (Zhu et al., 2020; Zhan et al., 2020; Niknam et al., 2020). A simple example of a compliant mechanism in nature is a tree with branches swaying in the wind, but the base is rigid and anchored in the ground.

Compliant mechanisms can simplify and reduce the part count of a mechanism or a machine because multiple parts can be fused into a single body that can still perform the same task. For example, a door hinge has a minimum of three parts, but a live hinge is a single part. Fewer moving parts will also result in a more reliable mechanism and lighter weight. Combining several parts into a single part will require less assembly time if any is required. Fewer moving parts and less wear means less maintenance is required. However, having parts that never slide or rub against anything and remain well below the material's yield point might not need any maintenance. Compliant mechanisms naturally come with a stiffness similar to a spring that is dependent on the material the mechanism is made of; this can be either a benefit or a drawback depending on how the mechanism will be used. Furthermore, compliant mechanisms have a limited range of motion because the elastic deformation of the part needs to stay well below

the yield limit of the material; otherwise, the material will start to degrade and eventually fail. A parasitic motion is also an undesirable factor of compliant mechanisms because of the pivoting point not being a single stationary point but moves as a result of the mechanical properties of the material and how they change while the mechanism deforms (Yu & Zhang, 2019; Ling et al., 2018; Cuellar et al., 2018).

The capability of compliant mechanisms has attracted extensive research on the subject. Generating a part numerically to have specific mechanical behaviour and then fabricating it to high accuracy is very promising. Some compliant mechanisms can be simple enough to fabricate two-dimensionally, and by applying a force correctly, will deform three-dimensionally and function compliantly. This technology makes it possible to build tiny compliant mechanisms to perform very small and precise motions, for example, micro-gripping manipulation (Ling et al., 2018; Yong, 2016; Kim & Cho, 2009; Bückmann et al., 2014). Larger, more complex compliant mechanisms are more challenging to simulate as they are not rigid bodies. Therefore, the deformation and movement of the part do not exactly perform as intended. The most noticeable indication of the non-rigid-body movement is seen in a live hinge, where it does not have a single pivoting point, but instead, the pivoting point moves as the part deforms as a result of kinematic and elastic-mechanical behaviours (Yu & Zhang, 2019).

The most remarkable part of compliant mechanisms is that they are monolithic structures that can mechanically move and deform within limitations. Compliant mechanisms can be numerically generated to deform and move in specific ways. However, for the mechanism to work as generated, high precision and the ability to fabricate very complex and intricate structures are required, which is where AM is most promising. Utilising AM to fabricate compliant mechanisms has proven favourable as the AM process allows for the complexity and accuracy required in developing compliant mechanisms (Correa & Ferreira, 2015; Cuellar et al., 2018). Nevertheless, AM has its drawbacks, mainly the layer-upon-layer process, as it results in the part behaving differently in the horizontal direction than in the vertical.

Fabricating compliant mechanisms from polymer materials allows the mechanism to deform easily compared to metal material or alloy. However, polymer parts will be substantially weaker and break much earlier, whereas metal will be more challenging to deform, last longer and be more durable. Metal compliant mechanisms can have thinner features as the metals have higher mechanical properties, which means that by incorporating the L-PBF process in the fabrication of compliant mechanisms, they can be developed with finer detail and more

compliance. By utilising compliant mechanism design rules and taking into account AM limitations, even single parts made from a rigid material such as titanium were manufactured; Figure 5 is an example of this.

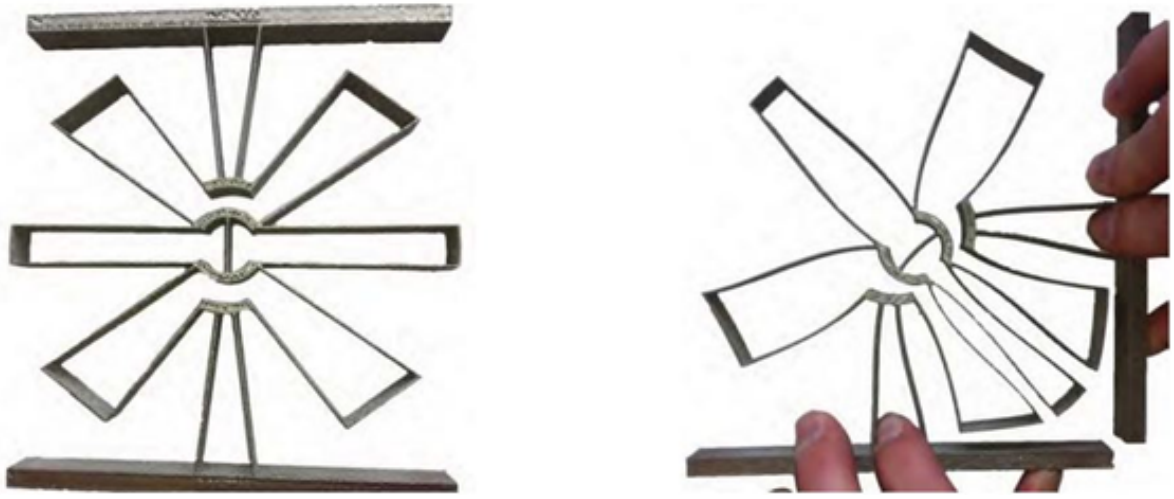

Figure 5. A compliant hinge fabricated with L-PBF in titanium (Fowler, 2012).

A variety of flexure patterns and structures can also be used to allow the deformation of a monolithic structure. Removing material from a thin wall in a grid-like pattern can have the same effect as making a thinner wall. However, a thin wall grid will be more structurally supportive in the vertical direction, thus limiting the deformation of the structure to sideways motion. Interlocking flexures can allow for a much more fixed pivoting point. Having two thin wall grids will assist the part in deforming from a central pivoting point; the grid flexure structure also allows for two flexures to interlock without being connected. This type of monolithic structure is complemented by the AM fabrication process and allows for much more control with the mechanism (Keiner et al., 2019; Kruis et al., 2019; Wei et al., 2018). Figure 6 is an example of an interlocking flexure monolithic structure.

Figure 6. An interlocking flexure monolithic structure (Keiner et al., 2019).

2.4. Metamaterials

Metamaterials are artificially composed materials that have been engineered to exhibit properties that often do not occur in nature. Metamaterials are assembled from various elements mainly produced from composite materials such as polymers and metals. They are typically arranged in a repeating pattern on a milli-, micro- or even nanometre scale. Metacells, also referred to as unit cells, are the hypothetical foundation of a metamaterial. These unit cells are commonly on the micro- or nanometre-scale and are the geometrical structures arranged in a repeating pattern to form the metamaterial. The design of the unit cells and how they are arranged determines the properties of the metamaterial. Furthermore, building material from the atomic level is possible in the current day and age. It is very complicated and takes a substantial amount of time to make even a small piece of material. Additionally, even creating metamaterials with unit cells is enough to prove that the properties of a material can be changed when modified on a micro- or nanometre-scale (Surjadi et al., 2019; Yu et al., 2018).

Metamaterials obtain their properties from the shape, size, arrangement and geometry of the elements used in their construction. This allows the material to be engineered to have specific properties such as materials that show zero or negative mechanical parameter values or materials that change and manipulate electromagnetic waves, sound waves and light (Bertoldi et al., 2017; Nicolaou & Motter, 2012; Bückmann et al., 2014). This has attracted much attention to metamaterials, and more research has been done on the subject. However, the main category of metamaterials to be examined in this study is mechanical metamaterials.

Mechanical metamaterials utilise the synergy between topology optimisation and material compositions to create materials with different mechanical properties than their natural counterparts. These properties include Young's modulus, shear modulus, bulk modulus, and Poisson's ratio. Some advancements that have been made in mechanical metamaterials include ultra-lightweight and ultra-stiff materials that consist of nanoscale metacellular structures, negative compressibility or negative thermal expansion materials and materials with negative Poisson's ratios, to name a few. Changing the material's properties to specific values and behaviours will optimise metamaterials for specific industrial applications (Yu et al., 2018; Surjadi et al., 2019. Therefore, a substantial amount of research needs to be done on the subject of mechanical metamaterials, especially.

The Poisson's ratio is described as the resistance of a material to laterally contract when a longitudinal force pulls it (Greaves et al., 2011). An auxetic material is a technical term for a

metamaterial with a negative Poisson's ratio, first introduced in 1991 by Evans (Evans et al., 1991). A material with a positive Poisson's ratio tends to contract in the lateral directions while a longitudinal tensile force is applied to it, trying to keep the area more or less the same (seen in Figure 7a). Auxetic metamaterials expand in all directions when a longitudinal tensile force is applied, causing the volume of the material to alter, as seen in Figure 7c) (Kolken & Zadpoor, 2017; Mizzi et al., 2018). Therefore, a zero Poisson's ratio means there is no distortion in the lateral direction when the material changes in length, as indicated in Figure 7b) (Mizzi et al., 2018).

For biomedical applications, a metamaterial is needed that can mimic the properties or work with the body to help restore the injured part of the body. The stiffness of metal implants is much higher than that of bone, leading to a stress-shielding effect and loosening of the implant. Bone is a known natural anisotropic material; therefore, metamaterials manufactured by AM and engineered to be more compliant to exhibit less stress can be a rational choice instead of solid implants (Yan et al., 2015). Implants can also be fabricated to be porous, promoting faster bone growth. Some parts of the body also have auxetic behaviour, such as tendons which can be replicated with metamaterial structures and be used as tendon implants (Bobbert & Zadpoor, 2017; Gatt et al., 2015).

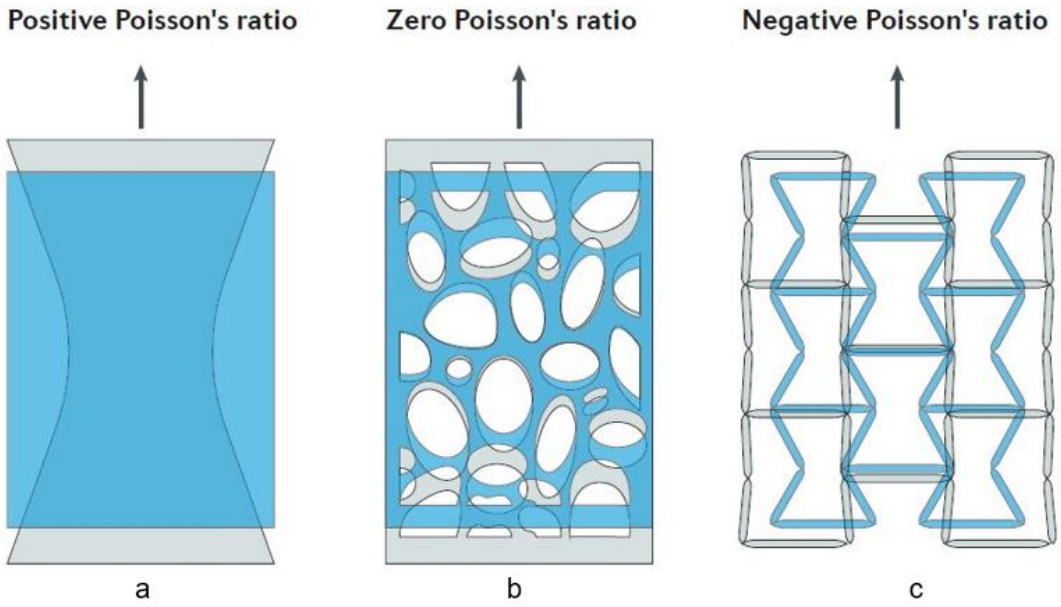

Figure 7. A demonstration of the behaviour of a material when it has a positive (a), zero (b) and negative (c) Poisson's ratio (Bertoldi et al., 2017). Blue is the initial state; grey is after tensile deformation.

The advancements in AM over the last few decades significantly improved the viability of using 3D printers to fabricate metamaterials. This is due to the enhanced level of detail that AM machines can fabricate, allowing for finer detailed and complex structures to be fabricated. Advancements in AM technologies have come as far as allowing for features down to the nanometer scale to be fabricated (Surjadi et al., 2019; Chen et al., 2020; Challagulla et al., 2020). However, the process of fabricating metamaterials on a micro- and nanometre-scale is very time consuming and does not produce a viable amount of metamaterial. Nevertheless, as AM continues to advance, the fabrication times of these metamaterials will be reduced, and the quantities produced will increase. Another benefit of AM is combining different materials throughout the fabrication process, utilising the different material properties, and modifying them in whichever way is required (Yadroitsau, 2008; Kinnear, 2016).

2.5. Dynamically responsive structures

Dynamically responsive structures combine metamaterials, compliant mechanisms, and topology optimised objects. By combining the methods of compliant mechanisms with the nodes or unit cells of a lattice structure, the result will be a metamaterial that possesses compliant deformation-like properties. Furthermore, this will produce a metamaterial that can be used as a frame-like structure but can be engineered to have dynamic or elastic properties such as vibration or shock-absorbance (Dede & Hulbert, 2009). Another property that can prove beneficial in a dynamically responsive structure is a negative Poisson's ratio or an auxetic structure. This could allow the structure to expand and contract equally in its horizontal plane while remaining rigid perpendicular to the plane (see Figure 8).

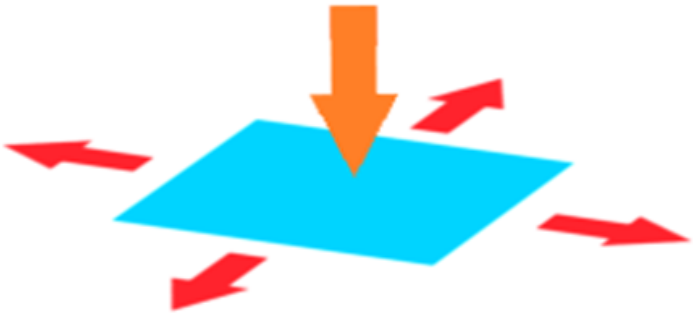

Figure 8. Scaffold is auxetic in one plane, but rigid perpendicular to that plane. Red arrows indicate the directions in which the scaffolding can expand and contract, and the orange arrow indicates the force perpendicular to the plane.

Scaffolds are structures mainly utilised in regeneration and tissue engineering. Therefore, developing a dynamically responsive scaffolding (DRS) mainly focused on medical use. An example of this is developing bone replacement implants from DRS methods which will reduce the stiffness of the implant and can be engineered to behave similarly to the bone, thus reducing the effect of stress shielding. Furthermore, this will reduce the likelihood of the implant becoming loose and requiring surgery to refasten or replace the implant. AM implants benefit from the geometric accuracy and the significantly more straightforward fabrication process compared to other methods of implant fabrication. The surface quality resulting from SLS and L-PBF processes is porous, and specialised material that contains substances such as HA can contribute to bone tissue growth (Al-Tamimi et al., 2017; Miranda et al., 2019).

Bone resorption is the process whereby osteoclasts break down bone. The human body is continually in a state of bone remodelling to keep bones strong and healthy. Due to the high stiffness of metals and alloys compared to bone, bone resorption can often occur at the anchor points of metal and alloy implants, often referred to as stress shielding. Metamaterial allows engineers to modify the mechanical properties of a part, for example, reducing the stiffness of metallic bone implants, allowing for better energy dissipation into the bone and, therefore, reducing the stress-shielding effect (Hashemi et al., 2020).

Dynamically responsive scaffolds can be designed to have different mechanical behaviours in different axes. For example, the scaffolding will be able to protect from impacts in the perpendicular direction of the scaffold plane while being able to expand and contract in the horizontal directions. This will prove especially beneficial in the biomedical field of cranial protection and for more common implants such as hip implants, as the reduced stiffness of the metamaterial will reduce bone resorption and increase implant lifespan. Developing a DRS with auxetic properties can result in a scaffolding that can deform in one plane but is still rigid perpendicular to that plane. This type of DRS would prove to be very beneficial in the cranial implant field, especially for children whose skulls are still expanding. The DRS will expand with the child's skull while still protecting the brain, therefore, reducing or removing the need for periodical cranial plate replacement surgeries for the rest of the child's life. Autologous bone grafts are preferred for pediatric cranioplasty for infants and children under seven years. As the implant cannot grow with a young child, some authors suggest reserving metal implants for children over ten years (Salam et al., 2018).

2.6. Summary

This chapter gives an overview of the relevant topics and methods in creating a DRS. The benefits and the possible challenges that could be expected were investigated. An overview of using AM to fabricate DRS is presented with a comparison of the benefits and drawbacks of AM versus IM and which is best to be used in this study. A breakdown is also shown regarding the percentage of research and development done in the AM field. Then, a deeper dive into the challenges and the broad range of processes involved in polymer AM and a range of biocompatible and biodegradable polymer materials that can be utilised.

The utilization of L-PBF, an AM process used to fabricate 3D parts from metals and alloys, was researched. The process of L-PBF was explained, and the differences in polymer and metal processing were discussed. The difficulties with metal L-PBF were explored so that solutions can be found if problems are encountered. The research also included L-PBF features that could prove beneficial in creating DRS, features such as single track/vector printing and topology optimisation. The methods and processes of topology optimisation of materials were also explored. The benefits and drawbacks of utilising topology optimisation were discussed and how it can be used in creating DRS. Utilising different topology patterns when fabricating an object can result in the object possessing different properties, even if the object consists of the same amount of material. The possibility of utilising topology optimisation in medical applications, and the benefits that it can provide, were also discussed.

Additionally, research was done into compliant mechanisms to investigate what they are and how they work. The benefits of compliant mechanisms were explored, and more possibilities were discussed to assist with the creation of DRS. AM of compliant mechanisms and the feasibility of utilising metals or alloys to fabricate compliant mechanisms were researched. Furthermore, the topic of metamaterials was also studied, specifically mechanical metamaterials that have unnatural mechanical behaviours and properties. As discussed, unit cells are the hypothetical foundation of a metamaterial and are the determining factor of the metamaterial's properties. Different unnatural properties were explored, and the auxetic behaviour seemed promising for creating a DRS. Moreover, advancements in the scalability of metamaterials and their unit cells were researched and proved to be in line with the goals of this study.

Finally, research was done into DRS that behave the same way, such as dynamic lattice structures. However, the leading factor of a DRS compared to other structures was the ability

to return to its initial form due to the compliant mechanism methods involved in its creation. The possibility of a DRS seemed to be particularly beneficial in the medical field, thus resulting in the creation of the DRS.

CHAPTER 3: MATERIAL AND METHODS

For initial tests, experimental specimens were produced from ABS filament by an FDM system. Nylon and Ti6Al4V samples were then manufactured by L-PBF and were tested using a tensile testing machine. Research methodology is described in chapter 1.4.

3.1. Materials

3.1.1. ABS filament

Acrylonitrile Butadiene Styrene (ABS) is a thermoplastic commonly used for FDM printing due to its relatively high strength, impact resistance, toughness, heat resistance, good electrical insulation, and high strength-to-weight ratio. The ABS filament used in this study was supplied by 3D Printing Systems SA.

The properties of ABS material are shown in Table 2.

Table 2. Material properties of ABS used for the preliminary simulations

Material properties	Value
Elastic modulus	1598 MPa
Poisson's ratio	0.35
Density	1110 Kg/m^3
Tensile strength	28 MPa
Shear Modulus	755 GPa
Yield strength	39 MPa

3.1.2. PA 2200 powder

PA 2200 is based on polyamide 12 powder supplied by EOS. Compared to standard polyamide 12, PA 2200 is characterised by higher crystallinity and higher melting point in comparison with pure PA12 due to the specific production process, as indicated in the supplier's product information sheet. For this case study, the powder is used in a 50% virgin and 50% used powder ratio. The particle size distribution ranges from 30 µm to 100 µm, and a scanning electron microscope (SEM) image shows PA 2200 powder particles (Figure 9).

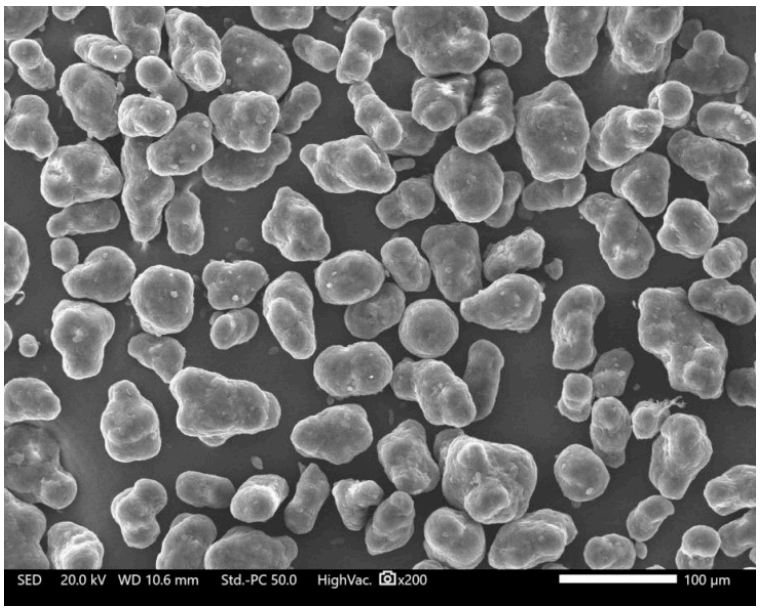

Figure 9: SEM photo of used PA 2200 powder.

PA 2200 has excellent long-term stability, high chemical resistance and is biocompatible. Polymer-based implants are lighter, more cost-effective, and mostly more manageable to work with than their metallic counterparts, which makes them a suitable option for implant material when providing strength is not of much concern. PA 2200 can be combined with HA to form a PA 2200/HA osteoconductive mixture (Van Der Walt & Nsengimana, 2016). The material properties of the PA 2200 are shown in Table 3 below.

Table 3: Material properties of PA 2200 used for the SLS specimens (EOS PA 2200, 2021)

Material properties	Reference values from EOS
Elastic modulus	1650 MPa
Elongation percentage	18%
Tensile strength	48 MPa
Density	930 kg/m^3

3.1.3. Ti6Al4V powder

Titanium (Ti) is a very popular material with a wide range of applications in industries such as aerospace, biomechanical, automotive, and chemical handling. This is due to Ti's high mechanical strength-to-weight ratio and exceptional chemical resistance. By adding elements such as aluminium (Al), vanadium (V), nickel (Ni), molybdenum (Mo), chromium (Cr) or zirconium (Zr), the mechanical properties of Ti alloys can be altered such as raising or lowering heat resistance, conductivity or ductility.

The metallic material selected for study is Ti6Al4V. Ti6Al4V alloy is one of the preferred alloys for medical implants due to its outstanding strength-to-weight ratio, fatigue resistance, high corrosion resistance and biocompatibility. Ti6Al4V alloy contains 89 wt% Ti, 6 wt% Al, 4wt% V and 1 wt% trace elements. The two primary grades of Ti6Al4V used for implants are Ti6Al4V grade 5 and Ti6Al4V grade 23 ELI (Extra Low Interstitials). Ti6Al4V grade 5 and Ti6Al4V grade 23 ELI are quite similar, with the most significant difference being that Ti6Al4V grade 23 ELI has reduced levels of nitrogen, oxygen, iron and carbon, which improves the fracture toughness and ductility (Le Roux et al., 2020; Chen et al., 2020). Figure 10 is a graph that shows the ultimate tensile strength (UTS), yield strength (YS), elongation and area reduction of tensile tested LPBF Ti6Al4V grade 23 ELI specimens.

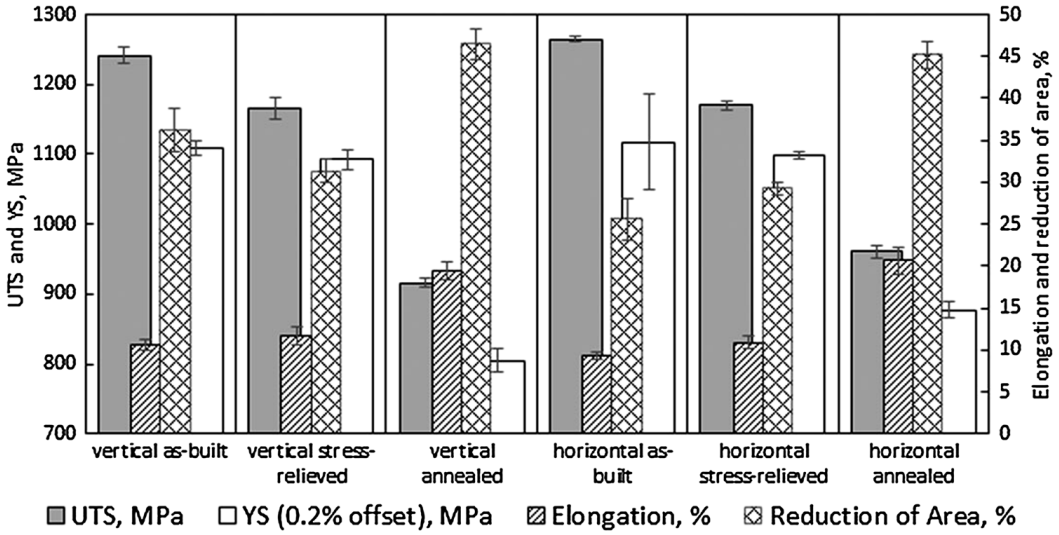

Figure 10. Tensile mechanical properties of Ti6Al4V ELI samples (Yadroitsev et al., 2018).

Table 4: Mechanical properties of horizontal stress-relieved and annealed L-PBF Ti6Al4V grade 23 samples (Yadroitsev et al., 2018)

Material properties	Value
Elastic modulus	110 GPa
Elongation percentage	21%
Poisson's ratio	0.31
Density	4410 kg/m^3
Yield strength	880 MPa
Ultimate tensile strength	960 MPa

3.2. AM systems

3.2.1. UP Mini 2SE FDM printer

ABS samples were fabricated on a Tiertime UP Mini 2SE printer located at the Product Development and Technology Station (PDTS) at Central University of Technology, Free State (CUT). The UP Mini 2SE (Figure 11, Table 5) is a fully enclosed printer utilising an FDM extrusion process to build parts layer-by-layer. The ABS samples were sliced and printed on Tiertime's UP Studio and flexbord with no adhesives.

Figure 11: UP Mini 2SE (3D Printing Systems SA, 2021).

The UP Mini 2SE is a compact midrange FDM 3D printer that can be set up out of the box and print within five minutes. This printer is very popular for its ABS printing capabilities.

Table 5: UP Mini 2SE specifications (3D Printing Systems SA, 2021)

Printing technology	FDM/MEM (Melted Extrusion Modelling)
Build volume	120 x 120 x 120 mm
Extruders	Single
Extruder maximum temperature	299 °C
Extruder maximum travel speed	150 mm/s
Smallest layer height	0.15 mm
XY accuracy	±0.15 mm/100 mm
Filament diameter	1.75 mm
Power input	110–240 VAC, 50–60 Hz, 90 W

3.2.2. EOSINT P 396 system

The PA 2200 samples were fabricated on an EOSINT P 396 SLS machine located at the CRPM at CUT. The EOSINT P 396 (Figure 12, Table 6) is a highly productive 3D printing system that utilises an SLS system to produce high-quality parts layer by layer.

Figure 12: EOSINT P 396 SLS system (EOS SLS, 2021).

Table 6: EOSINT P 396 specifications (EOS, 2021)

Printing technology	L-PBF (SLS)
Build volume	340 x 340 x 600 mm
Laser type	CO_2, 70 W
Scan speed	Up to 6 m/s
Smallest layer height	60 µm
Precision optics	F-theta lens, high-speed scanner

3.2.3. EOSINT M 280 system

The Ti6Al4V ELI samples were fabricated on an EOSINT M 280 L-PBF machine located at the CRPM. The EOSINT M 280 (Figure 13, Table 7) is an industrial 3D printing system that can fabricate high-quality metallic parts. Ti6Al4V ELI samples were manufactured with standard process parameters and strategy recommended by supplier.

Figure 13: EOSINT M 280 system (EOS, 2021).

Table 7: EOSINT M 280 specifications (EOS, 2021)

Printing technology	LPBF
Build volume	250 x 250 x 325 mm
Laser type	400 W Yb-fibre laser
Scan speed	Up to 7 m/s
Smallest layer height	100 µm
Focus diameter	100–500 µm
Power consumption	8.5 kW

3.3. Numerical simulations

The software used to run the numerical simulations is Simulation Solutions for SolidWorks 2020, specifically finite elements analysis (FEA). Simulation Solutions has various simulations, ranging from FEA and flow simulations to plastic injection moulding simulations. SolidWorks also has an extensive database of different materials and their material properties used for the simulations.

3.4. Tensile tests

The PA 2200 and Ti6Al4V specimens were tested on the MTS Criterion Model 43 located at CUT. The MTS Criterion Model 43 (Figure 14) has a single test space rated for forces ranging from 100 N to 50 kN. The polymer specimens were pulled at a rate of 10 millimetres per minute until failure occurred, and the Ti6Al4V specimens were pulled at a rate of 12 millimetres per minute.

Figure 14: MTS Criterion Model 43 tensile testing machine (MTS, 2021).

Figure 15 demonstrates how the scaffolding specimens were placed in the machine for tensile testing. This layout was selected to observe the behaviour of the scaffoldings when they are elongated in a single direction. It will also give an idea of the weak points in each scaffolding and an estimate of how far the scaffoldings can elongate before failing.

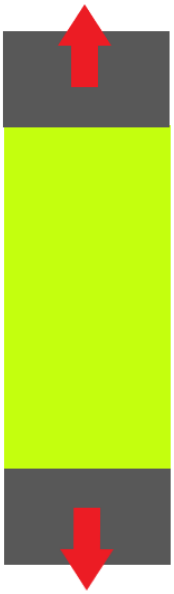

Figure 15: Scaffolding tensile test schematic. The green section shows the scaffolding area, the grey areas are solid and used to fasten the scaffolding in the machine, and the arrows indicate the directions in which the specimens were pulled.

3.5. Scaffolding design

The conceptualisation of the scaffoldings was done with the following requirements: the scaffoldings had to be able to repeat infinitely, and therefore a hexagonal and a square pattern were chosen. These patterns are divided into two categories, each with the same distances between nodes (Figure 16). Furthermore, the centre of each node is a cylinder with a 2 mm hole to be used as an anchor point for screws. Lastly, all walls are 0.5 mm thick with 0.7 mm thick node cylinder walls.

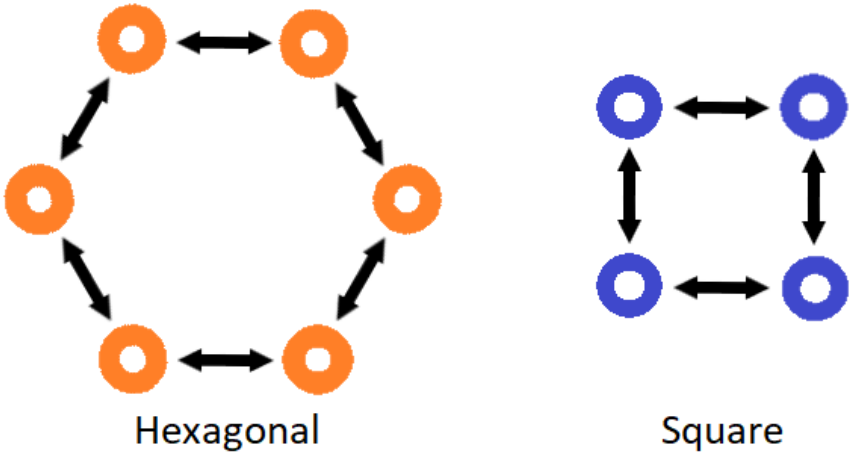

Figure 16: Hexagonal and square pattern categories.

3.5.1. Wide-bow pattern

The wide-bow pattern has three arms on each node and falls in the hexagonal category. The arms start with a long spiral arch that straightens and then ends with another arch that connects to the arm of the next node (Figure 17). The scaffolding structure is better presented when six nodes are combined to form a hexagonal shape. The linked arms between two nodes form a wide, flat bow that winds into the nodes in opposite directions. Theoretically, the long arch of the arms should allow for very low resistance at the beginning of the deformation process.

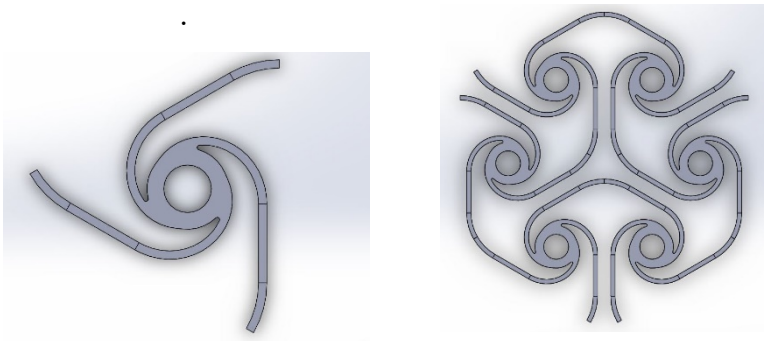

a b

Figure 17: Wide-bow node (a) and single pattern (b).

3.5.2. Double-bow pattern

The double-bow pattern has six arms on each node and falls in the hexagonal category. The arms are relatively short compared to the other designs and are half ovals that intersect with the node halfway from one end to another (Figure 18). The arms link up with those from the next node to form complete ovals resulting in six links on each node and two links between each node, which is double that of the rest of the designs. Theoretically, this scaffolding should be much stiffer than any other design but still allow for compliant deformation.

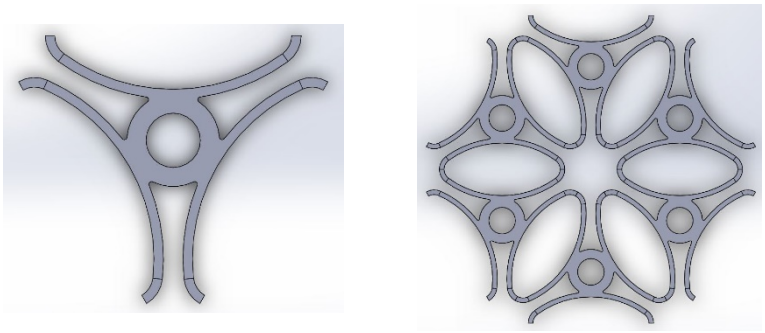

a b

Figure 18: Double-bow node (a) and single pattern (b).

3.5.3. Long-bow pattern

The long-bow pattern has three arms on each node and falls in the hexagonal category. The arms are connected tangentially to the node in a counter-clockwise or clockwise rotation. The arms extrude from the node in a long, straight arc with a small arch on the end where it links to the next nodes (Figure 19). When connected, six nodes form a hexagon with long, high-

arching arms and ample expansion space. Theoretically, the long arms should allow considerable displacement between the nodes and minimum resistance force when expanding.

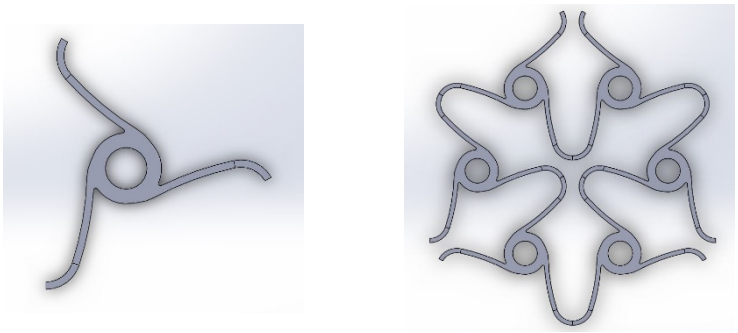

a b

Figure 19: Long-bow node (a) and single pattern (b).

3.5.4. Mirrored-spiral pattern

The mirrored-spiral pattern has four arms on each node and falls in the square category. The arms spiral off the centre node into straight lines with small arches on the ends to link to the next node (Figure 20). In order to form the single four-node pattern, the first node is mirrored in the X- and Y-axis, and lastly, one of the second nodes is again mirrored into the fourth position, as seen in Figure 20. Theoretically, the reversed directions of the adjacent nodes will cause the nodes to rotate in opposite directions, resulting in the nodes displacing away from the adjacent nodes. This should result in an auxetic scaffolding.

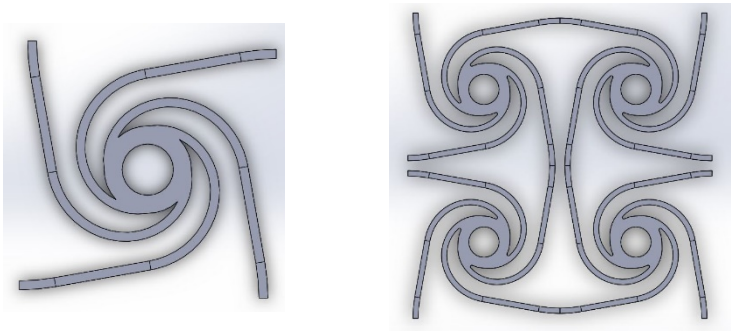

a b

Figure 20: Mirrored-spiral node (a) and single pattern (b).

3.5.5. Repeating-spiral pattern

The repeating-spiral pattern has four arms on each node and falls in the square category. The arms are shaped similar to a half rotation of the golden ratio spiral, starting from the centre of the node (Figure 21). The beginning of the spiral intersects with the screw mount of the node and therefore was removed. The square single pattern is formed by linking four nodes in the square shape, with all node spirals rotating in the same direction. This combination of spirals in the same rotational directions should, theoretically, allow for displacement in one of the axes whilst having a minimum displacement in the other direction, in other words having a zero Poisson's ratio.

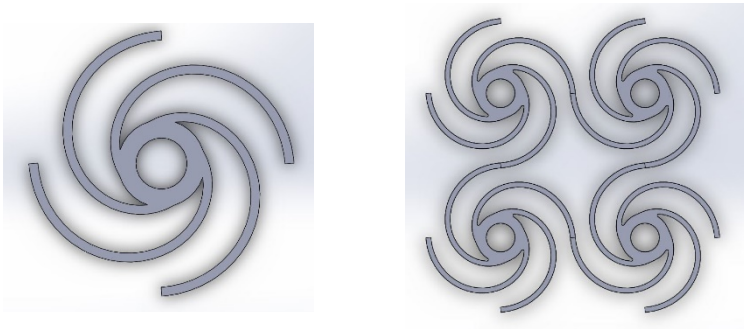

a b

Figure 21: Repeating-spiral node (a) and single pattern (b).

3.5.6. Linked-spiral pattern

The link-spiral pattern has four arms on each node and falls under the square category. The arm starts from the node and spirals out into a strait that will overlap with adjacent arms (Figure 22). The single pattern is formed by mirroring the node at the X- and Y-axis, similar to the mirrored-spiral pattern. However, the straight parts of the arms overlap, creating a common beam supported by four nodes. Theoretically, the common beam supported by four nodes should make for a significantly more stable structure, especially in the axis perpendicular to the scaffolding plane.

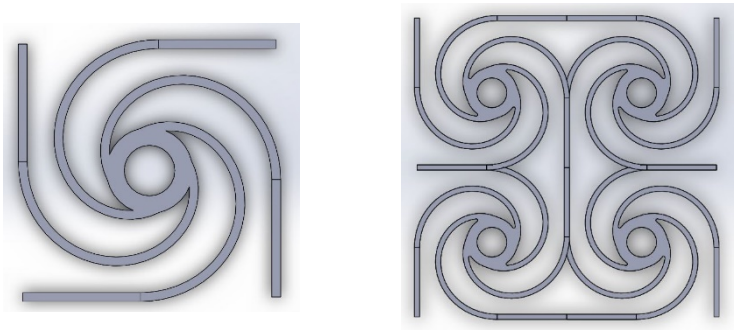

a b

Figure 22: Linked-spiral node (a) and single pattern (a).

3.5.7. Overview of designed samples

Preliminary tests were done with FDM-printed scaffoldings. The scaffoldings were printed on a Tiertime UP Mini 2SE from ABS material. These scaffoldings were printed 60% bigger than described in Chapter 4 as the FDM printer requires a wall thickness of 0.8 mm to be capable of fabricating. The scaffoldings were also designed in hexagonal and square shapes with three single patterns in each direction, as seen in Figure 23Figure 24 - Figure 26. The purpose of the study on the FDM specimens was to inspect the dynamic behaviour of the scaffoldings and establish the difference in stiffness of the different scaffolding designs.

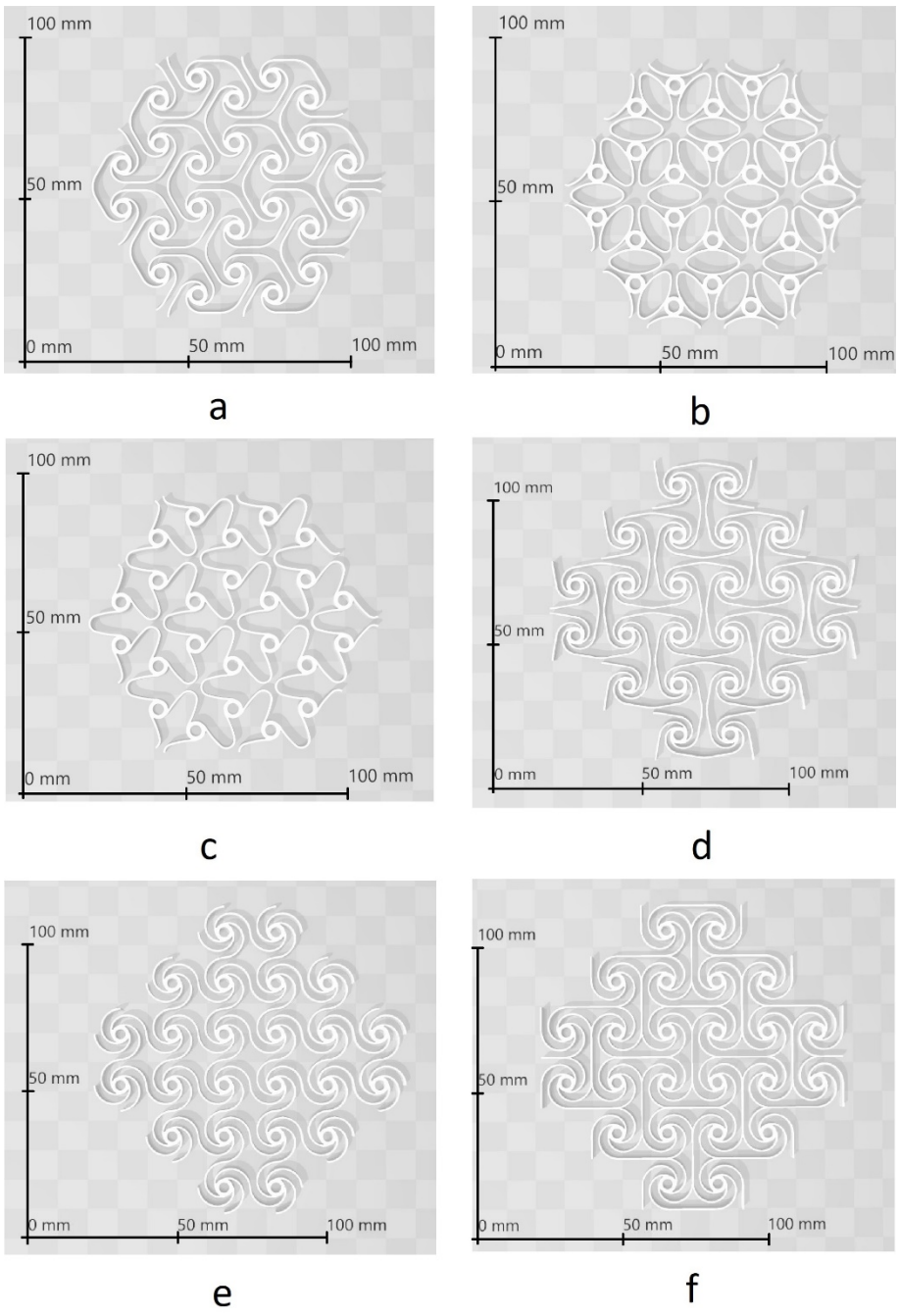

Figure 23: STL models of FDM specimens: a) wide-bow, b) double-bow, c) long-bow, d) mirrored-spiral, e) repeating-spiral, f) linked-spiral designs.

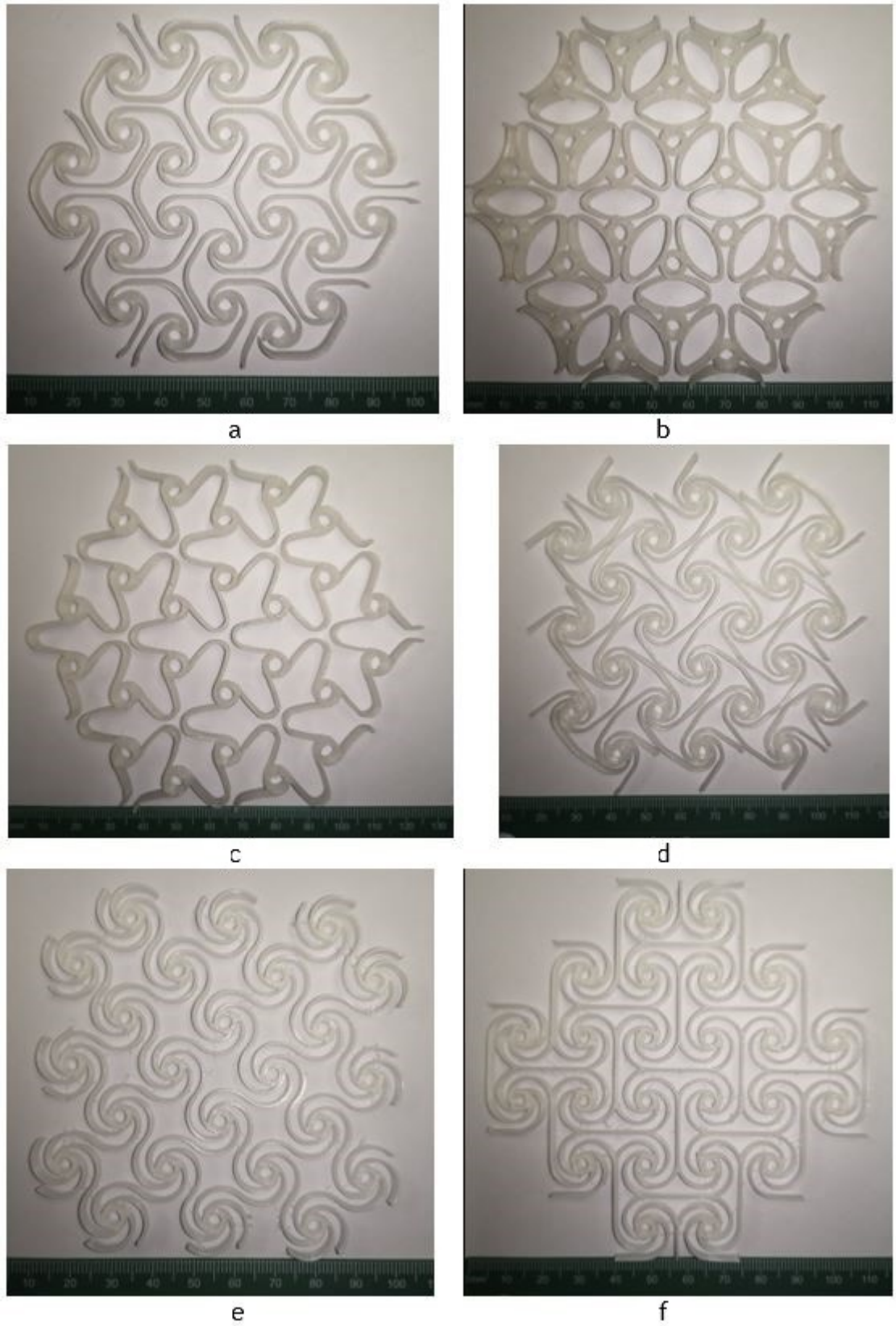

Figure 24: FDM-printed specimens: a) wide-bow, b) double-bow, c) long-bow, d) mirrored-spiral, e) repeating-spiral, f) linked-spiral designs.

Initially, the preliminary scaffoldings were fabricated at the intended scale to verify the printed dimensions compared to the CAD models. Figure 26 shows the SLS PA 2200-printed scaffoldings painted in grey for a better contrast view.

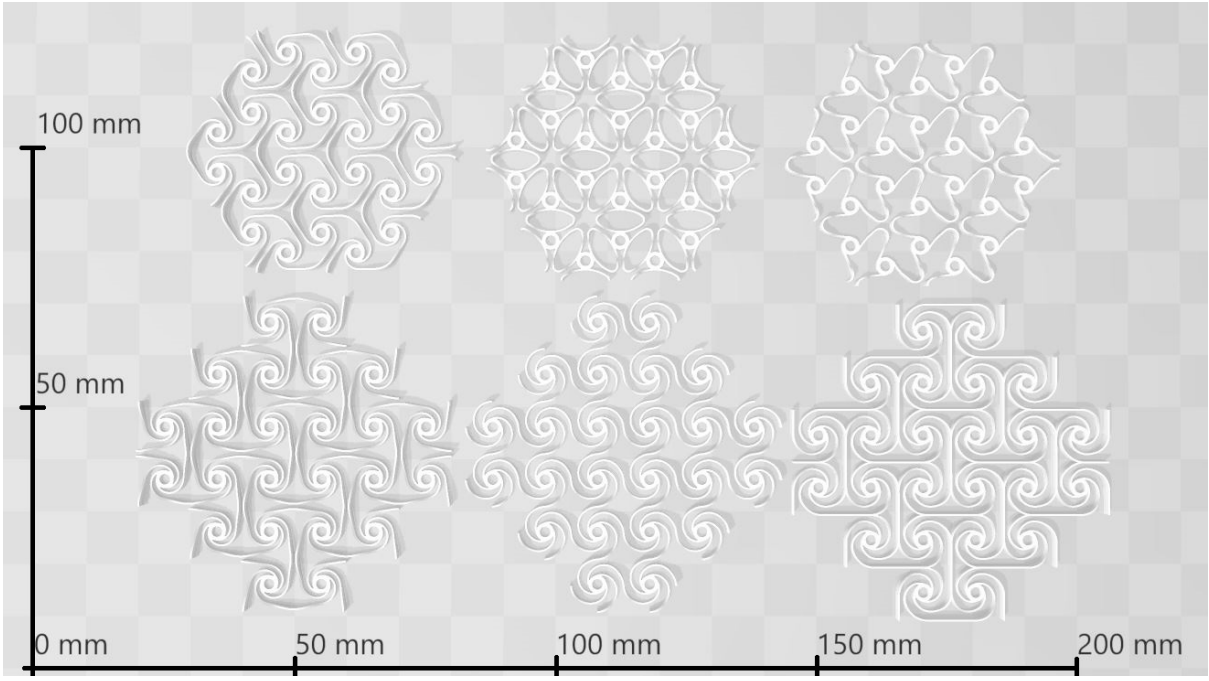

Figure 25: STL models of PA 2200 scaffoldings.

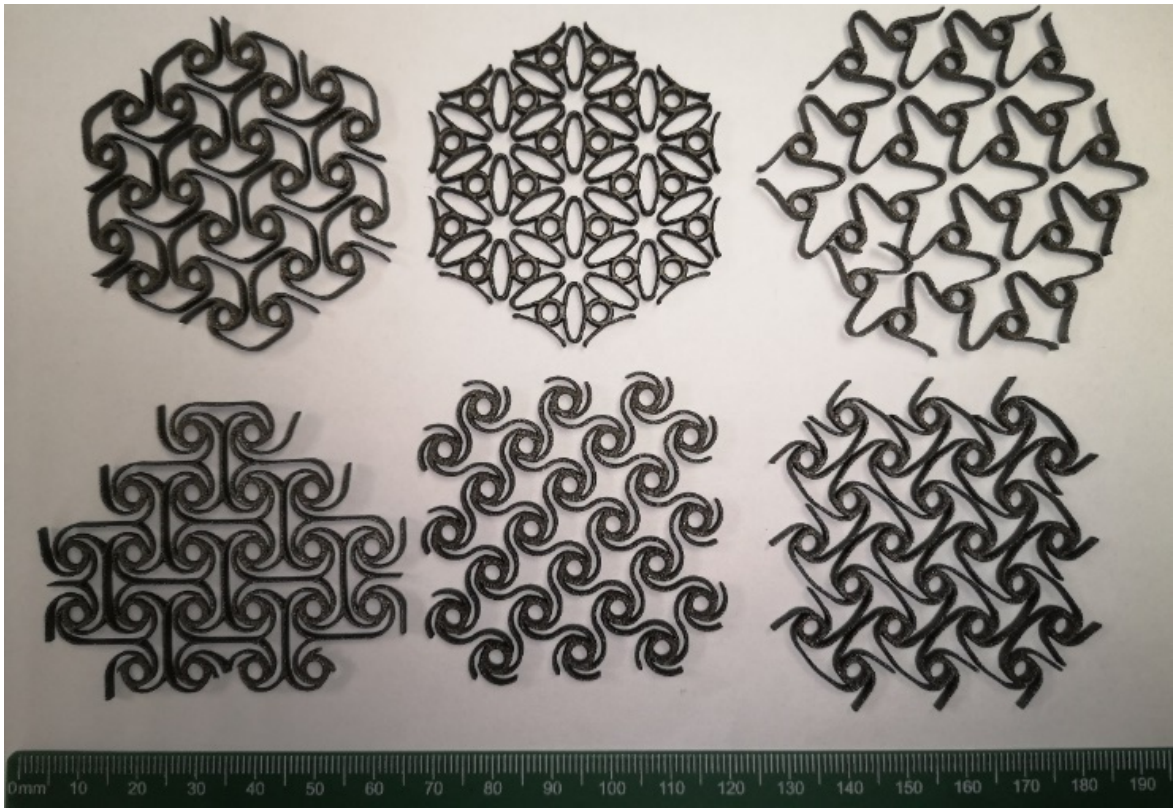

Figure 26: Manufactured PA 2200 scaffoldings.

The next step was to modify the scaffoldings into a structure that could be clamped and stretched on a tensile testing bench, see Figure 27. Due to the geometries of the scaffoldings, the behaviour of a single scaffolding would be different in every direction. Therefore, there are two specimens of each scaffolding that will be oriented in two different directions; for the hexagonal pattern scaffolding, the two directions are in the X- and Y-axis, as seen in Figure 28a. For the square pattern scaffolding, the first direction can be in either the X- or Y-axis as the geometries are identical. Therefore, the second direction is 45° offset from the X- and Y-axis, as seen in Figure 28b.

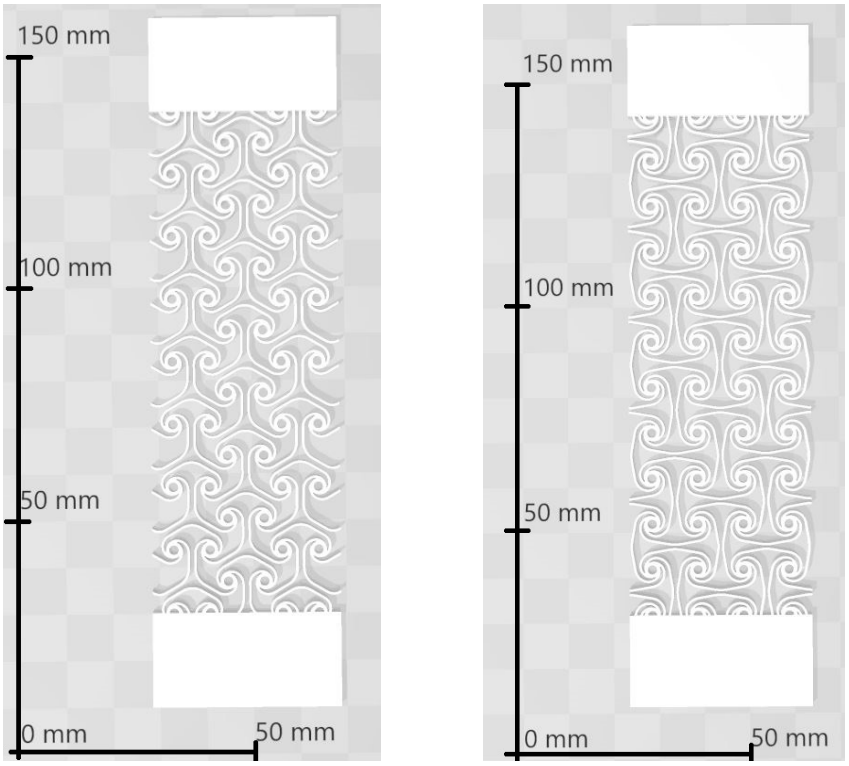

a b

Figure 27: Tensile specimen examples: a) hexagonal pattern specimens b) square pattern specimens.

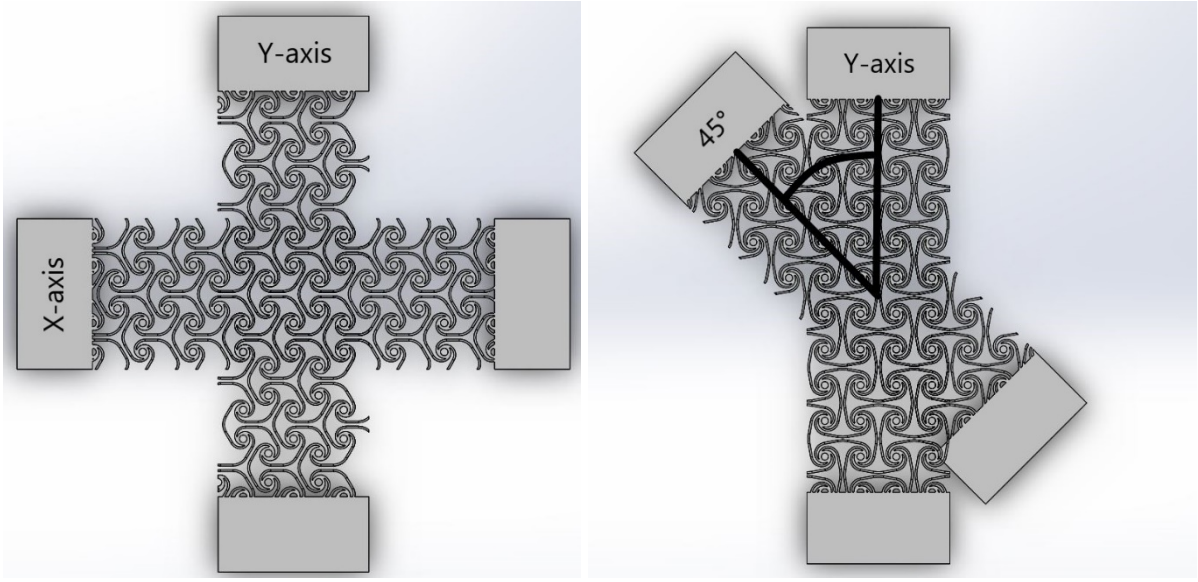

a b

Figure 28: Tensile specimen directions: a) a hexagonal pattern specimen in the X- and Y-axis, b) square pattern specimen in the parallel and skew axis.

The specimens are 2.6 mm thick, just over the intended thickness of 2 mm of the final Ti6Al4V scaffoldings, with a width of 40 mm to fit in the jaws of the tensile testing bench. The ends of the specimens have a solid section about 20 mm in length to provide grip for the tensile test bench jaws. The length of the specimens is node-to-node-based to allow the geometries of the scaffoldings to deform as if they were mounted at the nodes. The final length is the closest node-to-node length of 100 mm, along with the solid sections. This means there is a different length for each direction in each category resulting in four different total lengths: 146.7 mm for the hexagonal X-axis, 147.8 mm for the hexagonal Y-axis, 150 mm for the square Y-axis and 139 mm for the square 45° offset direction.

For the Ti6Al4V scaffoldings, the wall thickness was reduced from 0.5 mm to 0.3 mm, the mounting node walls reduced from 0.7 mm to 0.5 mm, but with a 2 mm hole for the mounting screws, the pattern size was reduced by 25%, and finally, the thickness of the scaffoldings was reduced from 2.6 mm to the 2 mm intended implant thickness. The specimens have an X-axis and a Y-axis for the hexagonal pattern wide-bow, and a parallel-axis and a skew-axis for the square pattern linked-spiral. The Ti6Al4V tensile specimens have the same design as the polymer specimens, with a 40 mm width to fit in the tensile tester jaws and a 20 mm solid part at the ends for the jaws to grip. The lengths of the specimens were determined by the closest node-to-node length of 100 mm, similar to the polymer specimens. Figure 29 shows a comparison of the Ti6Al4V design and the polymer design.

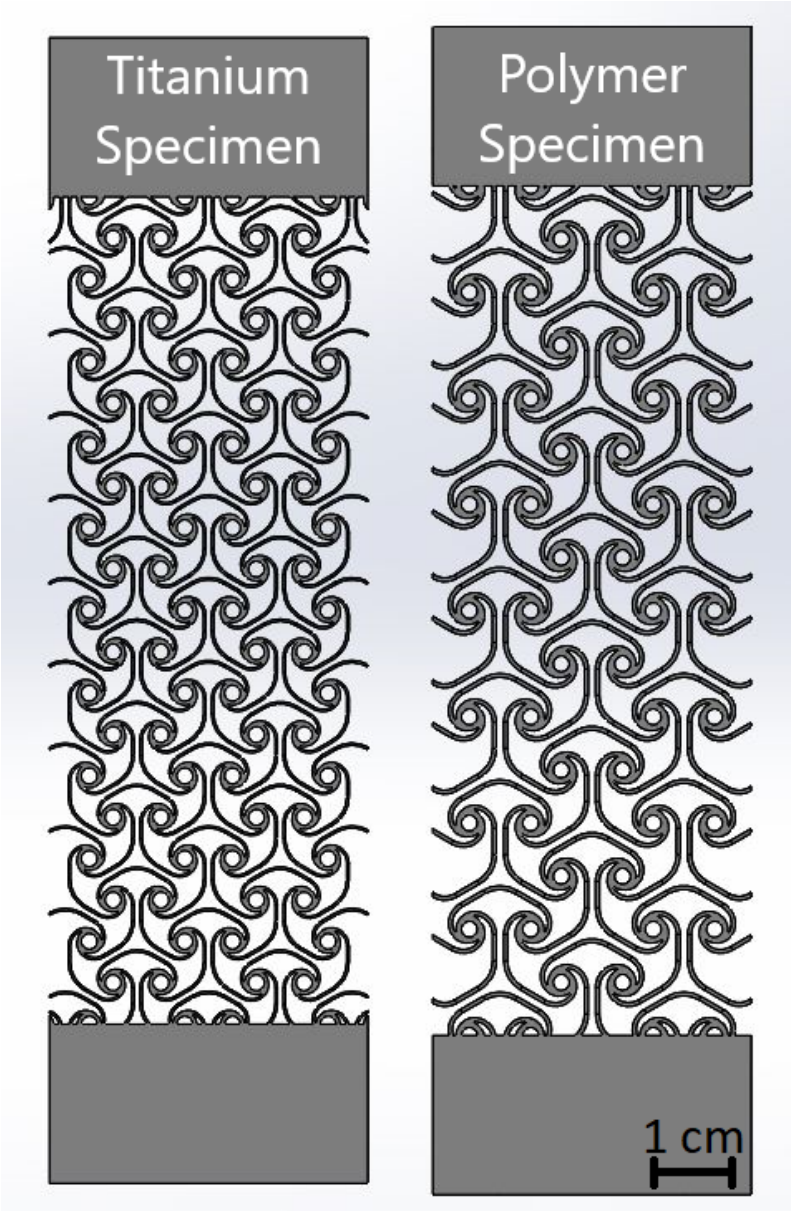

Figure 29: Design changes comparison.

Table 8: Summary of studied samples

Type of samples	Geometry	Tests	Purpose
FDM ABS scaffoldings	Hexagonal and square shapes that have three single patterns in each direction	• Manual pulling and pressing the scaffolding • FEA analysis numerical simulations	• Observe the deformation of the scaffoldings • Gain insight into the behaviour of the scaffoldings compared to the simulated behaviour
L-PBF PA 2200 preliminary scaffoldings	Hexagonal and square shapes that have three single patterns in each direction	Fixing the scaffoldings to the cranial fracture sample and manually pressing the scaffolding	Ascertain the resistance of the scaffoldings perpendicular to their plane
L-PBF PA 2200 tensile samples	Rectangular with clamping areas X-axis and Y-axis directions: • Wide-bow • Double-bow • Long-bow Parallel and skew direction: • Mirrored-spiral • Repeating-spiral • Linked-spiral	Mechanical tensile testing on the MTS Criterion tensile testing machine	• Obtain the mechanical properties of the PA 2200 scaffolding samples and compare them with the numerically calculated values • Observe the deformation due to elongation of the scaffolding • Locate the weak point in the scaffoldings
L-PBF Ti6Al4V	Rectangular with clamping areas X-axis and Y-axis directions: • Wide-bow • Double-bow • Long-bow Parallel and skew direction: • Mirrored-spiral • Repeating-spiral • Linked-spiral	Mechanical tensile testing on the MTS Criterion tensile testing machine	• Obtain the mechanical properties of the Ti6Al4V scaffolding samples and compare them with the numerically calculated values • Observe the deformation due to elongation of the scaffolding • Locate the weak point in the scaffoldings

The polymer DRS specimens were all placed horizontally in the build volume in the same direction to ensure consistency, as seen in Figure 30. The samples were built at different heights but with the same number of layers to fit all samples in the same build volume. It must be noted

that polymer samples were tested as-built without any post-processing, while the Ti6Al4V grade 23 samples were stress-relieved by being placed in a vacuum furnace at 200 °C for one hour followed by 650 °C for three hours and then cooled down to room temperature. After that, the Ti6Al4V grade 23 samples were heat treated in a vacuum furnace at a temperature of 200 °C for one hour, then at an increased temperature of 950 °C for two hours and cooled down to room temperature.

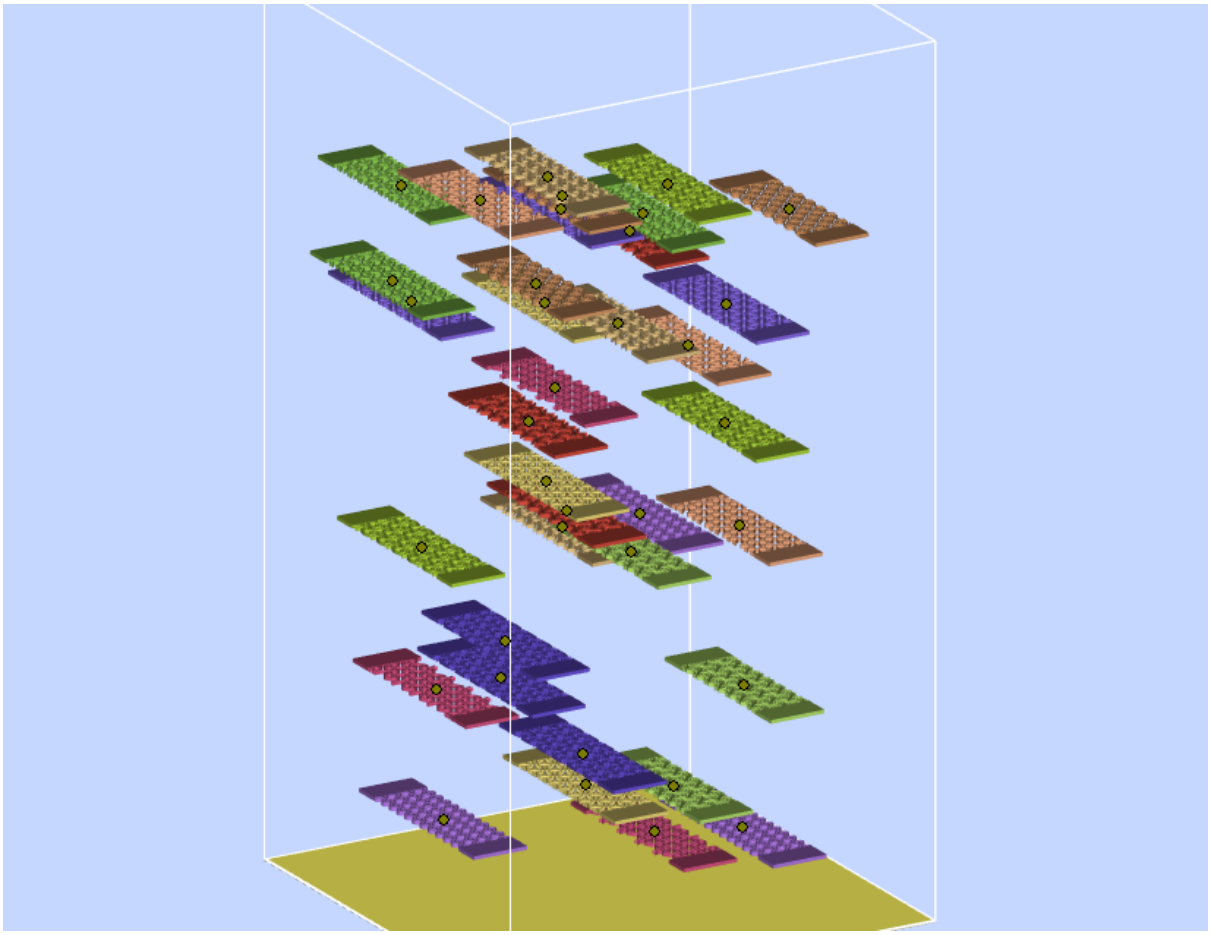

Figure 30: Build volume of the PA 2200 DRS specimens. The scaffolding samples are colour-coded, with each colour representing a scaffolding design.

3.6. Computer tomography scanning

X-ray micro-computed tomography was performed by a General Electric Vtomex L240 system, using 180 kV and 100 µA for X-ray generation, employing a 0.5 mm copper filter to reduce beam hardening. A total of 3000 step positions were used to record images around the object as it rotates through 360°. The first image is discarded at each step position, and the second image is recorded for improved image stability. The voxel size was set to 20 µm.

The data were processed and analysed in Volume Graphics VGSTUDIO MAX 3.4. An advanced surface determination function was used with modules for porosity analysis, wall thickness analysis and nominal-actual comparison. Porosity analysis was done with the VGDefX algorithm, with default settings and minimum pore size 2 x 2 x 2 voxels, i.e., pores > 40 µm in diameter. The wall thickness analysis function used the sphere method to find the local thickness at all points within the material walls. The nominal-actual comparison module allows visualising deviations from the CAD/design geometry. The overlap of the actual and CAD geometries was done with a best-fit registration, with manual adjustment for the deviations at the cut side of the sample. Due to the algorithm searching for nearest surfaces, some large deviations are falsely shown to be smaller because other surfaces are closer (there is no direct tracking of individual points). Despite this, the locations of the largest deviations are easily identified and indicated.

CHAPTER 4: POLYMER SCAFFOLDINGS

4.1. FDM ABS scaffoldings

Initial tests and simulations were done with polymer scaffoldings as they are easier to fabricate and test and are much more affordable. The ABS scaffoldings (Figure 24) were tested by physically pulling and pressing the scaffolding by hand to observe the deformation and behaviour of the scaffoldings. The following was observed:

- The wide-bow design exhibited good expansion and contraction in the horizontal axis, and it did not exhibit auxetic behaviour.
- The double-bow design exhibited less to no expansion and contraction in the horizontal axes and no auxetic behaviour; however, it did show promising dynamic behaviour in the vertical axis.
- The long-bow scaffolding exhibited exceptional expansion and contraction in the horizontal axes and auxetic behaviour in all horizontal directions; this design was deemed promising.
- The mirrored-spiral scaffolding exhibited expansion and contraction in the horizontal axes and semi-auxetic behaviour; auxetic behaviour was only displayed in the X-axis and Y-axis and not in other directions.
- The repeating-spiral exhibited expansion and contraction in the horizontal axes; however, it did not exhibit auxetic behaviour, and the scaffolding would displace asymmetrically when expanding.
- The linked-spiral exhibited auxetic behaviour in all directions; however, it did show less expansion and contraction in the horizontal axis, but it was also more robust in the scaffolding's perpendicular (vertical) direction; this design also proved promising for a viable DRS.

4.1.1. Stress distribution in wide-bow scaffoldings under loading

Finite element analysis (FEA) using Simulation Solutions (SolidWorks version 2020) was done on the preliminary specimens. To observe the deformation of the scaffolding when a load is applied perpendicular to the scaffolding, a fixed point was applied on the outermost screw mounting point, and a total force of 10 N perpendicular to the scaffolding was applied to the centre-most mounting holes (Figure 31). A custom ABS material with material properties from

Table 2 was used for the simulations. Finally, the preliminary stress distribution diagrams were set to display the von Mises chart between 0 MPa and 40 MPa.

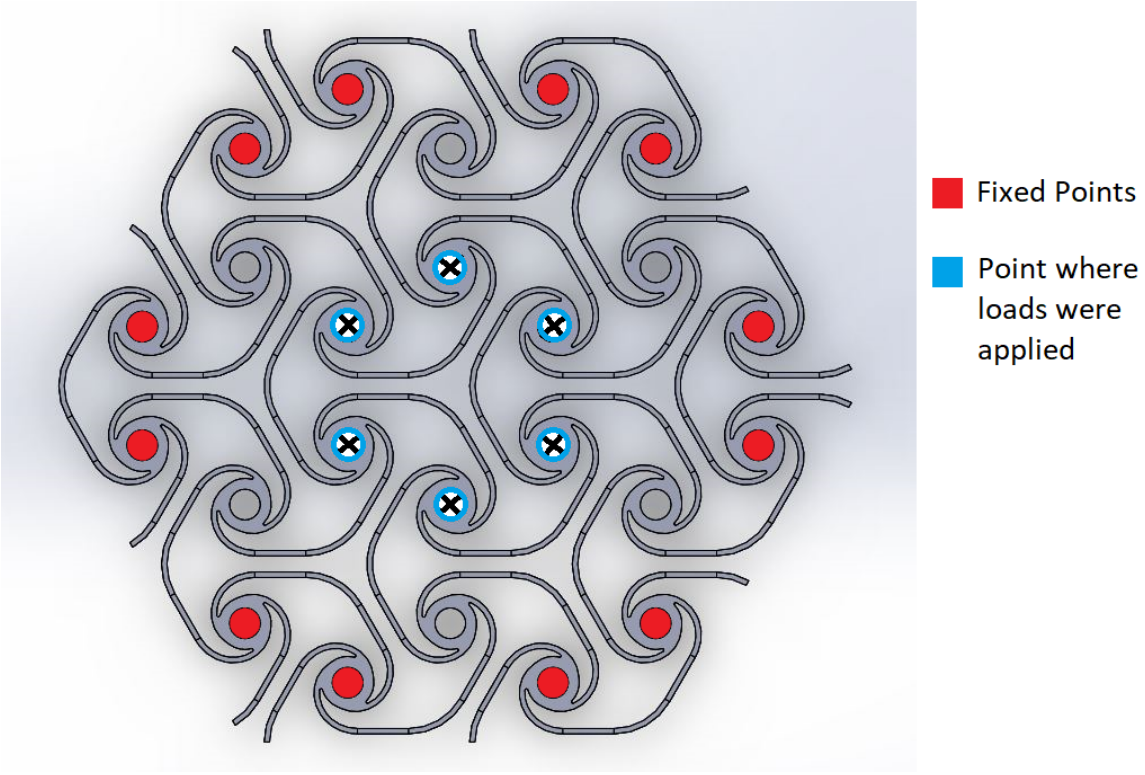

Figure 31: Preliminary simulation setup for the wide-bow scaffolding. The direction of loads is shown by ⊗.

The results from the FEA of the wide-bow show that the stresses were mainly concentrated in three directions parallel to the scaffolding geometry, as seen in Figure 32. The stress distribution graph (Figure 32a) shows that the stress concentration is higher than the yield strength of the material, meaning that this scaffolding will most likely fail under a 10 N load. It is also important to note that the highest stresses are at the spiral curve directly adjacent to the node. Also, note the arc where the nodes of the two arms have fewer stress concentrations, as indicated in Figure 32b-c.

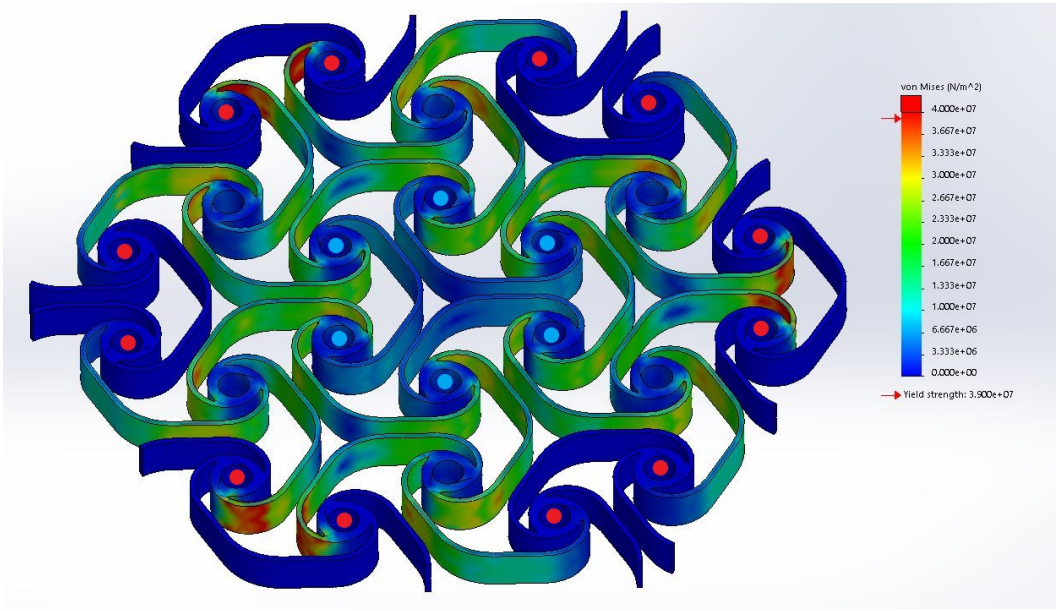

a

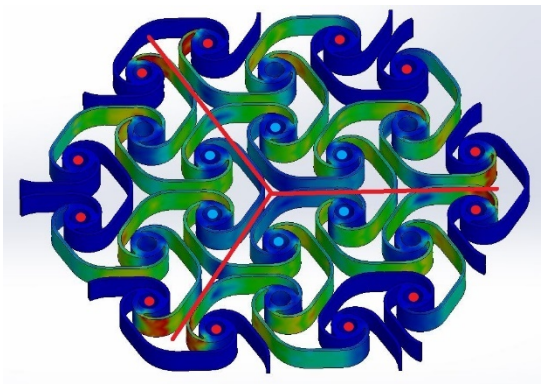

b

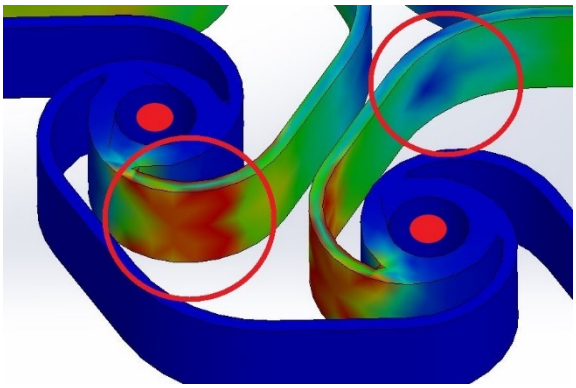

c

Figure 32: ABS wide-bow scaffolding FEA examinations (fixed nodes are indicated with red dots and the load applied nodes indicated with blue dots, the load is applied into and perpendicular to the scaffolding): a) stress distribution graph at a load of 10 N, b) load pathing through the scaffolding shown with the red line, c) a closeup of a high- and low-stress concentration.

4.1.2. Stress distribution in double-bow scaffoldings under loading

The stress distribution graph in Figure 33a for the double-bow shows the stress concentrations are significantly lower than the other scaffoldings. This is probably due to the double arms links unique to this scaffolding. When increasing the stress contrasts on the stress distribution graph, the highest concentrations of stress are on the inner walls of the arms of the scaffoldings, as seen in Figure 33b. In Figure 33c, the stresses are more evenly distributed to adjacent nodes and arms.

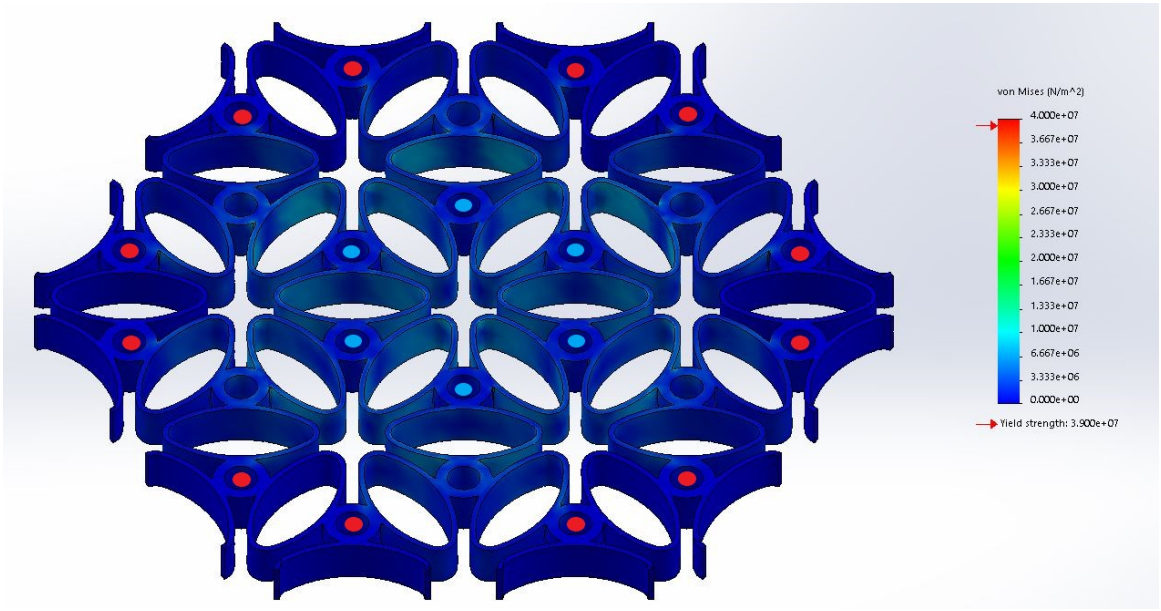

a

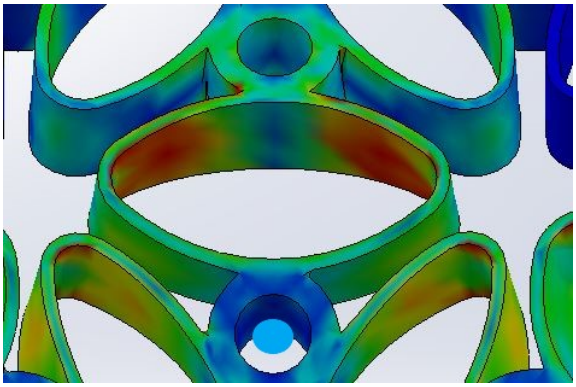

b

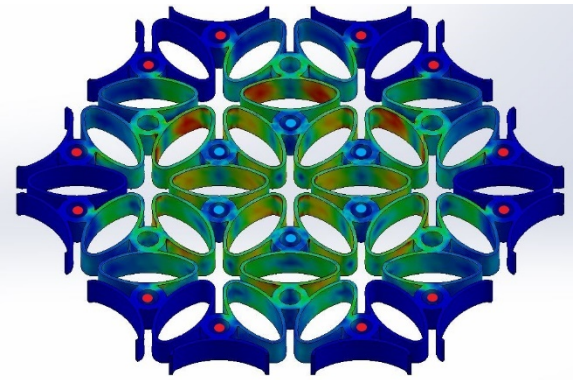

c

Figure 33: ABS double-bow scaffolding FEA examinations (fixed nodes are indicated with red dots and the load-applied nodes indicated with blue dots, the load is applied into and perpendicular to the scaffolding): a) stress distribution graph at a load of 10 N, b) closeup of stress concentrations, c) stress distribution graph with higher stress saturation to make the stress concentrations more visible.

4.1.3. Stress distribution in long-bow scaffoldings under loading

The long-bow scaffolding displayed much more and higher stress concentrations, as seen in Figure 34a. However, most stresses are distributed in three directions, similar to the wide-bow seen in Figures 34b-c. When focusing on one of the directions, it is clear to see a path that the stresses take between the fixed points and the point that has the load applied. The stresses are also more directed towards one side of the linked arms.

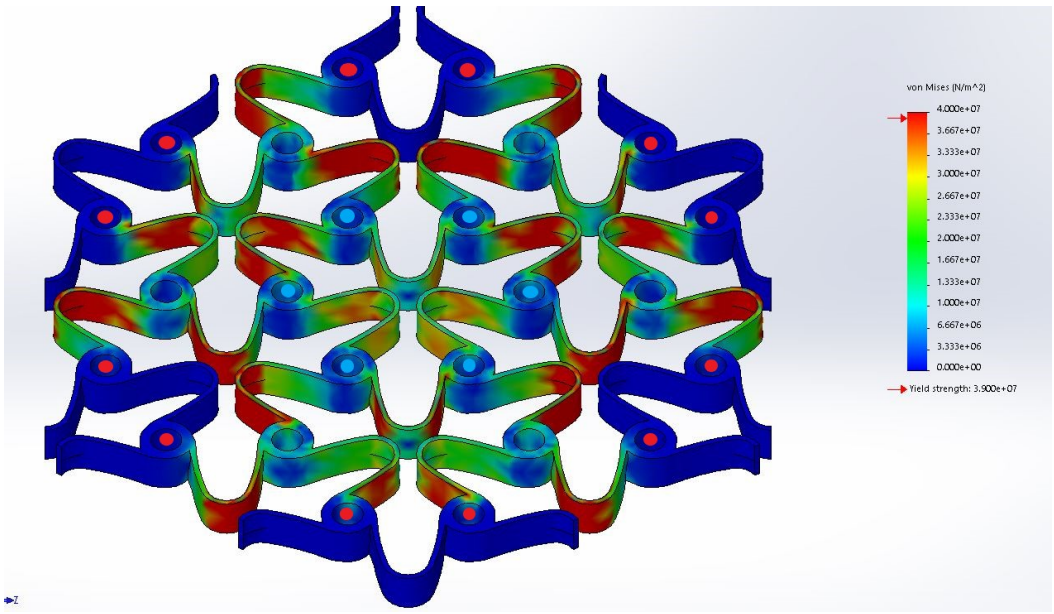

a

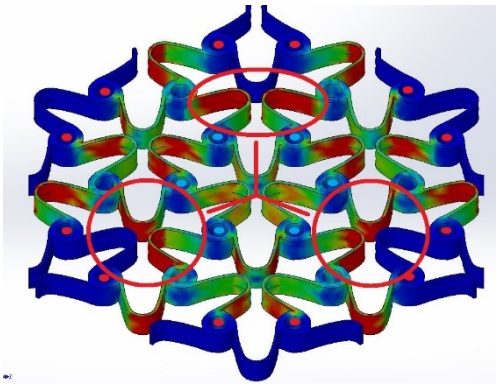

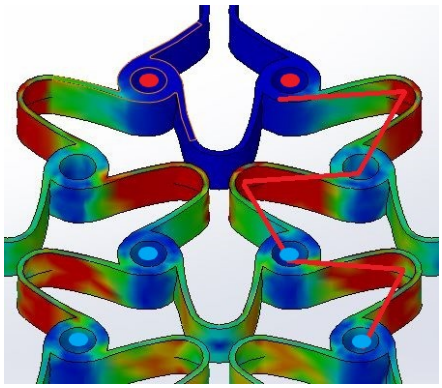

b c

Figure 34: ABS long-bow scaffolding FEA examinations (fixed nodes are indicated with red dots and the load-applied nodes indicated with blue dots, the load is applied into and perpendicular to the scaffolding): a) stress distribution graph at a load of 10 N, b) the majority of the stress in the graph is in the indicated three directions, c) stress path from the load to fixed points.

4.1.4. Stress distribution in mirrored-spiral scaffoldings under loading

From observing the stress distribution diagram for the mirrored-spiral in Figure 35, it seems that the stresses are more evenly spread out in the axis parallel to the scaffolding geometries, likely due to the square pattern of the scaffolding. When focusing on a single pattern, the greatest stress concentration is directed to the spiral part of the arms directly after the nodes, as seen in Figure 35b. Another phenomenon to note is shown in Figure 35c, where there is a high

concentration of stress on the fixed node's side of the linked arm but a low concentration on the side that is closer to the node that has the load.

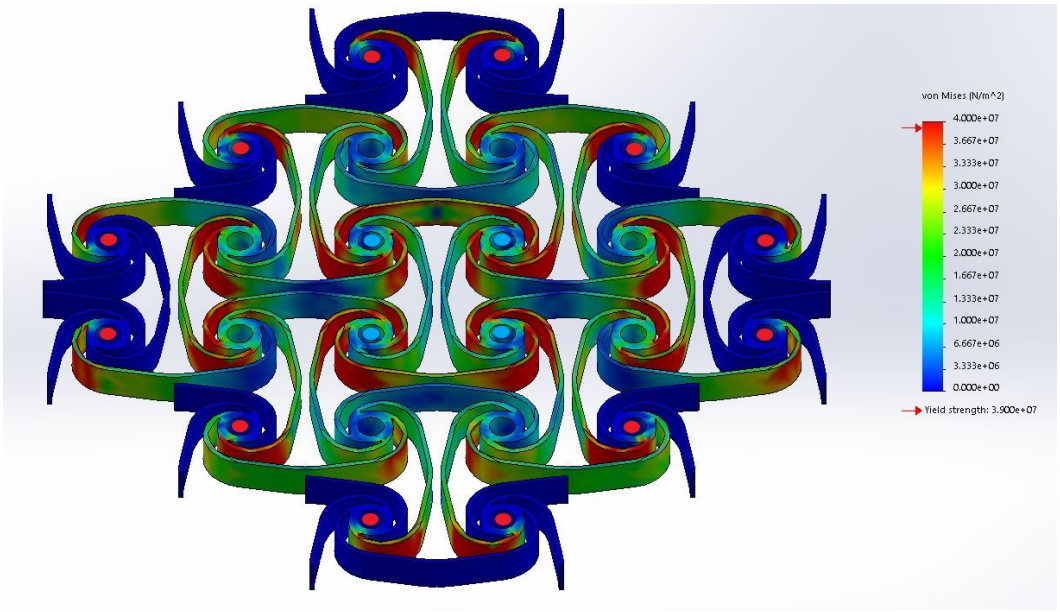

a

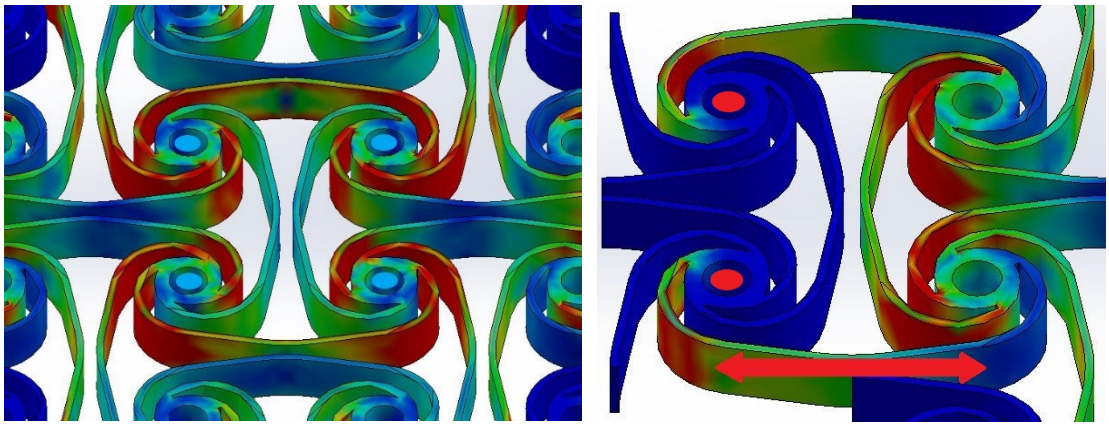

b c

Figure 35: ABS mirrored-spiral scaffolding FEA examinations (fixed nodes are indicated with red dots and the load applied nodes indicated with blue dots, the load is applied into and perpendicular to the scaffolding): a) stress distribution graph at a load of 10 N, b) view of the largest single pattern stress concentrations, c) phenomenon where there is a high-stress concentration on the fixed side of the link but a low-stress concentration on the other end of the link.

4.1.5. Stress distribution in repeating-spiral scaffoldings under loading

The repeating-spiral mainly had low-stress concentrations except for a couple of very high concentrations, as seen on the stress distribution diagram in Figure 36. A very peculiar

phenomenon was found in the repeating-spiral, as indicated in Figure 36b. The high concentrations of stress were only found on one of the four arms of each node, followed by an arm with a low concentration of stress. Furthermore, the respective concentration point would cycle counterclockwise to the next arm of the next node. It was also observed that on the outer nodes of the scaffolding, there was a high concentration of stress at the start of the arm where the node is connected; however, at the centre of the arm where the two node's arms link, there was a low concentration of stress, as seen in Figure 36c.

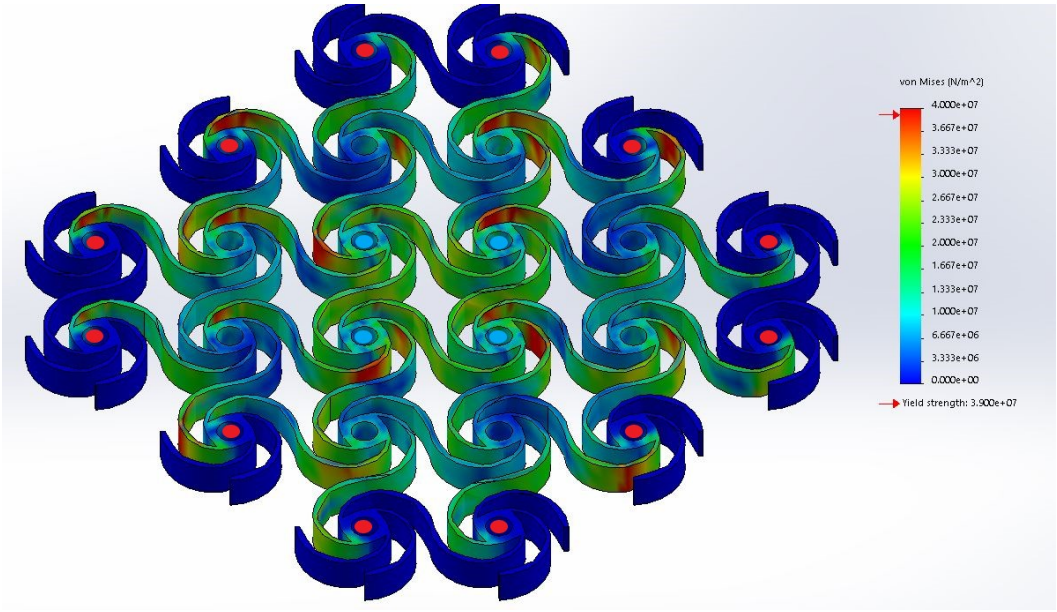

a

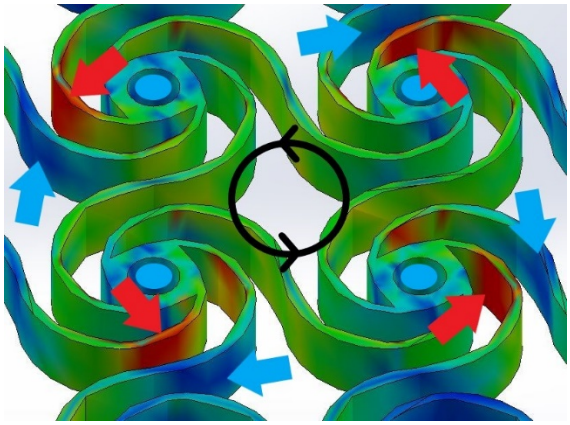

b

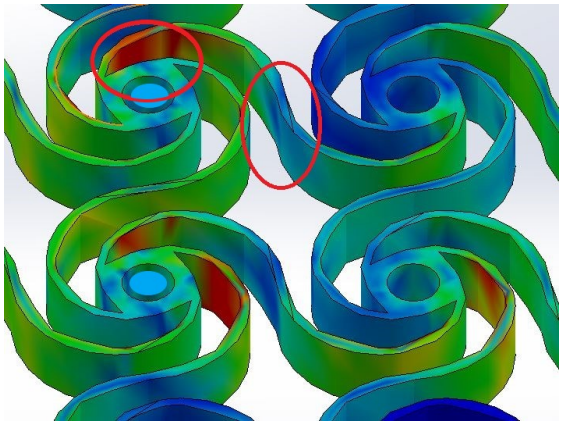

c

Figure 36: ABS repeating-spiral scaffolding FEA examinations (fixed nodes are indicated with red dots and the load applied nodes indicated with blue dots, the load is applied into and perpendicular to the scaffolding): a) stress distribution graph at a load of 10 N, b) high- and low-stress concentrations found on the centre single pattern, c) a high-stress concentration can be seen at the end of the links with a low concentration at the centre of the link.

4.1.6. Stress distribution in linked-spiral scaffoldings under loading

Lastly, the linked-spiral stress distribution diagram in Figure 37 shows that all the stresses are relatively evenly distributed around the scaffolding, except for the nodes in the centre. Focusing on the centre single pattern in Figure 37b, the high-stress concentrations are located in some type of mirrored pattern reflecting over the X- and Y-axis. Furthermore, the substantially lower stress concentrations on the linked arm sections can be observed, as indicated in Figure 37c.

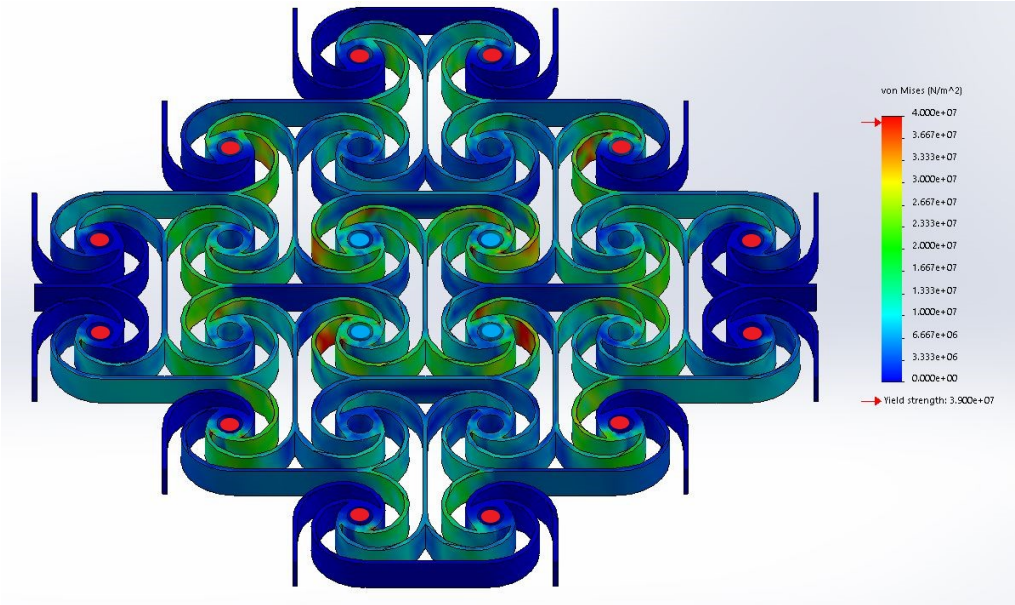

a

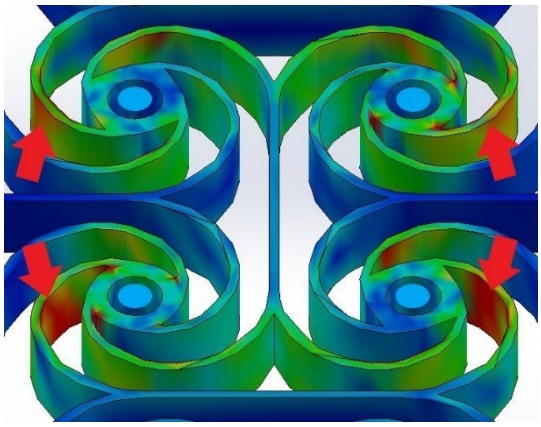

b

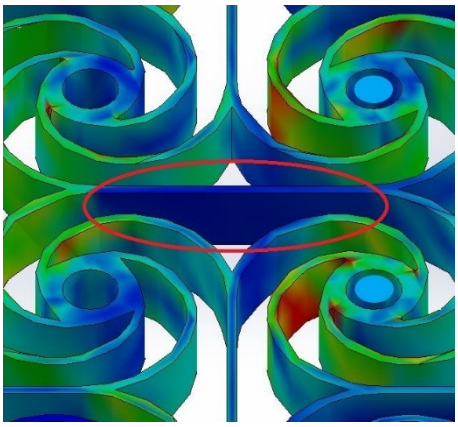

c

Figure 37: ABS linked-spiral scaffolding FEA examinations (the fixed nodes are indicated with red dots and the load applied nodes indicated with blue dots, the load is applied into and perpendicular to the scaffolding): a) stress distribution graph at a load of 10 N, b) a closer look at the stress concentrations in the centre single pattern, c) observation of the lower stress found in the linked arm sections.

4.1.7. Summary

The above simulations were done with fixed points on the outer nodes and loaded points perpendicular to the scaffolding on the centre single pattern nodes for a total load of 10 N for each scaffolding. The hexagonal scaffoldings have distributed their loads in three primary directions, but the square patterns distributed the load more evenly across the scaffolding. All the scaffolding can be observed to have stress concentrations above the material's yield point, meaning that all the scaffoldings would fail at the high-stress concentrations except for the double-bow scaffolding, which is the only scaffolding that did not show stress concentrations above the material's yield point. However, this also means that the double-bow scaffoldings are by far the stiffest of the six designs and would most likely have the least expansion and contraction, which will most likely result in bone resorption in the cranial scaffolding implant. Furthermore, the wide-bow and the linked-spiral showed the most optimal stress distribution across their scaffoldings and are the most promising with the least and smallest stress concentrations.

4.2. SLS scaffoldings from PA 2200

4.2.1. Preliminary tests

A cranial fracture sample obtained from an earlier CT scan of a child who suffered a severe injury to the head can be seen in Figure 38. The fractured area was sectioned from the rest of the skull and printed on the SLS machine to test the PA 2200 scaffoldings in a similar environment to that for which they are intended. Figure 39 shows the SLS printed cranial sample for testing. The data from the CT scan of the fracture was not perfect and did contain a flaw; however, for a mock test, it was still acceptable. The holes in the nodes are made to fit a 3 mm screw to mount the scaffolding to the skull.

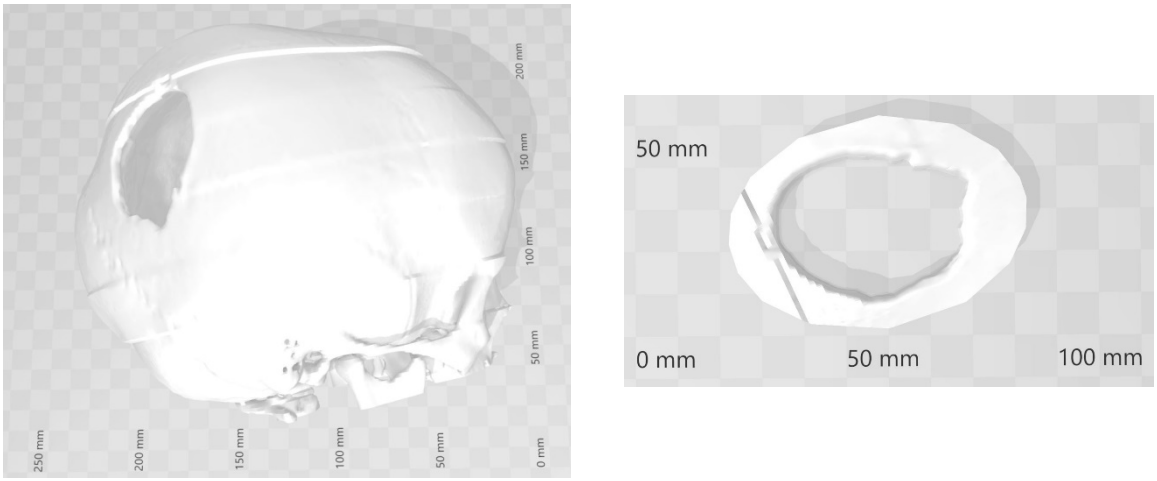

a b

Figure 38: STL model of cranial fracture sample: a) full model, b) sectioned area.

The cranial sample tests were done by first drilling several equally spaced holes around the fractures in the cranial sample (Figure 39a). The scaffolding was then mounted one hole at a time, selecting holes that stretched the scaffolding the least. This is to reduce the stress in the scaffolding and prevent bone resorption. Once the scaffolding was successfully mounted, the excess material was removed by cutting it off. Figure 39b shows an example of the linked-spiral scaffolding after mounting and removing the excess material. With this technique, the scaffoldings can be fabricated as large, ready-to-use grids, and the doctors can cut out the required size section, mount the scaffolding and remove the excess material.

a (b)

Figure 39: L-PBF PA 2200 fracture sample for testing.

The mock tests proved that most of the SLS PA 2200 scaffolds were too weak and did not provide sufficient protection when an approximate force of 10 N was applied perpendicular to the scaffolding. The scaffoldings did not fail but did displace roughly 2 cm into the cranial, which is unacceptable. However, the scaffoldings exhibiting auxetic behaviour did prove to be sturdier:

- The double-bow design had no displacement in the horizontal axes; however, it did behave much more dynamically vertical to the scaffolding, which is not useful for this particular test but does seem promising for other applications.
- The wide-bow design was much weaker than was expected. However, titanium is a much stronger and stiffer material than nylon, and therefore this scaffolding might still be promising in titanium if other scaffoldings are too stiff.
- The linked-spiral pattern proved to be the most exceptional, exhibiting perpendicular protection while still expanding and contracting in horizontal directions.

When the simulated results were compared with the preliminary test done on the cranial fracture sample under the 10 N load, the simulations indicated that the stress on the scaffolding links would surpass the material yield point and most likely fail, yet in the preliminary tests, none of the scaffoldings failed under a 10 N load. However, the preliminary scaffoldings did displace substantially more than the simulations calculated. These results suggest that due to the scaffoldings' highly complex geometry, the simulations are not reliable enough to be used to simulate these scaffoldings.

4.2.2. Tensile testing of wide-bow samples

X-axis wide-bow samples

The tensile testing of the X-axis specimen of the wide-bow design is shown in Figure 40. Here it can be seen that the nodes do unwind as intended to allow high elongation. It is also noted that only the nodes in the centre rows of the specimens were affected by the force applied due to the outer nodes not being indirectly connected to the grip extensions. However, if the pattern was wider, theoretically, a similar deformation should be observed at an offset up or down; therefore, the result should be similar.

Figure 41 shows the deformation of the wide-bow X-axis single pattern during the tensile test. The pattern starts as a hexagon and then begins to expand vertically (in the direction that the tensional force is applied) with minimum change in the horizontal direction (the direction

perpendicular to the tensional force). The single pattern continues to deform vertically to a point at Figure 41e where it is almost rectangular. As the elongation continues, the centre bow between the nodes starts to deform inwards in the opposite direction to its initial resting form, and the horizontal distance between the nodes starts to decrease. This is most likely due to the opposed unwinding directions of the two nodes connected to the centre bows.

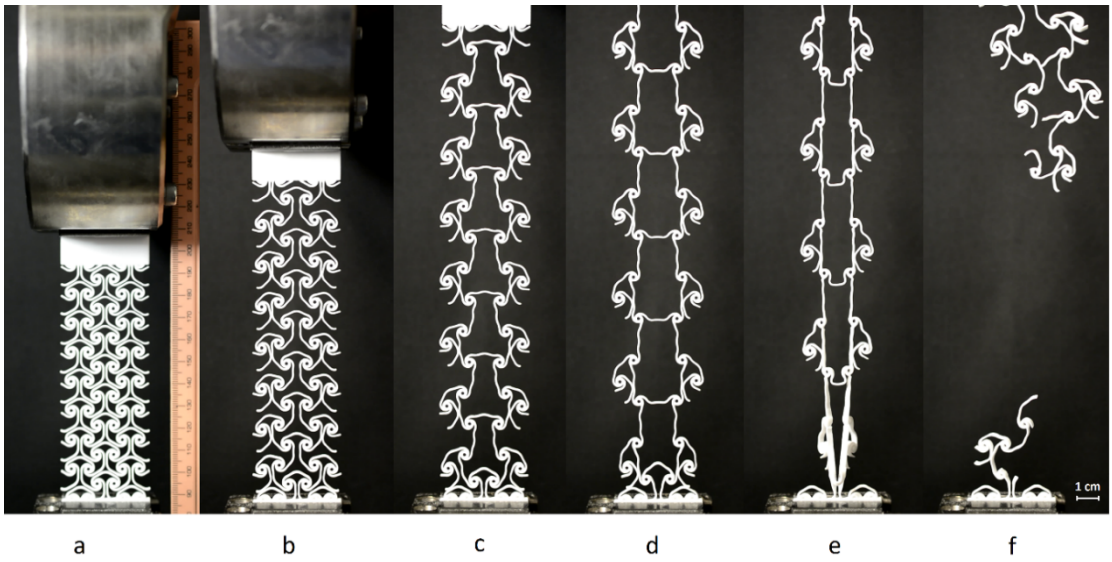

Figure 40: Different stages of deformations of the wide-bow X-axis sample during tensile testing: a) sample clamped in the grips in a natural position, b–d) scaffolding elongation, e) scaffolding moments before failure, f) scaffolding after the failure occurred.

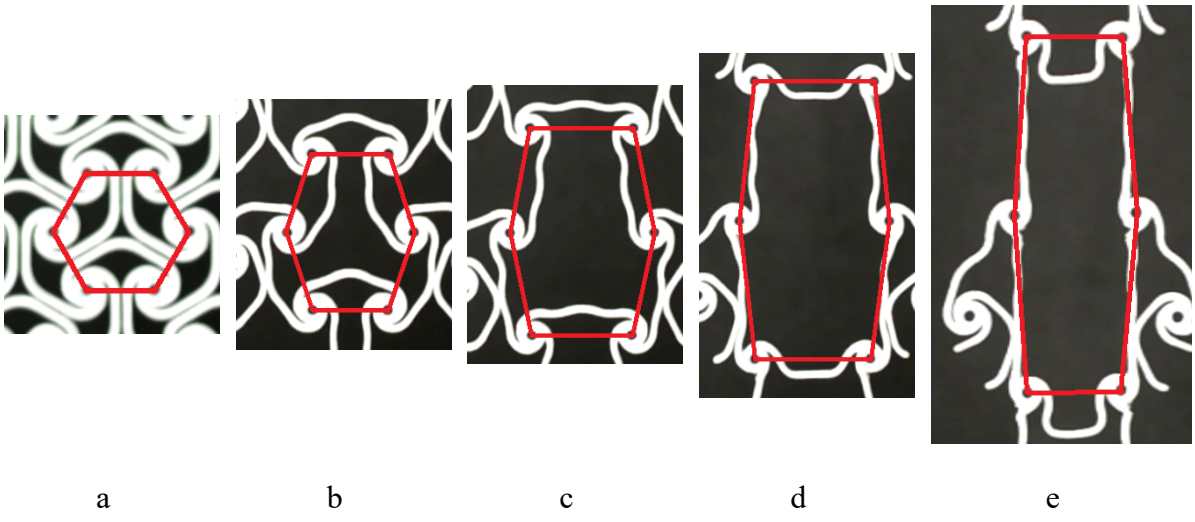

Figure 41: Wide-bow X-axis single pattern deformation (red lines connect the nodes of the single pattern and indicate the deformation of the single pattern): a) single pattern in its natural state, b–d) single pattern deforming as the scaffolding elongates, e) single pattern moments before failure occurred.

Finally, from observation of the failure of the specimen, it is noted that most of the failure points were at the ends of the links, where the arms connect to the nodes, as seen in Figure 42. A closeup of Figure 41e on Figure 42a shows how the nodes have unwound so much that a tear starts forming on each node where the arms connect to the nodes. Also, note that two of three links of all the nodes in the force path are fully unwounded and are now straight. Figure 42b shows the failure point on the specimen before failure occurred.

a b c

Figure 42: Close-up view of wide-bow X-axis: a) shows the links tearing from the nodes and are indicated with red arrows, b) where the scaffolding failed indicated with red lines, c) scaffolding after the failure occurred.

Y-axis wide-bow samples

Next is the tensile testing of the Y-axis wide-bow, and Figure 43 shows the progression of the tensile test. Once again, the nodes can be observed to unwind as intended. However, due to the opposing directions of adjacent nodes, the scaffolding seems to be folding in on itself, unlike the X-axis, which was expanding due to the opposing rotational directions. It also appears that in this direction, more nodes were in the force path and being deformed. This is most probably only due to the layout of the scaffolding pattern.

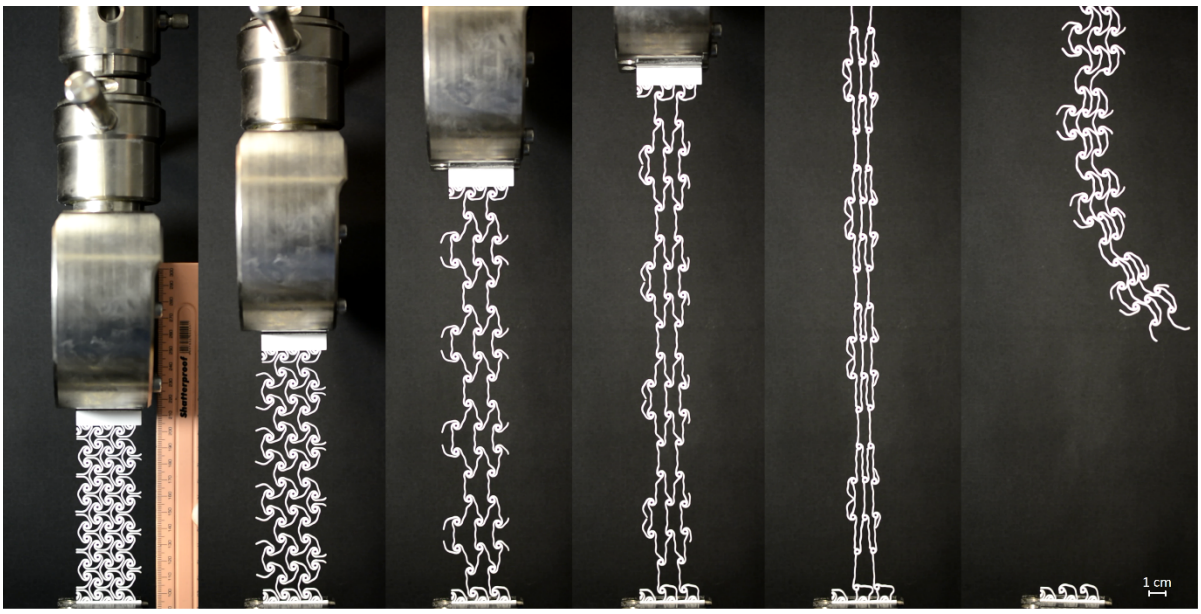

Figure 43: Different stages of deformations of the wide-bow Y-axis sample during tensile testing: a) sample clamped in the grips in a natural position, b–d) scaffolding elongation, e) scaffolding moments before failure, f) scaffolding after the failure occurred.

Figure 44 shows the deformation of the wide-bow Y-axis single pattern during the tensile test. The pattern starts as a hexagon and then starts to expand vertically and contract horizontally. The deformation continues until a point in Figure 44e right before failure where the single pattern is in a very tall and narrow shape. In this direction, there was no centre bow to stop the pattern from collapsing into the vertical centre, resulting in a tall and narrow shape.

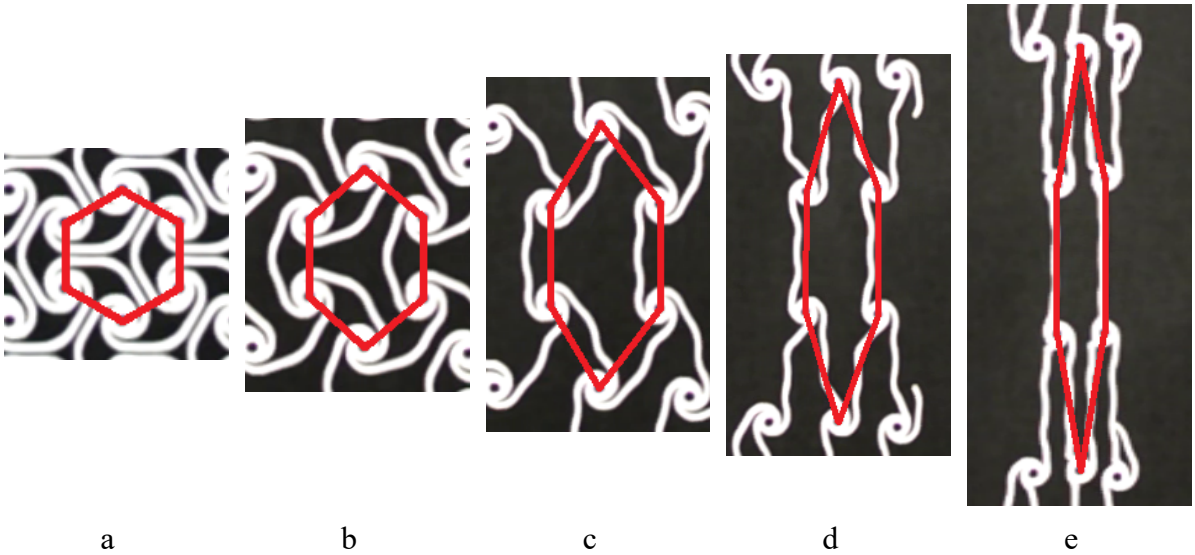

Figure 44: Wide-bow Y-axis single pattern deformation (red lines connect the nodes of the single pattern and indicate the deformation of the single pattern): a) single pattern in its natural state, b–d) single pattern deforming as the scaffolding elongates, e) single pattern moments before the failure occurred.

A closer look at Figure 44e stage (Figure 45) indicates that the failure points are at the ends of the links where the arms connect to the nodes, once again due to the extent that the nodes unwound, causing tearing. Figure 45a shows tearing forming along the specimen. The outer nodes seem to be under less stress than the centre nodes, likely due to only two arms being under tension, allowing the nodes to rotate further. The amount of rotation of the nodes can be observed on the outer node arms, which made an almost 180° rotation. Figure 45b shows the failure point and Figure 45c a closeup of the failure point after failure.

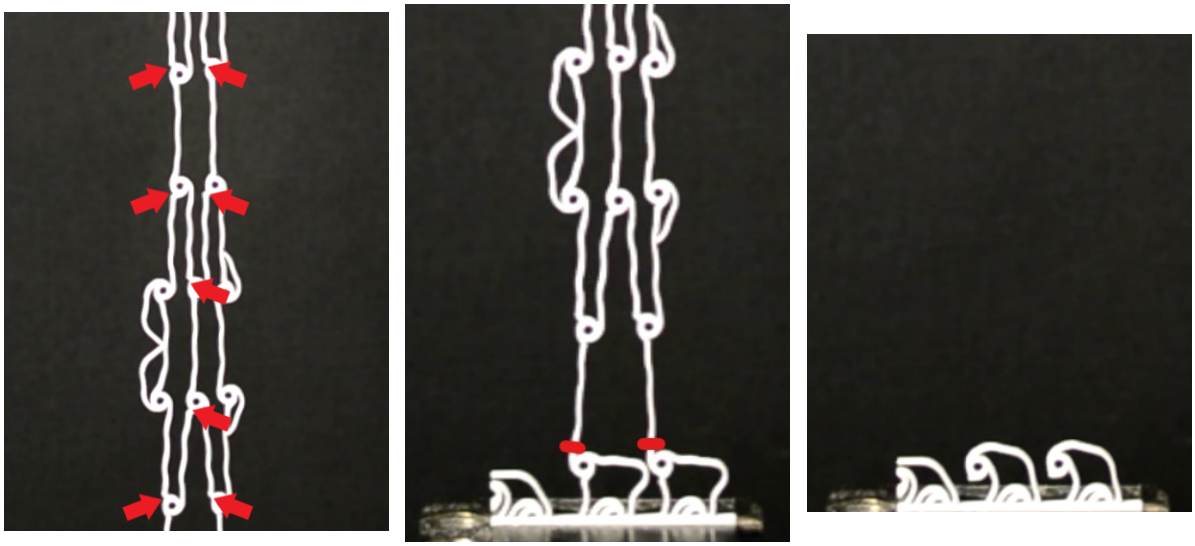

a b c

Figure 45: Wide-bow Y-axis closeup shows: a) links tearing from the nodes and are indicated with red arrows, b) where the scaffolding failed, indicated with red lines, c) scaffolding after the failure occurred.

Comparison of tensile behaviour of X- and Y-axis wide-bow samples

The force-displacement graph below in Figure 46 combines the X- and Y-axis data for the wide-bow scaffolding. This graph proves that the Y-axis specimen could deform further, reaching a displacement of 275 mm compared to the 241.3 mm of the X-axis. However, the X-axis could withstand a higher peak force of 39.96 N before breaking than the 28.7 N of the Y-axis. The data indicates that the X-axis had a relative elongation[1] of 215.5% and the Y-axis of 245.6%. Both curves have a relatively long growth curve, with the X-axis having a shorter but

[1] Relative elongation called in the present work "an elongation" is the ratio of the grips' displacement to the initial length of the scaffolding sample (%).

higher curve than the Y-axis (it is stiffer). An irregularity can be seen at about 220 mm on the X-axis curve. This corresponds to the approximate time the scaffolding started deforming in the camera's direction, as seen in Figure 41e.

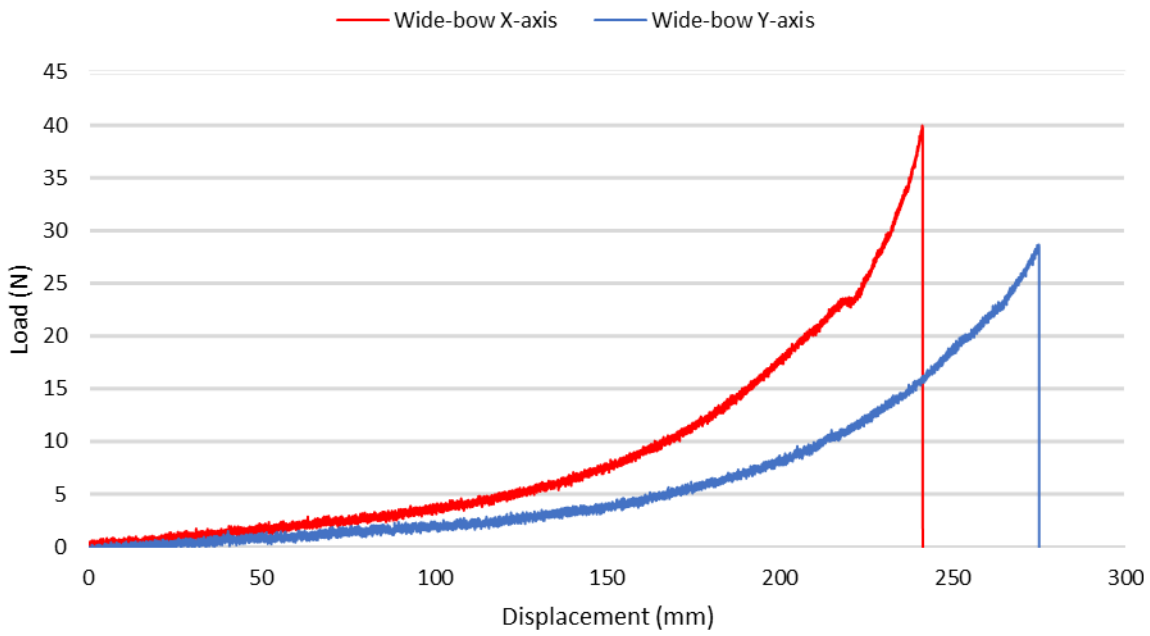

Figure 46: Load-displacement curves of wide-bow tensile specimens.

The graph shows that the wide-bow scaffolding is stronger in the X-direction but can displace further in the Y-direction.

4.2.3. Tensile testing of double-bow samples

X-axis double-bow samples

The double-bow tensile test process can be seen in Figure 47. This scaffolding was designed to deform the arms instead of rotating the node, which reduces the distance it can displace but allows it to be significantly stronger. The width of the scaffolding shrinks as it elongates due to the deformation of the arms from a shallow oval to almost rectangular and then back to an oval but in a direction perpendicular to its original direction.

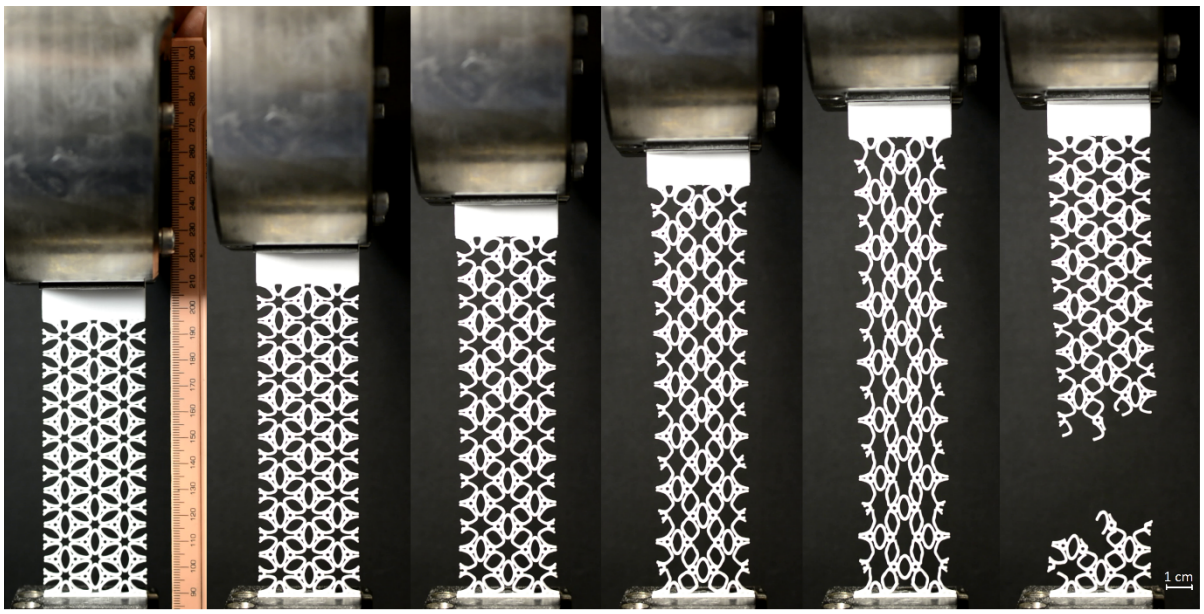

Figure 47: Different stages of deformations of the double-bow X-axis sample during tensile testing: a) sample clamped in the grips in a natural position, b–d) scaffolding elongation, e) scaffolding moments before failure, f) scaffolding after the failure occurred.

Figure 48 shows the deformation of the double-bow X-axis single pattern during the tensile test. There is no significant change in the horizontal distance between the two top and bottom nodes of the single pattern. Most of the deformation seems to be in the links between the top and bottom nodes connecting to the centre nodes. The shape of the single pattern starts as a hexagon but then slowly deforms into an almost rectangular shape.

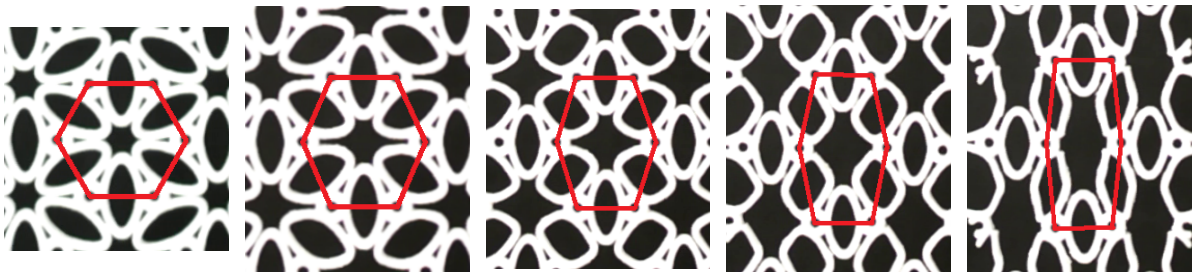

Figure 48: Double-bow X-axis single pattern deformation (red lines connect the nodes of the single pattern and indicate the deformation of the single pattern): a) single pattern in its natural state, b–d) single pattern deforming as the scaffolding elongates, e) single pattern moments before failure occurred.

A closeup of Figure 47e in Figure 49a highlights once more that the potential failure points are at the section where the arms connect to the nodes. However, the tearing was most likely caused due to the extensive deformation of the links between the nodes. The centre vertical oval-

shaped double links had minimum deformations. Also, note that there are tears on the outer node connections; this most probably indicates substantial tension in the outer nodes, meaning that the scaffolding effectively distributes the tensional forces to all the nodes. Figure 49b shows the failure point in red and the point that further tore off during failure in blue. Figure 49c is a closeup of the failure points after the failure occurred.

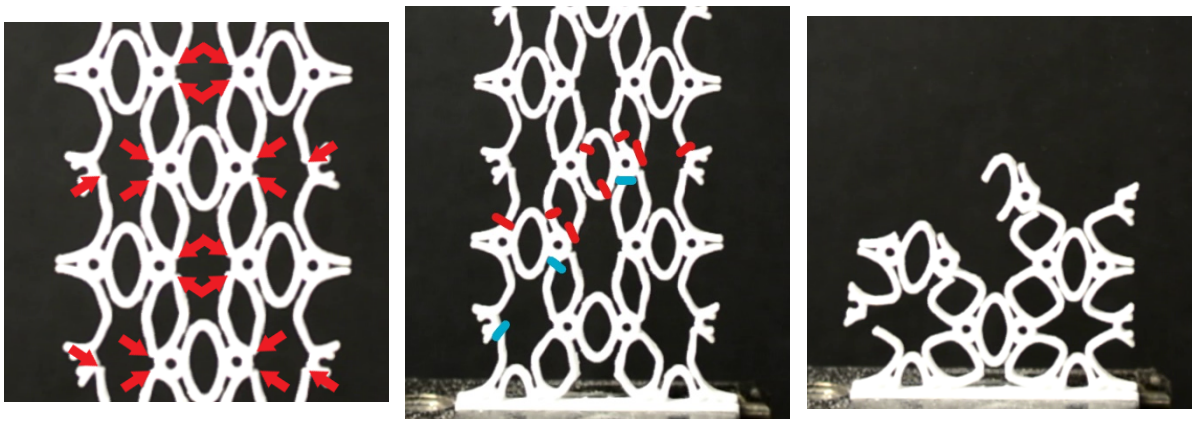

a b c

Figure 49: Double-bow X-axis closeup shows a) the links tearing from the nodes and are indicated with red arrows, b) where the scaffolding failed indicated with red lines, c) scaffolding after the failure occurred.

Y-axis double-bow samples

The tensile test progression for the Y-axis specimen of the double-bow scaffolding is shown in Figure 50. The links between the nodes can again be seen deforming instead of the nodes unfolding. However, it seems to be the centre horizontal oval that is doing most of the displacement in this direction, which is entirely the opposite of the X-axis, where the centre oval was vertical and had minimum deformation. The other ovals seem to be deformed as well, but not as much as the centre ovals. Also, note how the width of the scaffolding mostly stays constant until the stage of deformation shown in Figure 50d, where there is a significant reduction in width likely due to the deformation of the links between the nodes.

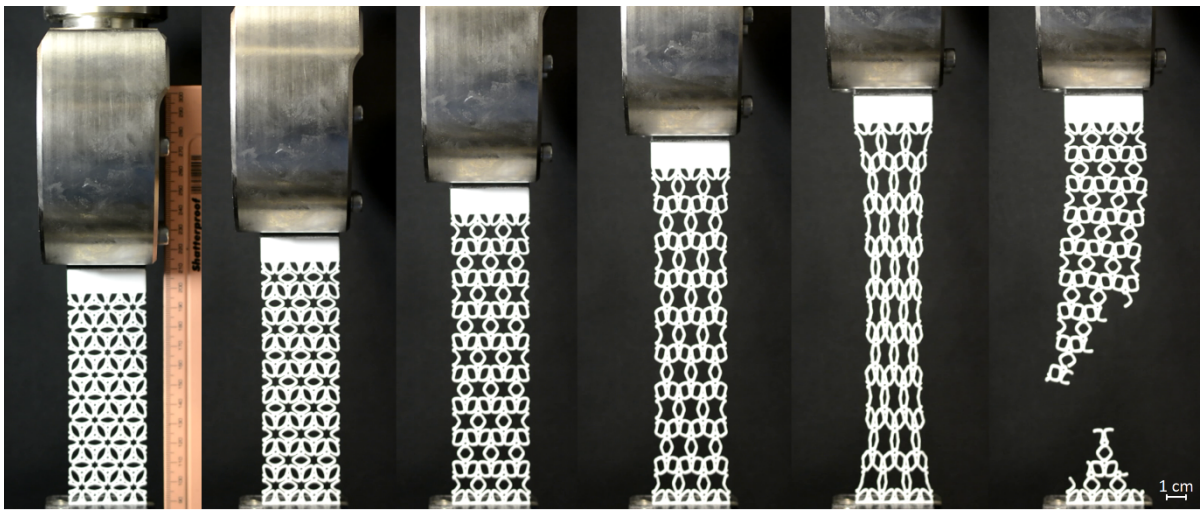

Figure 50: Different stages of deformation of the double-bow Y-axis sample during tensile testing: a) sample clamped in the grips in a natural position, b–d) scaffolding elongation, e) scaffolding moments before failure, f) scaffolding after the failure occurred.

Figure 51 show the deformation of the double-bow Y-axis single pattern during the tensile test. There was deformation in the vertical and horizontal direction in the single pattern below, with the most significant deformation being in the vertical direction. The single pattern started as a hexagon and deformed into a taller, narrower hexagon.

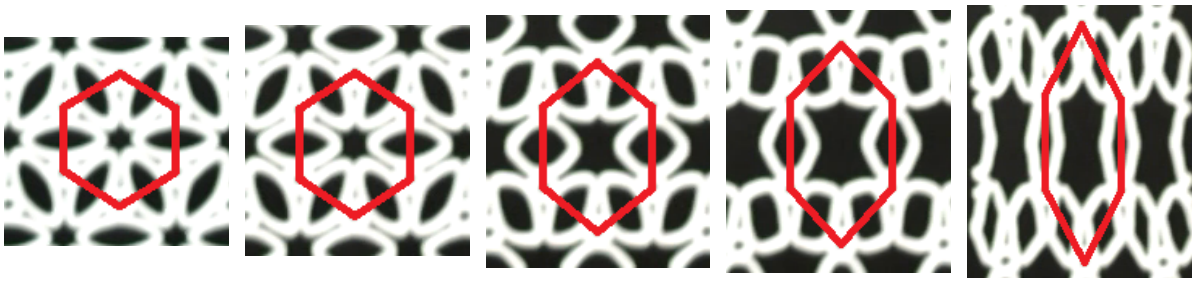

Figure 51: Double-bow Y-axis single pattern deformation (red lines connect the nodes of the single pattern and indicate the deformation of the single pattern): a) single pattern in its natural state, b–d) single pattern deforming as the scaffolding elongates, e) single pattern moments before failure occurred.

A close-up look at Figure 50e in Figure 52a shows how the links deformed before breaking, creating tears at the ends of the links. The original horizontal ovals have been fully stretched into vertical ovals; the side ovals have also been deformed into almost rectangular shapes. Figure 52 b) shows the failure point before failure occurred, and Figure 52c a closeup of the failure points after the failure occurred.

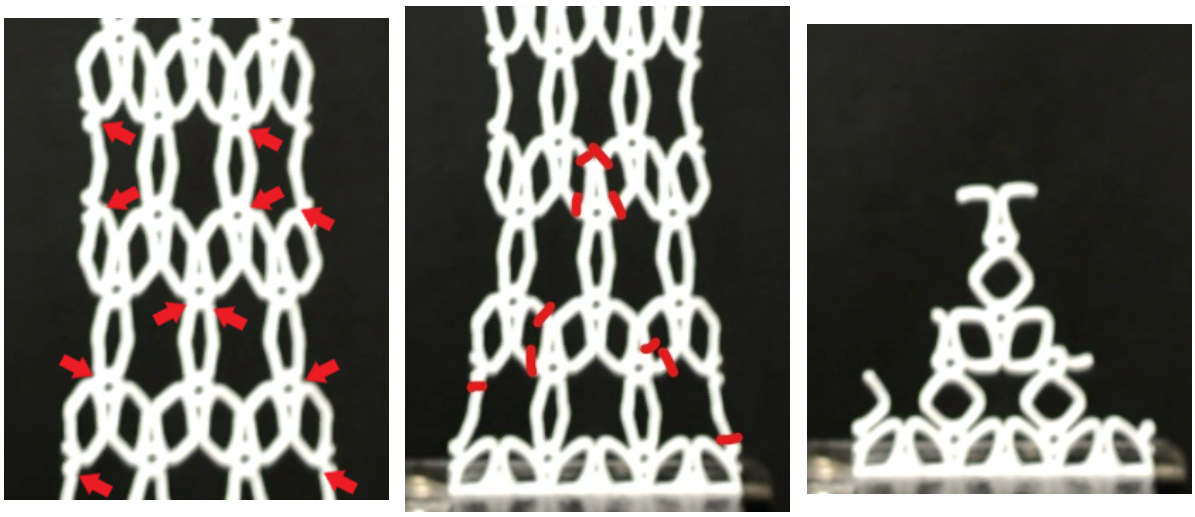

a b c

Figure 52: Double-bow Y-axis closeup shows a) links tearing from the nodes indicated with red arrows, b) where the scaffolding failed indicated with red lines, c) scaffolding after the failure occurred.

Comparison of tensile behaviour of X- and Y-axis double-bow samples

The graph in Figure 53 shows the X- and the Y-axis data combined for the double-bow scaffoldings. The Y-axis of the scaffolding was able to withstand a greater amount of force before breaking at 110.6 N compared to 84 N of the X-axis. The Y-axis was able to elongate further before breaking, reaching a total of 88.2 mm compared to 72.4 mm of the X-axis specimen.

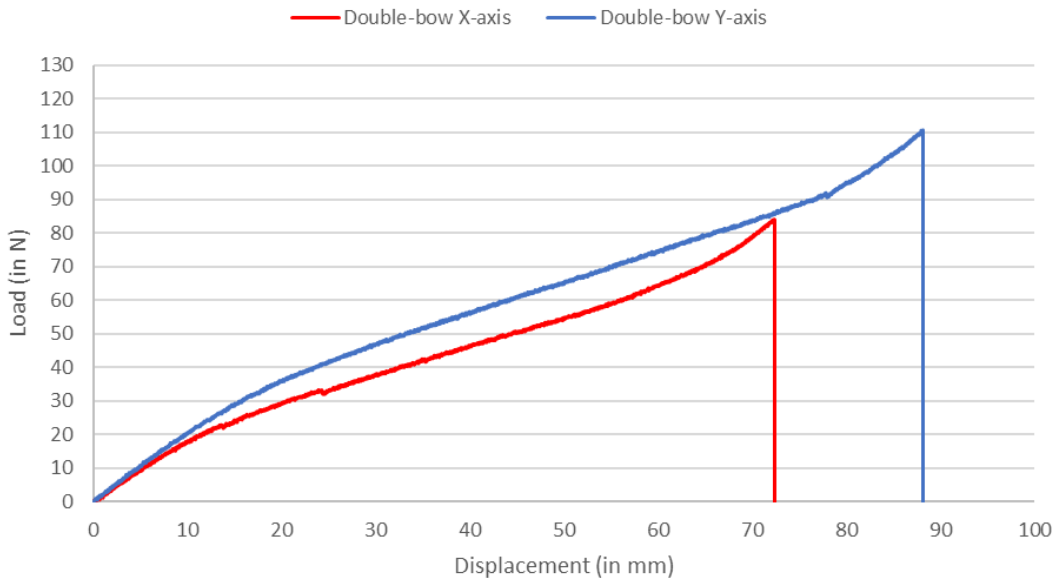

Figure 53: Double-bow tensile test data graphs.

The data also shows that the X-axis had a relative elongation of 64.6%, and the Y-axis had an elongation of 78.8% before breaking. Both curves had strong growth at the start, which decreased, but then levelled out and started to grow again before they broke. The shape of both graphs look similar, the only difference being that the graph for the Y-axis is larger than the X-axis. Small irregular spikes can be observed at 15 mm, 25 mm and very slightly at 35 mm, most likely due to cracks in the material.

4.2.4. Tensile testing of long-bow samples

X-axis long-bow samples

The last of the hexagonal scaffoldings is the long-bow, and the tensile test progression for the X-axis specimen is shown in Figure 54. The nodes rotated to unwind upwards in the structures above them as the specimen elongated. The long-bow was designed to use both the deformation of the links and the rotation of the nodes to allow the scaffolding to elongate.

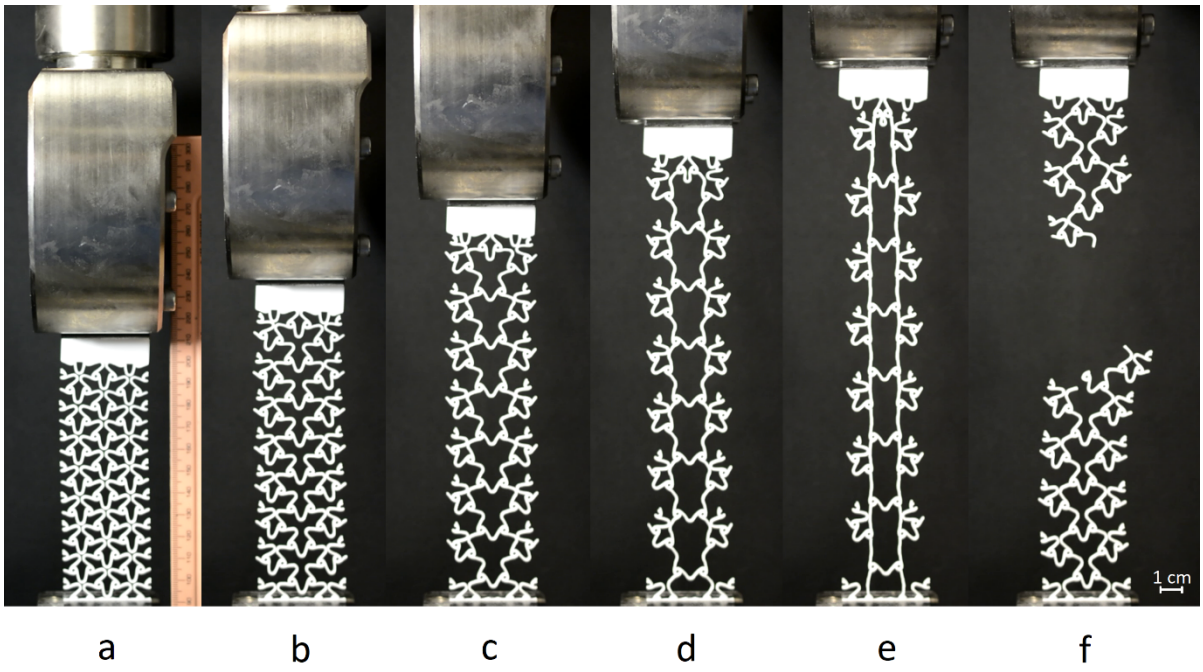

Figure 54: Different stages of deformation of the long-bow X-axis sample during tensile testing: a) sample clamped in the grips in a natural position, b–d) scaffolding elongation, e) scaffolding moments before failure, f) scaffolding after the failure occurred.

As seen in Figure 54, the scaffolding worked as intended. In the preliminary tests, this scaffolding displayed auxetic behaviour; however, during the tensile testing of the X-axis direction, the scaffolding only displayed minor auxetic behaviour at the start (Figure 54b),

where the width of the scaffolding increased ever so slightly. For the rest of the test, the width of the scaffolding can be seen to decrease (Figure 54c–e).

Figure 55 shows the deformation of the long-bow X-axis single pattern during the tensile test. The single pattern did start to expand auxetically as intended. However, once the initial deformation of the links was done and the nodes started to rotate, the single pattern started to elongate in the vertical direction, and the width started to shrink. Similarly to the other hexagonal scaffoldings, the shape of the single pattern in this direction seems to go from hexagonal to almost rectangular before breaking.

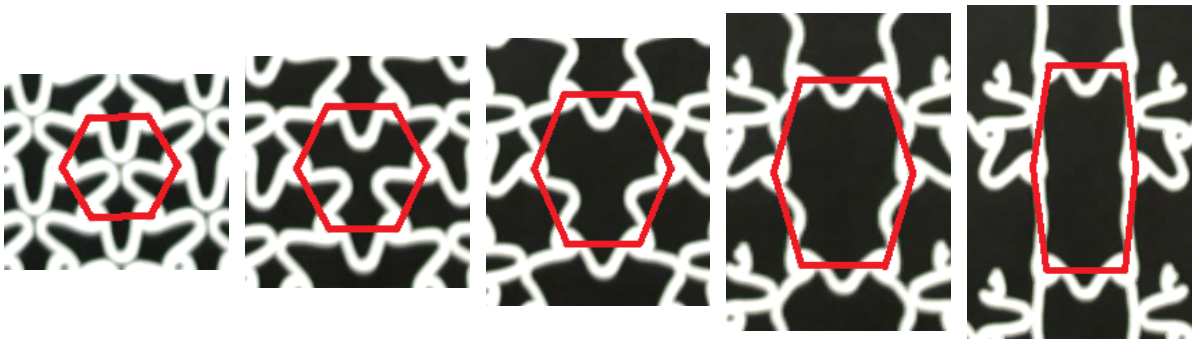

a b c d e

Figure 55: Long-bow X-axis single pattern deformation (red lines connect the nodes of the single pattern and indicate the deformation of the single pattern): a) single pattern in its natural state, b–d) single pattern deforming as the scaffolding elongates, e) single pattern moments before the failure occurred.

A closeup of Figure 53e in Figure 56a shows how the links have deformed before breaking. The links are fully stretched out and are most likely the cause of the tearing due to the scaffolding not being able to deform any other way. The centre link can also be seen supporting the nodes from fully expanding outwards. In Figure 56b, the failure point is marked in red, and the point that tore off further during failure is blue. Figure 56c is a closeup of the failure points after the failure occurred.

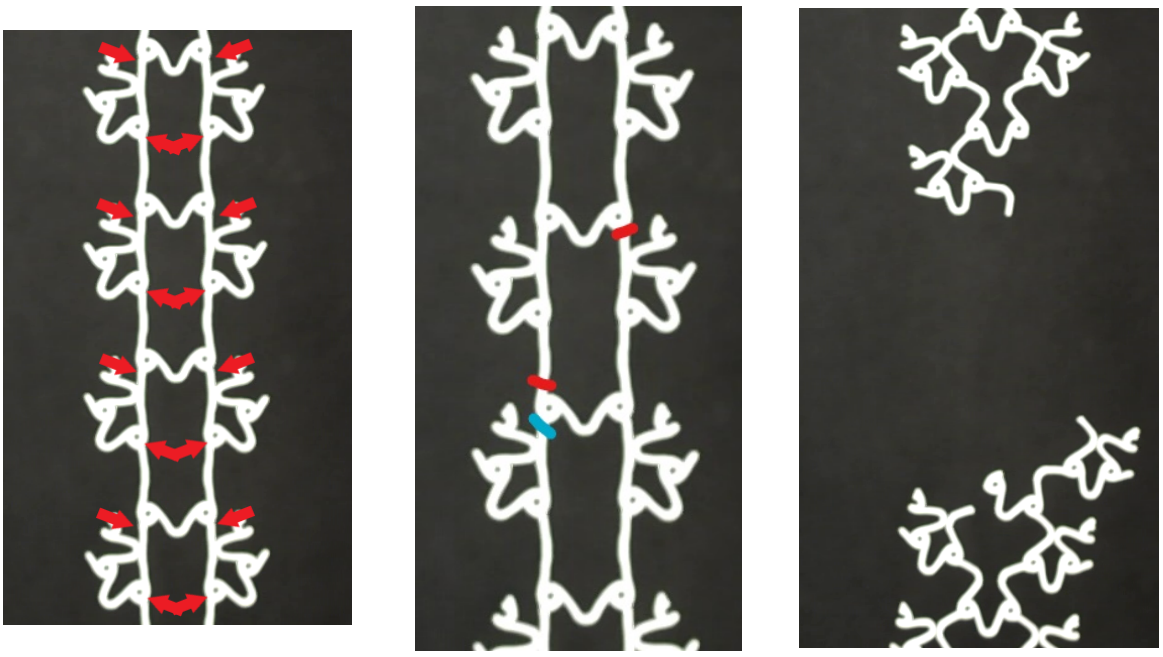

a b c

Figure 56: Long-bow X-axis closeup shows a) the links tearing from the nodes and are indicated with red arrows, b) where the scaffolding failed indicated with red lines, c) scaffolding after the failure occurred.

Y-axis long-bow samples

The tensile test progression for the long-bow Y-axis can be seen in Figure 57. From these images, it can be observed that the width of the scaffolding does increase horizontally as the specimen is vertically stretched, which confirms auxetic behaviour. The scaffolding continues to increase in width until Figure 57c, where it starts to reduce significantly in width before breaking at Figure 57f. This behaviour of the scaffolding seems to be more auxetic than the above-described scaffoldings, and it does seem that the patterns interlock much more effectively. More of the links and nodes in this axis are used to support the tensile force. The images of the specimen during the tensile test reveal how much the node rotated, as the legs on the right-hand side of the specimen seem to have rotated about 90° before breaking.

Figure 58 shows the deformation of the long-bow Y-axis single pattern during the tensile test. The single pattern started as a hexagon and then deformed into a larger hexagon in an auxetic manner as the tensile test continued. In Figure 58c, the hexagon started to deform more vertically than horizontally, and this continued as the tensile test progressed. The single pattern can also be seen collapsing in on itself by significantly decreasing the width of the single pattern. As the scaffolding elongated, the deformation of the links caused all the nodes to

expand outwards uniformly. However, as the elongation continued, the nodes started to rotate in on themselves, and the links were almost fully stretched out, causing them to pull the nodes horizontally closer together.

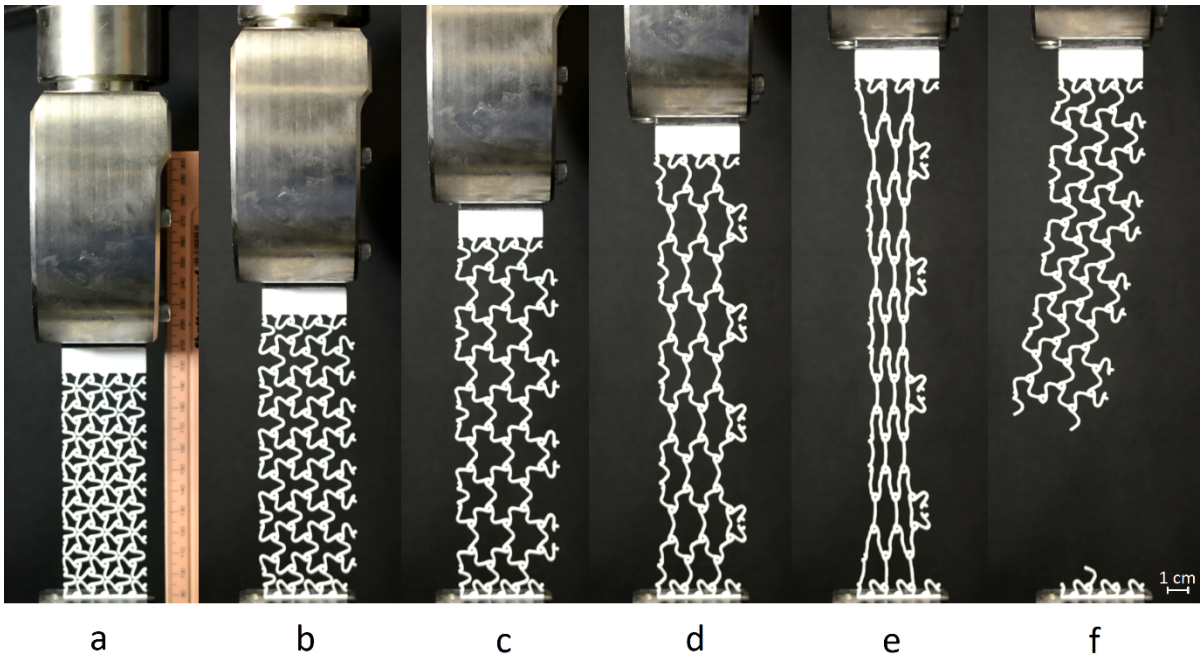

Figure 57: Different stages of deformations of the long-bow Y-axis sample during tensile testing: a) sample clamped in the grips in a natural position, b–d) scaffolding elongation, e) scaffolding moments before failure, f) scaffolding after the failure occurred.

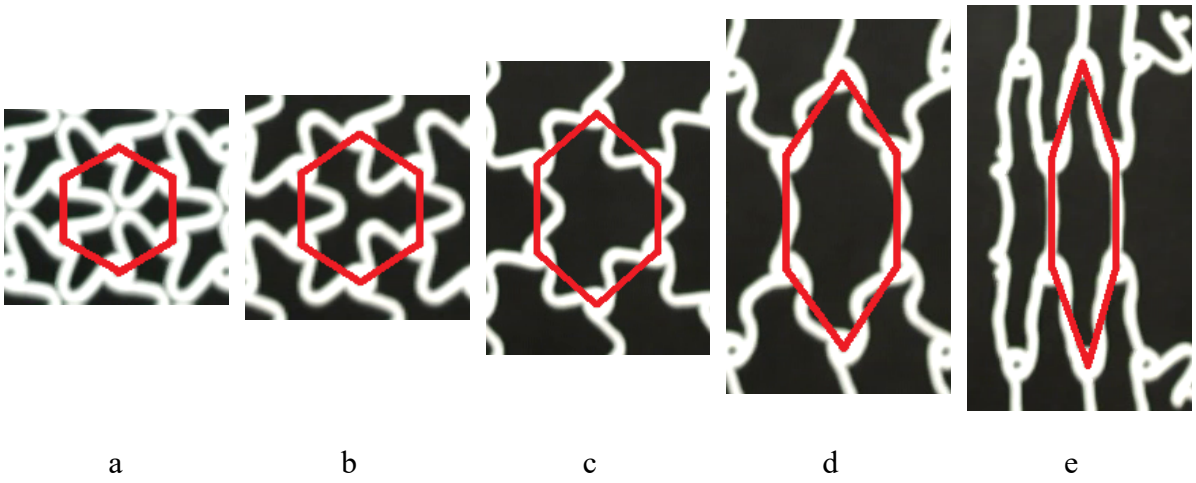

Figure 58: Long-bow Y-axis single pattern deformation (red lines connect the nodes of the single pattern and indicate the deformation of the single pattern): a) single pattern in its natural state, b–d) single pattern deforming as the scaffolding elongates, e) single pattern moments before the failure occurred.

A close-up view of Figure 57e in Figure 59a shows how the links have deformed before breaking. The links can be seen fully stretched out and is most likely the cause of the tearing due to the scaffolding not being able to deform any other way. More links and nodes can be seen to deform in this direction, meaning that the forces are better distributed. Figure 59b shows the failure points of the specimen before failure occurred, and Figure 59c shows the failure points after the failure occurred.

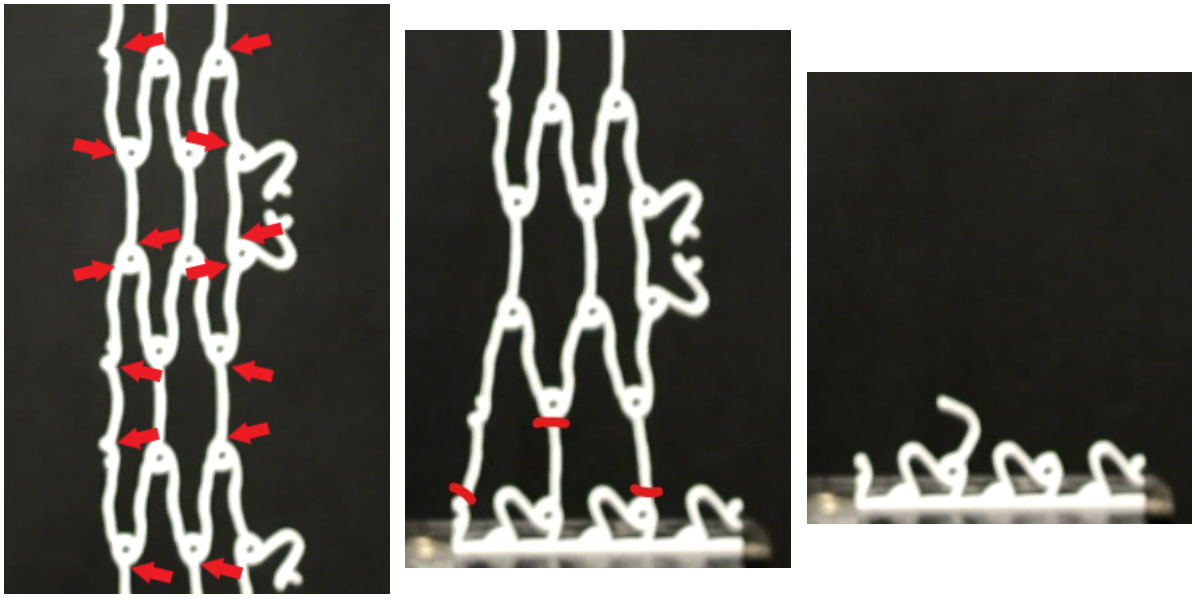

a b c

Figure 59: Long-bow Y-axis closeup shows a) the links tearing from the nodes and are indicated with red arrows, b) where the scaffolding failed indicated with red lines, c) scaffolding after the failure occurred.

Comparison of tensile behaviour of X- and Y-axis long-bow samples

The graph below in Figure 60 shows the X- and Y-axis data combined for the long-bow scaffoldings. The Y-axis of the scaffolding was able to withstand a higher amount of force before breaking at 66.1 N, compared to 44.7 N of the X-axis. The Y-axis could also elongate further before breaking, reaching 142.85 mm compared to 122.74 mm of the X-axis specimen. The data also shows that the X-axis had an elongation of 109.6%, and the Y-axis reached 127.55% before breaking. Both curves look similar to exponential growth curves, with only the X-axis having an irregularity closer to the point of failure at around 115 mm. Both curves seem to have almost identical data for the first 70–80 mm of elongation, which could be very promising as this could mean that the scaffolding is isotropic for its initial deformation.

However, further testing will be required at more angles, and multiple directional forces pulling on the scaffolding simultaneously will also be needed to confirm this.

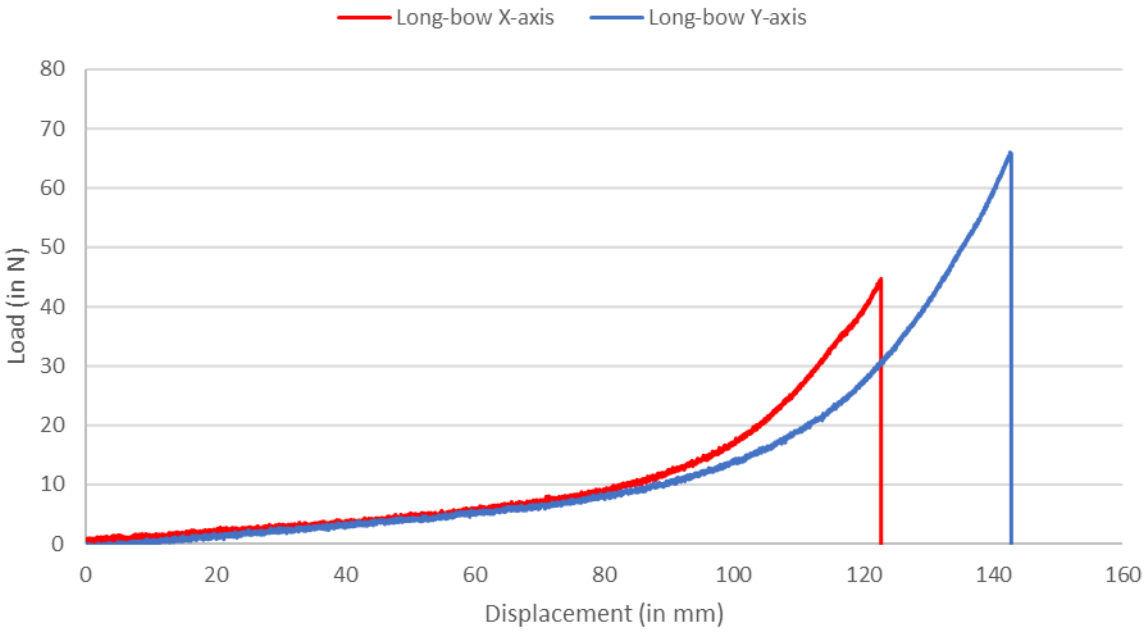

Figure 60: Long-bow tensile test data graphs.

4.2.5. Tensile testing of mirrored-spiral samples

Mirrored-spiral parallel-axis tensile tests

The first of the square pattern scaffoldings is the mirrored-spiral, and the progression of the parallel-axis tensile test can be seen in Figure 61. In the images below, the mirrored-spiral parallel-axis can be seen to be auxetic as it horizontally expands and vertically elongates. Figure 61a and Figure 61b show how much the scaffolding expanded horizontally with only a small amount of elongation. Figure 61c shows the maximum width the scaffolding reached before shrinking again. The rate at which the scaffolding shrank its width with elongation is much slower than when it expanded. In Figure 61d, the specimen's width is longer than its initial size and only before failure at Figure 61f did the width of the specimen shrink to less than its original size. Figure 61f shows that the specimen did not fail completely; instead, failures were distributed around the specimen.

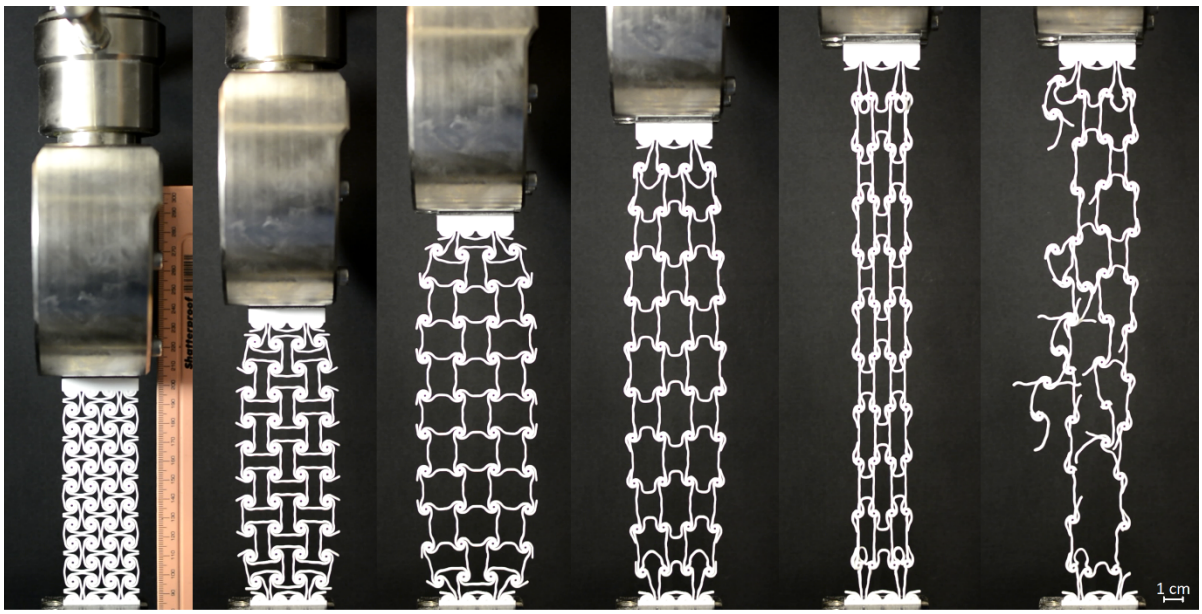

Figure 61: Different stages of deformation of the mirrored-spiral parallel-axis sample during tensile testing: a) sample clamped in the grips in a natural position, b–d) scaffolding elongation, e) scaffolding moments before failure, f) scaffolding after the failure occurred.

Figure 62 shows the deformation of the mirrored-spiral parallel-axis single pattern during the tensile test. The images show how the four nodes on the single pattern rotate inwards, causing the single node to expand. At the start of the test, the single pattern is seen as square and retains this shape while elongating until the stage shown in Figure 62c, where the single pattern starts to elongate more vertically than expand horizontally. This deformation continues as the nodes rotate past 90°, where the pattern starts to shrink horizontally as the nodes start pulling them horizontally closer.

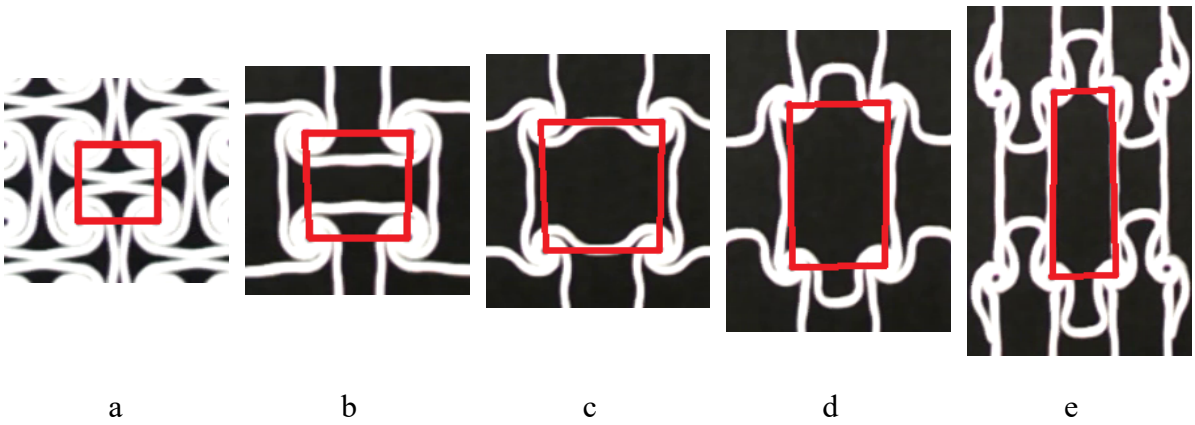

Figure 62: Mirrored-spiral parallel-axis single pattern deformation (red lines connect the nodes of the single pattern and indicate the deformation of the single pattern): a) single pattern in its natural state, b–d) single pattern deforming as the scaffolding elongates, e) single pattern moments before the failure occurred.

A close-up view of Figure 61e in Figure 63a shows how the links have deformed before breaking. This results from the links being fully straightened from the tensile force on the specimen, causing the tears to form as there was no other way for the specimen to deform. Figure 63b shows the failure points of the specimen before failure occurred, and Figure 63c shows the failure points after the failure occurred.

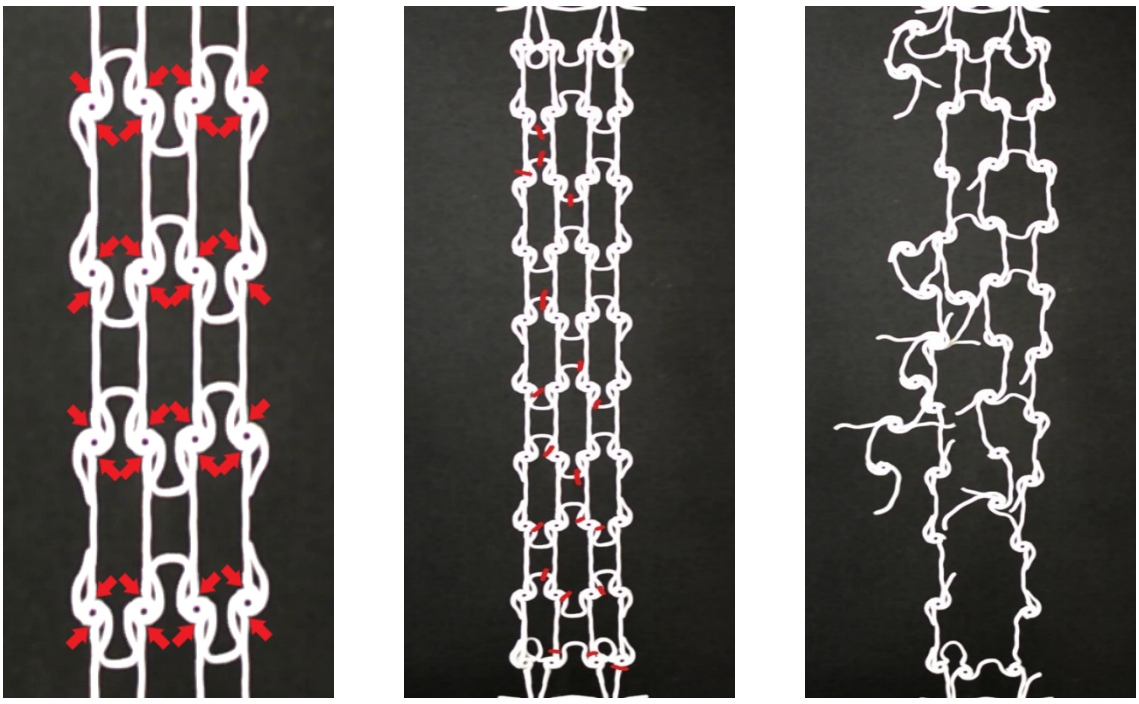

a b c

Figure 63: Mirrored-spiral parallel-axis closeup shows a) the links tearing from the nodes and are indicated with red arrows, b) where the scaffolding failed indicated with the red lines, c) scaffolding after the failure occurred.

Mirrored-spiral skew-axis tensile test

The next specimen is the offset angle or skew-axis of the mirrored-spiral scaffolding, and the progression of the tensile test can be seen in Figure 64. The skew-axis of the mirrored-spiral showed no auxetic behaviour even though the scaffolding was auxetic in the parallel-axis. The specimen contracted to about a quarter of its initial width while elongating, as seen in Figure 64e. The outer arms were observed to estimate the amount of rotation that the nodes performed during elongation and was found to be almost 180° before failure occurred.

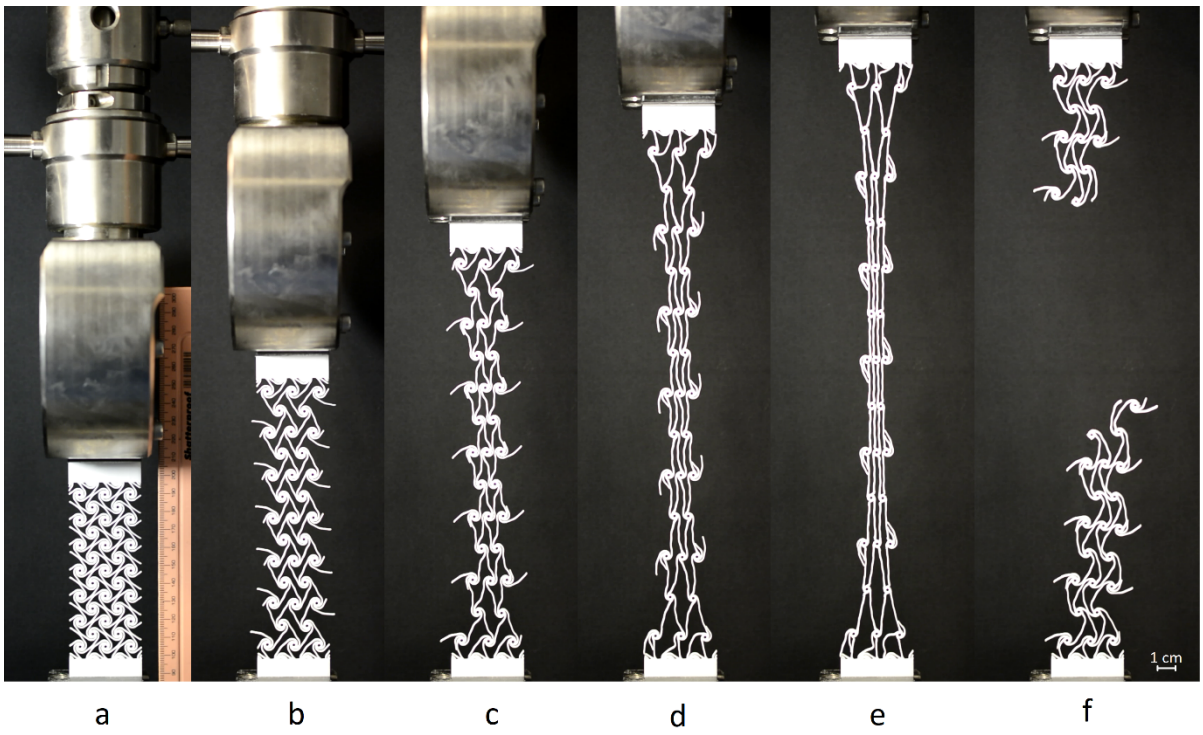

Figure 64: Different stages of deformation of the mirrored-spiral skew-axis sample during tensile testing: a) sample clamped in the grips in a natural position, b–d) scaffolding elongation, e) scaffolding moments before failure, f) scaffolding after the failure occurred.

Figure 65 shows the deformation of the mirrored-spiral skew-axis single pattern during the tensile test. The images show the single pattern starting as a 45° angled square and elongating vertically while collapsing horizontally inwards. No horizontal expansion was found at any point during the tensile testing, and the scaffolding completely collapsed in this direction to a point where the two vertical centre nodes were touching.

A closeup of Figure 64e in Figure 66a shows how the links have deformed before breaking. The links can be seen fully stretched out and is most likely the cause of the tearing due to the scaffolding not being able to deform any other way. Figure 66b shows the failure points of the specimen before failure occurred (in red). The close-up image of the specimen before failure also shows how much the scaffolding shrank in width before failing. Figure 66c is a close-up view of the failure point of the specimen after failure had occurred.

a b c d e

Figure 65: Mirrored-spiral skew-axis single pattern deformation (red lines connect the nodes of the single pattern and indicate the deformation of the single pattern): a) single pattern in its natural state, b–d) single pattern deforming as the scaffolding elongates, e) single pattern moments before the failure occurred.

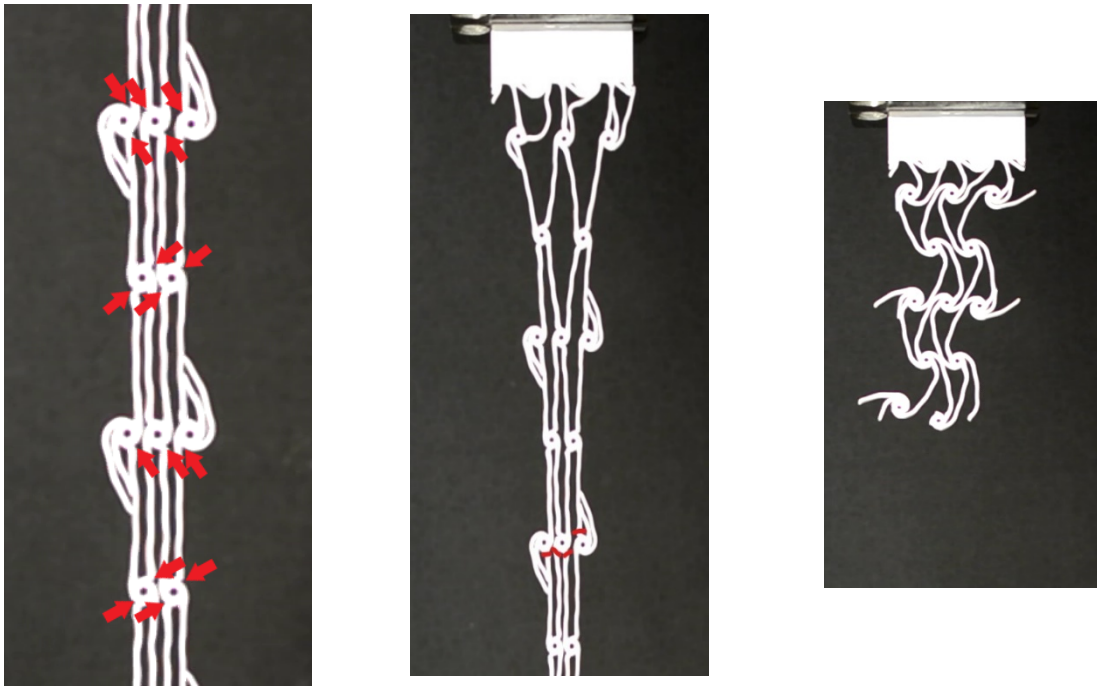

a b c

Figure 66: Mirrored-spiral skew-axis closeup shows a) the links tearing from the nodes and are indicated with red arrows, b) where the scaffolding failed indicated with red lines, c) the scaffolding after the failure occurred.

Comparison of tensile behaviour of mirrored-spiral samples

The graph below in Figure 67 shows the parallel- and the skew-axis data for the mirrored-spiral scaffoldings combined. The parallel-axis of the scaffolding, which showed auxetic behaviour, could withstand a significantly higher amount of force before breaking, reaching 97.8 N compared to the 59.4 N of the skew-axis. However, the skew-axis, which did not show any auxetic behaviour, could elongate further than the parallel-axis before breaking, reaching a total of 233.5 mm compared to 174.6 mm of the parallel-axis specimen. The data also shows that the parallel-axis had an elongation of 156% and the skew-axis had an elongation of 208% before breaking. It is noted that the two curves differ significantly in shape and length. The skew-axis has a smooth growth curve, compared to the parallel-axis, which has a much steeper and more turbulent curve.

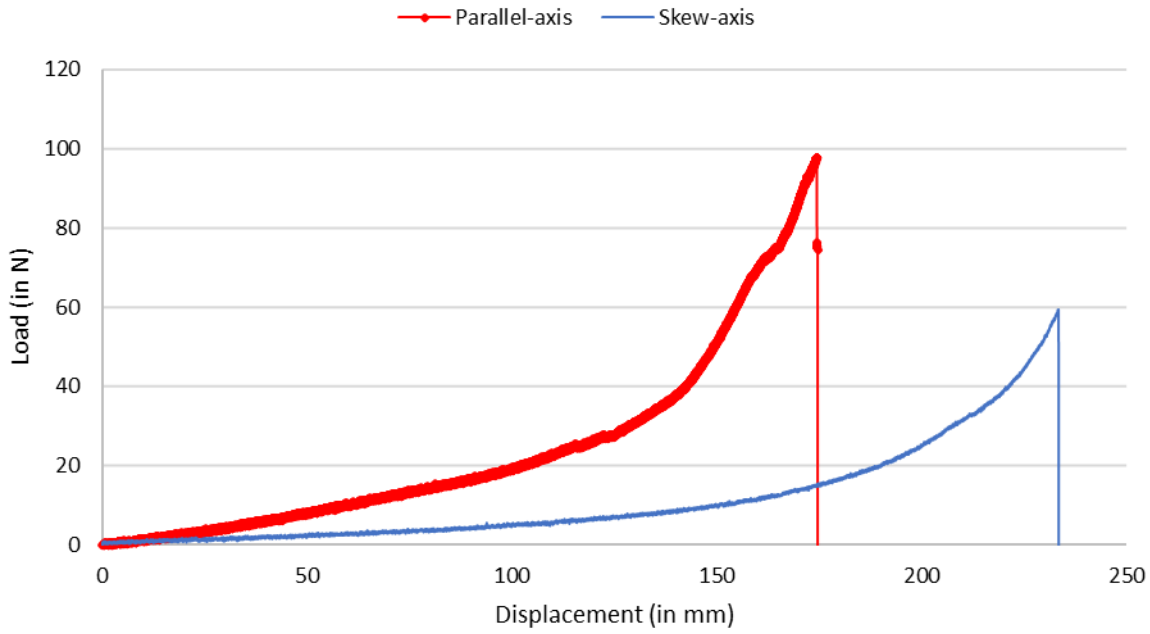

Figure 67: Load-displacement curves of mirrored-spiral samples.

4.2.6. Tensile testing of repeating-spiral samples

Repeating-spiral parallel-axis samples

The second scaffolding in the square category is the repeating-spiral, and the tensile test for the parallel-axis can be seen in Figure 68. It can be observed how the specimen twists as the elongation begins, seemingly twisting in the direction of the node's rotation. In Figure 68c, the twist is the most apparent. An observation can also be made on the layout of the nodes which is causing the twisting. The nodes further away from the ends seem to be aligned at an angle compared to the initial horizontal alignment. In Figure 68c, the deformation of the scaffolding

is seen to be inconsistent across the specimen. The top left part of the specimen appears to have more deformation than the top left side. The deformation then continues diagonally down to the bottom right side of the specimen, with the bottom left side having less deformation. The deformation of the specimen drastically changes in Figure 68d, with the twisting starting to even out and the different deformations also starting to equalize. In Figure 68d, the nodes can be seen starting to deform to the outer sides of the specimen, with gaps starting to form in the centre. By the stage shown in Figure 68e, the gaps are very apparent before failure occurs. It is also apparent how the links between the centre nodes progressed from diagonally up (from left to right) to diagonally down, which is quite a significant change.

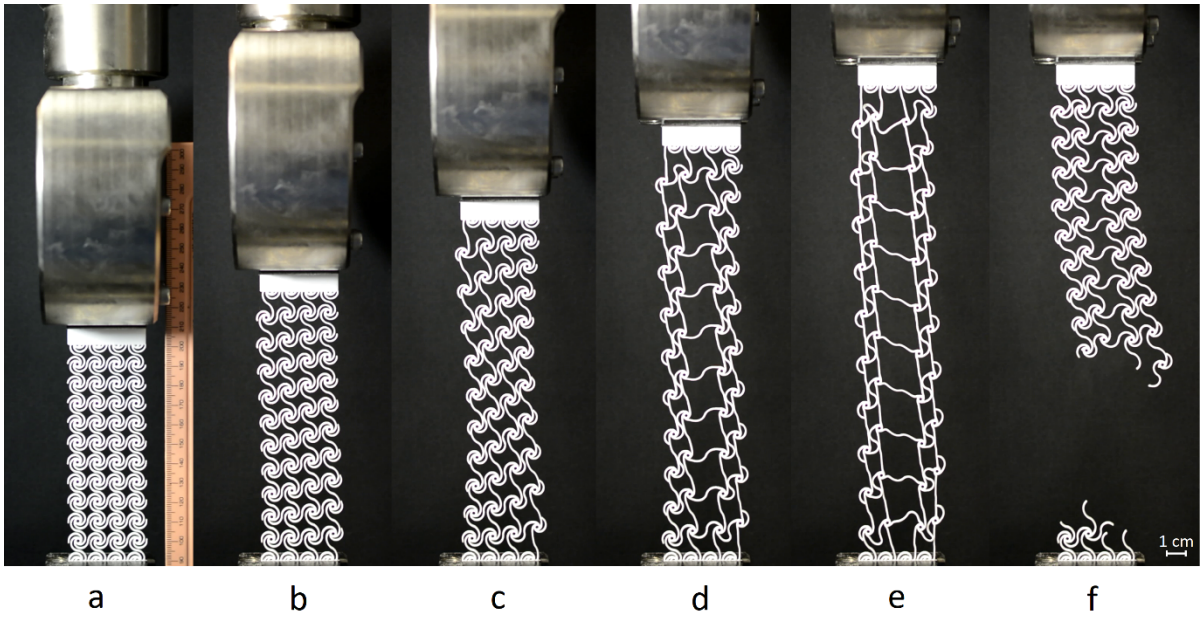

Figure 68: Different stages of deformations of the repeating-spiral parallel-axis sample during tensile testing: a) sample clamped in the grips in a natural position, b–d) scaffolding elongation, e) scaffolding moments before failure, f) scaffolding after the failure occurred.

Figure 69 shows the deformation of the repeating-spiral parallel-axis single pattern during the tensile test. The twisting effect is also apparent in the single pattern closeups, where it can be seen starting as a square that deforms into a parallelogram. This deformation continues to increase until Figure 69e, where the direction of the twist abruptly changes, as seen in Figure 69.

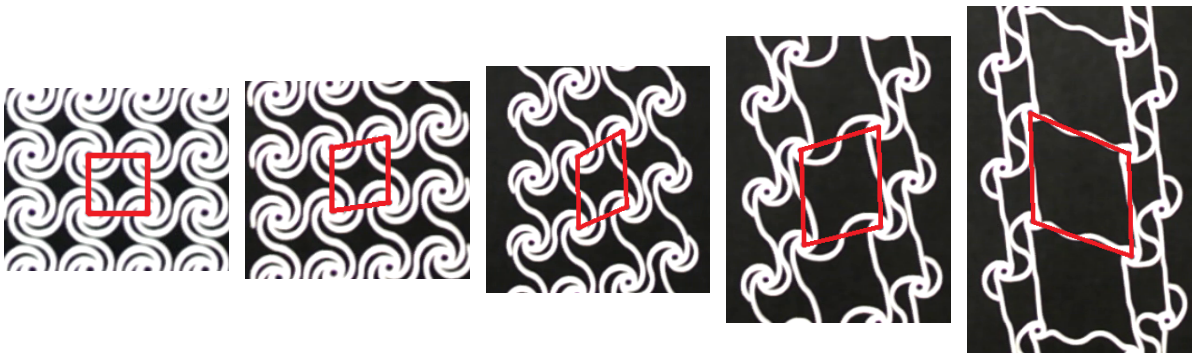

a b c d e

Figure 69: Repeating-spiral parallel-axis single pattern deformation (red lines connect the nodes of the single pattern and indicate the deformation of the single pattern): a) single pattern in its natural state, b–d) single pattern deforming as the scaffolding elongates, e) single pattern moments before failure occurred.

A close-up view of Figure 68e in Figure 70a shows how the links have deformed before breaking. No noticeable tearing was found in the closeup; however, there is some irregular deformation, compared to the rest of the specimen, at the ends of the scaffolding, as seen in Figure 70b. This is also where the failure occurred. Figure 70b shows the failure points of the specimen before failure occurred, and Figure 70c shows the failure points after failure had occurred.

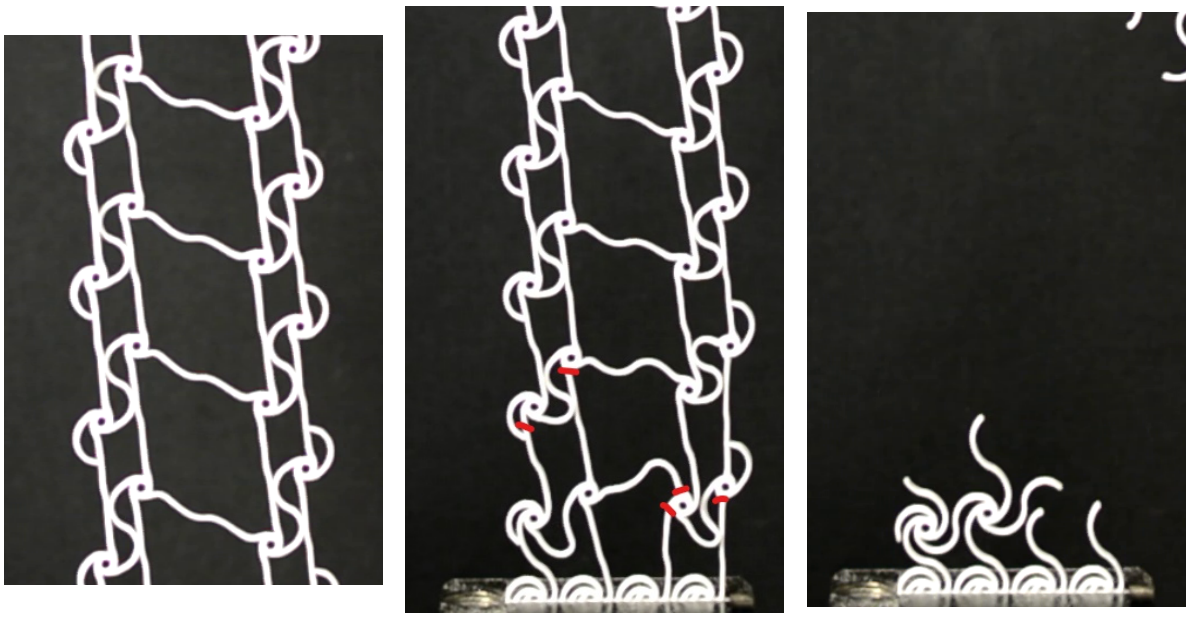

a b c

Figure 70: Repeating-spiral parallel-axis closeup shows a) the scaffolding under load but with no visible tearing, b) where the scaffolding failed indicated with red lines, c) scaffolding after the failure occurred.

Repeating-spiral skew-axis samples

The tensile test progression of the repeating-spiral skew-axis scaffolding is shown in Figure 71. The twisting is still apparent in this axis; the nodes are aligned at a 45° angle but continue to increase the angle in the node rotation direction. The deformation is inconsistent across the specimen. However, the deformation seems to be concentrated at the top right and bottom left of the specimen in this the skew-axis. The specimen can be seen completely collapsing inwards in the skew-axis, dissimilar to the parallel-axis, which developed gaps in the centre pushing the scaffolding outwards.

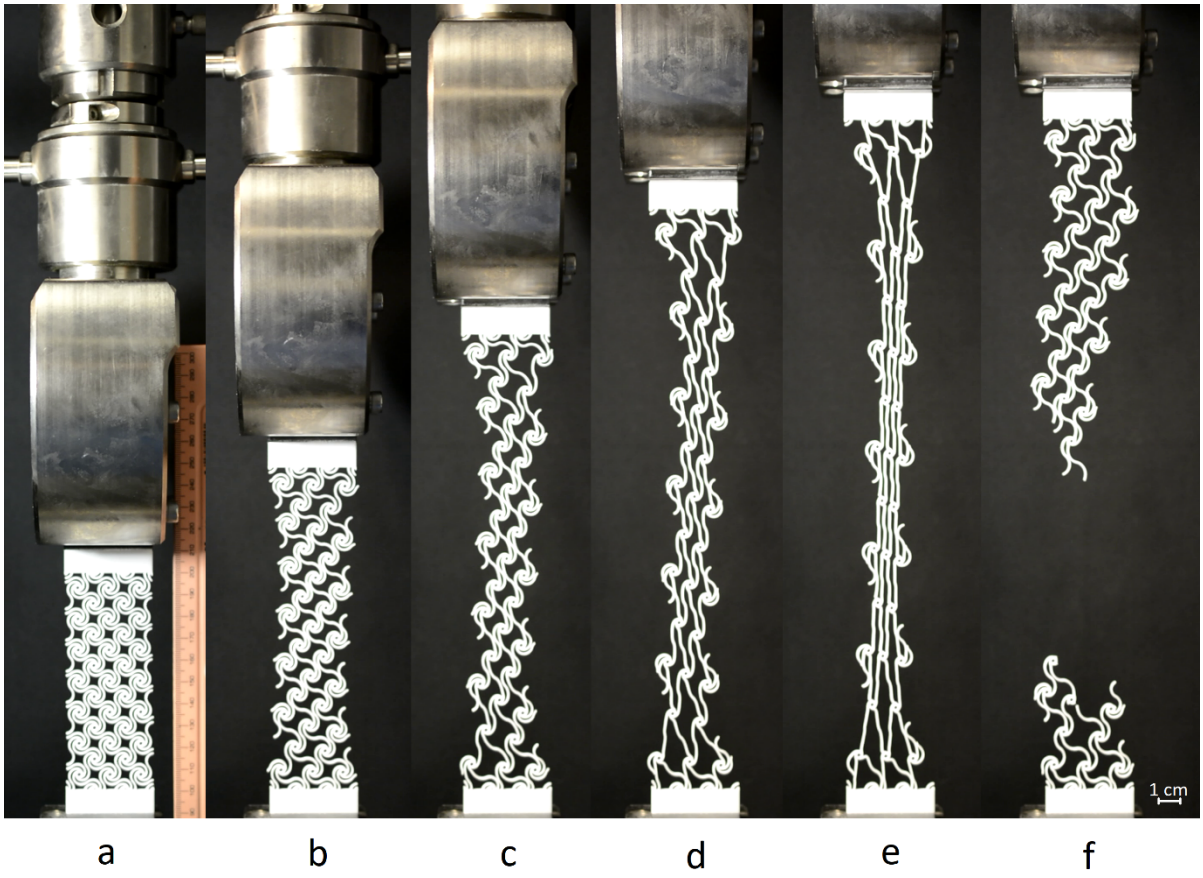

Figure 71: Different stages of deformations of the repeating-spiral skew-axis sample during tensile testing: a) sample clamped in the grips in a natural position, b–d) scaffolding elongation, e) scaffolding moments before failure, f) scaffolding after the failure occurred.

Figure 72 shows the deformation of the repeating-spiral skew-axis single pattern during the tensile test. The single pattern shows that the pattern deforms from an angled square into a parallelogram similar to the parallel-axis. However, the deformation does become more significant than in the parallel-axis, and in Figure 72e the shape almost becomes a diamond shape as the pattern collapses into the centre.

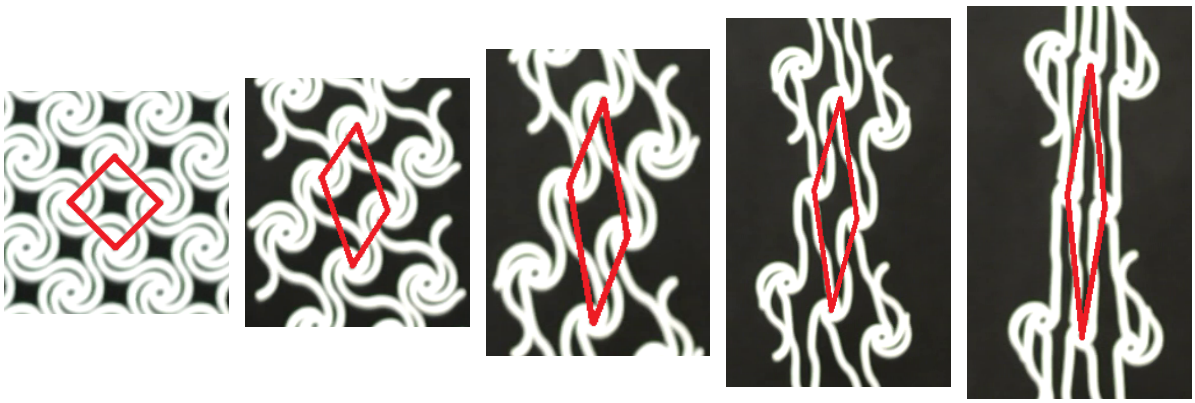

a b c d e

Figure 72: Repeating-spiral skew-axis single pattern deformation (red lines connect the nodes of the single pattern and indicate the deformation of the single pattern): a) single pattern in its natural state, b–d) single pattern deforming as the scaffolding elongates, e) single pattern moments before the failure occurred.

A closeup of Figure 71e in Figure 73a shows how the links have deformed before breaking. Unlike in the parallel-axis, the more apparent tearing can be seen in the skew-axis specimen. The tearing is most likely caused by the links being fully extended, allowing for no other deformation except tearing. Figure 73b shows the failure points of the specimen before failure occurred, and Figure 73c shows the failure points after failure had occurred.

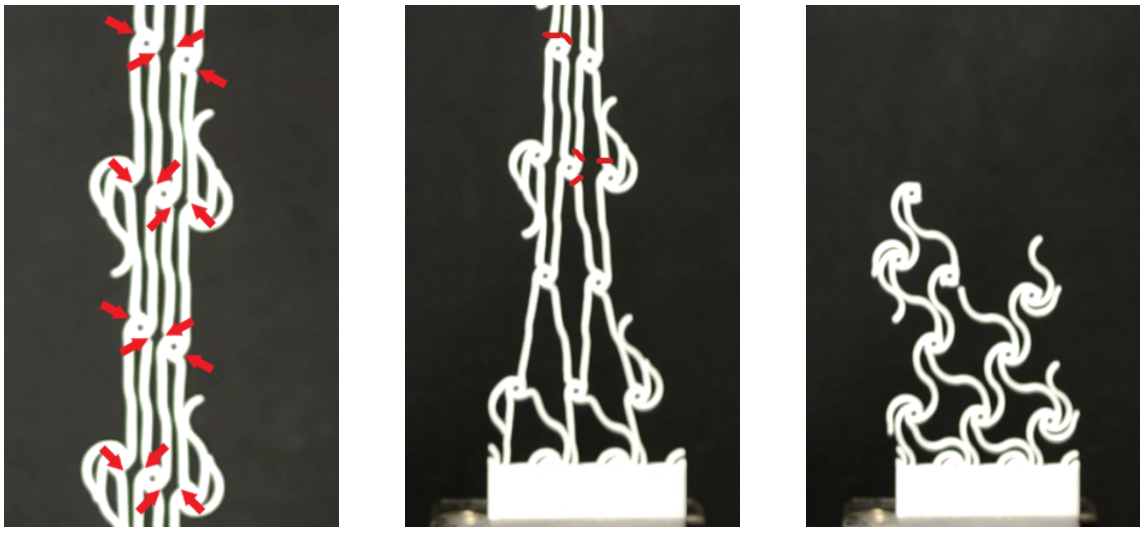

a b c

Figure 73: Repeating-spiral skew-axis closeup shows a) the links tearing from the nodes and are indicated with red arrows, b) where the scaffolding failed is indicated with red lines, c) scaffolding after the failure occurred.

Comparison of tensile behaviour of repeating-spiral samples

The data also shows that the parallel-axis has an elongation of 119.1%, and the skew-axis 189.4% before breaking. The graph below (Figure 74) indicates that both curves are growth curves, with the parallel-axis curve shorter and steeper with a linear section between 70–110 mm. The skew-axis curve is much smoother and grows much more consistently and longer. The two curves reach almost the same point of peak force before breaking.

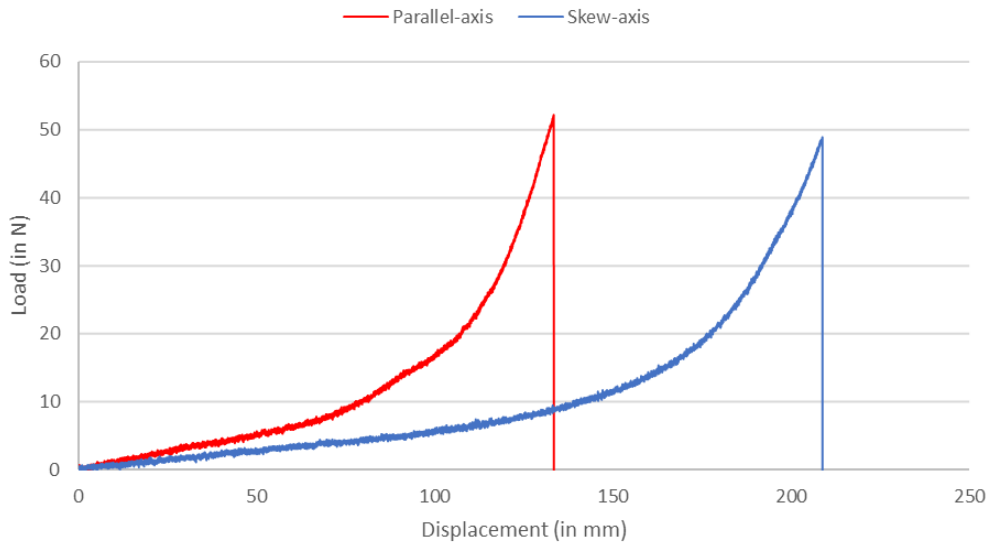

Figure 74: Load-displacement curves of repeating-spiral samples.

4.2.7. Tensile testing of linked-spiral samples

Linked-spiral parallel axis samples

The last of the square category scaffoldings is the linked-spiral; the parallel-axis tensile test is shown in Figure 75. This scaffolding also exhibits auxetic behaviour. The specimen expands horizontally while elongating vertically. The specimen increases in width up and until the stage shown in Figure 75d, the width then decreases. Figure 75e shows the moment before failure occurs; the width of the specimen is still greater than the initial width of the scaffolding.

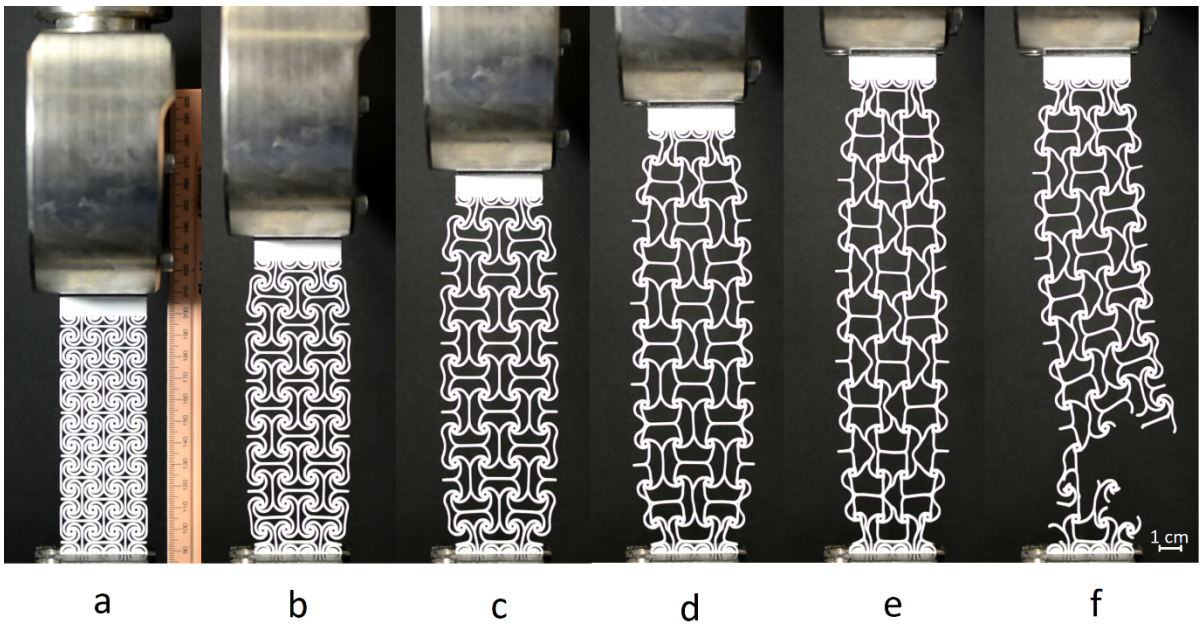

Figure 75: Different stages of deformations of the linked-spiral parallel-axis sample during tensile testing: a) sample clamped in the grips in a natural position, b–d) scaffolding elongation, e) scaffolding moments before failure, f) scaffolding after the failure occurred.

Figure 76 shows the deformation of the linked-spiral parallel-axis single pattern during the tensile test. The pattern remained square-shaped for about half of the elongation; it only increased in size. In Figure 76d, the shape of the pattern can be seen elongating in height more than expanding in width. In Figure 76e, moments before failure occurred, the pattern has grown more in height but reduced in width. The nodes also rotated towards the pattern's centre, causing the pattern to expand in all directions when elongating. The nodes rotated about 90° before failing.

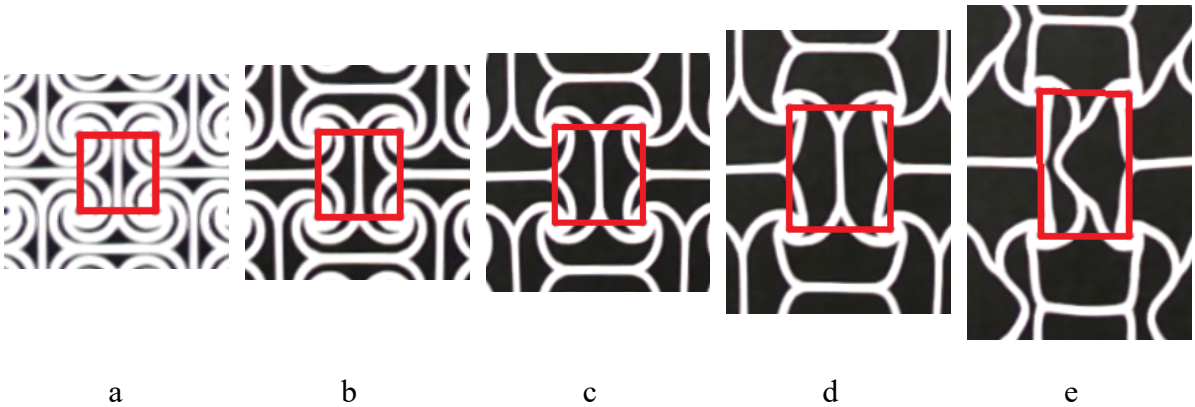

Figure 76: Linked-spiral parallel-axis single pattern deformation (red lines connect the nodes of the single pattern and indicate the deformation of the single pattern): a) single pattern in its natural state, b–d) single pattern deforming as the scaffolding elongates, e) single pattern moments before the failure occurred.

A closeup of Figure 75e in Figure 77a shows how the links have deformed before breaking. No noticeable tearing was found in the closeup. Furthermore, it does seem that a significant amount of stress could be concentrated at the link connection where the arms of two nodes meet to form the merged support link. However, observing the failure point in Figure 77b before failure occurred, it is noted that there are no failure points at the merger point. There are failure points close to the merger point, and the majority of the failure points are at the ends of links, similar to most of the failure points in the other specimens.

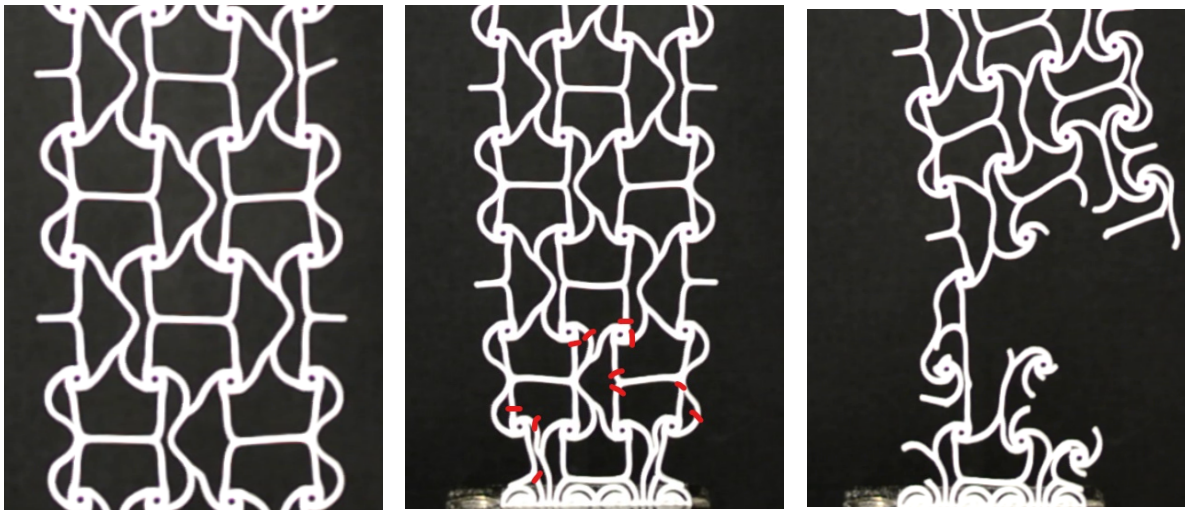

a b c

Figure 77: Linked-spiral parallel-axis closeup shows a) the scaffolding under load but with no visible tearing, b) where the scaffolding failed indicated with red lines, c) scaffolding after the failure occurred.

Linked-spiral skew-axis tests

The last of the scaffolding specimens tested is the linked-spiral skew-axis, and the tensile test is shown in Figure 78. Some auxetic behaviour can be seen as the specimen increases in width with the elongation in height. Even though the expansion in width is minor compared to the parallel-axis, it is still noticeable. This specimen also expands in width to around Figure 78e, where it then starts to contract. When the specimen fails, the width is still greater than its initial width. The shape of the deformation of the scaffolding is a sort of zig-zag shape, with some of the links transferring the tensile force and others supporting the scaffolding from collapsing in on itself.

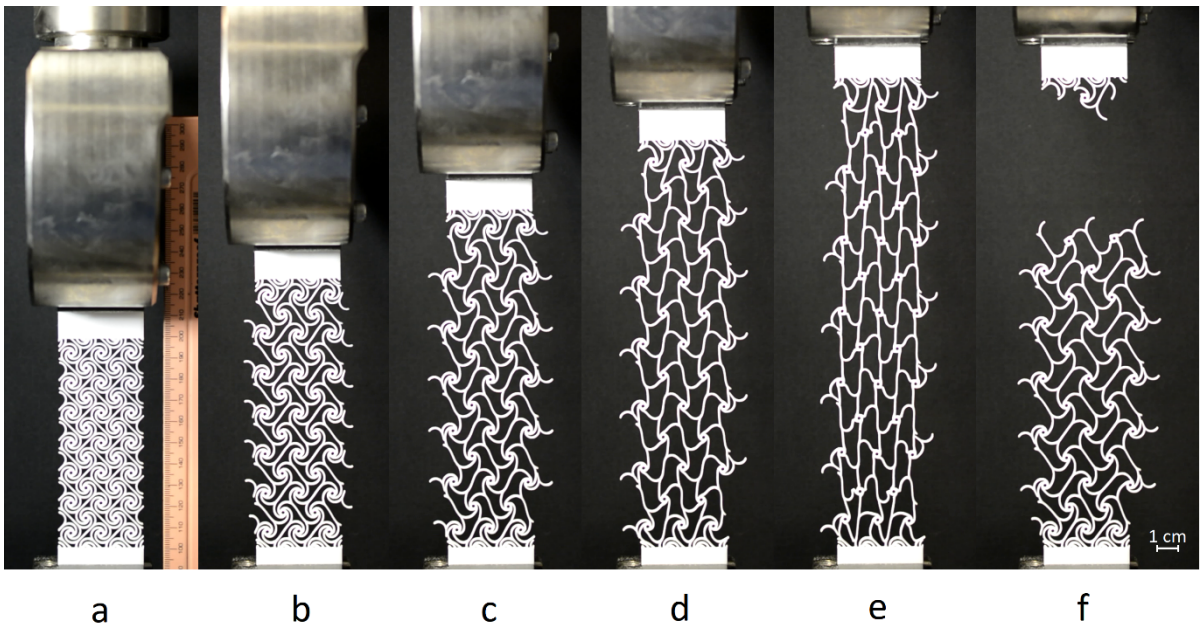

Figure 78: Different stages of deformations of the linked-spiral skew-axis sample during tensile testing: a) sample clamped in the grips, b–d) scaffolding elongation, e) scaffolding moments before failure, f) scaffolding after the failure occurred.

Figure 79 shows the deformation of the linked-spiral skew-axis single pattern throughout the tensile test. The shape of the single pattern goes from an angled square at the start of the test and deforms vertically as the specimen is elongated. The entire pattern also expands as the specimen elongates. Having a look at the merged link of this scaffolding, the arms connected to the top and bottom node appear to have almost pulled the merged link straight into a vertical position while pulling the left and right node arms closer and creating the zig-zag effect.

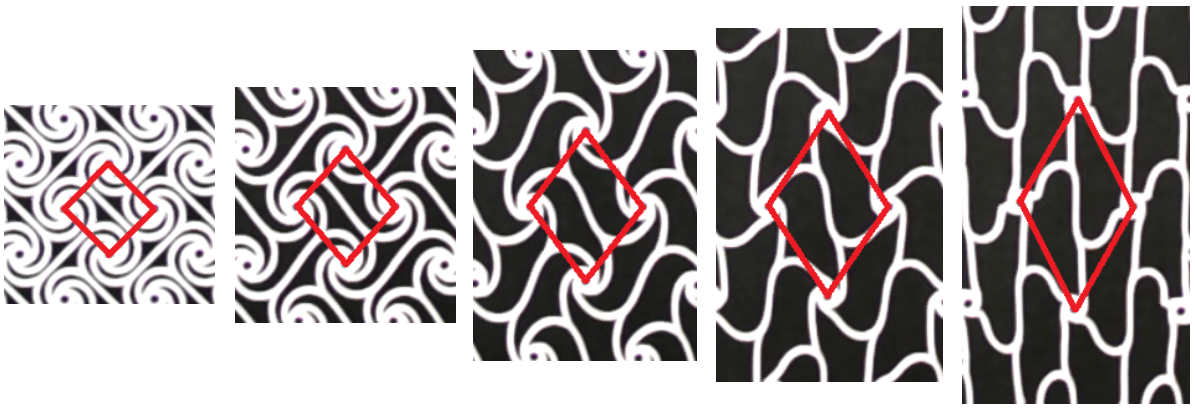

Figure 79: Linked-spiral skew-axis single pattern deformation (red lines connect the nodes of the single pattern and indicate the deformation of the single pattern): a) single pattern in non-loaded state, b–d) single pattern deforming as the scaffolding elongates, e) single pattern moments before the failure occurred.

A close-up view of Figure 78e in Figure 80 shows how the links have deformed before breaking. Unlike in the parallel-axis, the more apparent tearing can be seen in the closeup of the skew-axis specimen in Figure 80a. Most tears are located at the ends of the links connecting to the nodes, specifically those that support the scaffolding from collapsing. This tearing is most likely due to the tensile force pulling the scaffolding inwards, causing the supporting arms to deform past the point that the material can bend. Figure 80b shows the failure points of the specimen before failure occurred, and Figure 80c shows the failure points after failure had occurred.

a b c

Figure 80: Linked-spiral skew-axis closeup shows a) the scaffolding under load but with no visible tearing, b) where the scaffolding failed indicated with red lines, c) scaffolding after the failure occurred.

Comparison of tensile behaviour of linked-spiral samples

The graph below in Figure 81 shows parallel- and skew-axis load-displacement curves for linked-spiral scaffoldings. The skew-axis of the scaffolding withstood a greater amount of force before breaking, reaching 96.8 N compared to the 65.1 N of the parallel-axis. The skew-axis was also able to elongate further than the parallel-axis before breaking, reaching a total of 123.3 mm compared to 109.7 mm of the parallel-axis specimen. The data also shows that the parallel-axis had an elongation of 97.9%, while the skew-axis had 110% before breaking. The parallel-axis curve had a more linear growth, and the skew-axis had a smoother growth curve that initially grew slower and then started growing exponentially.

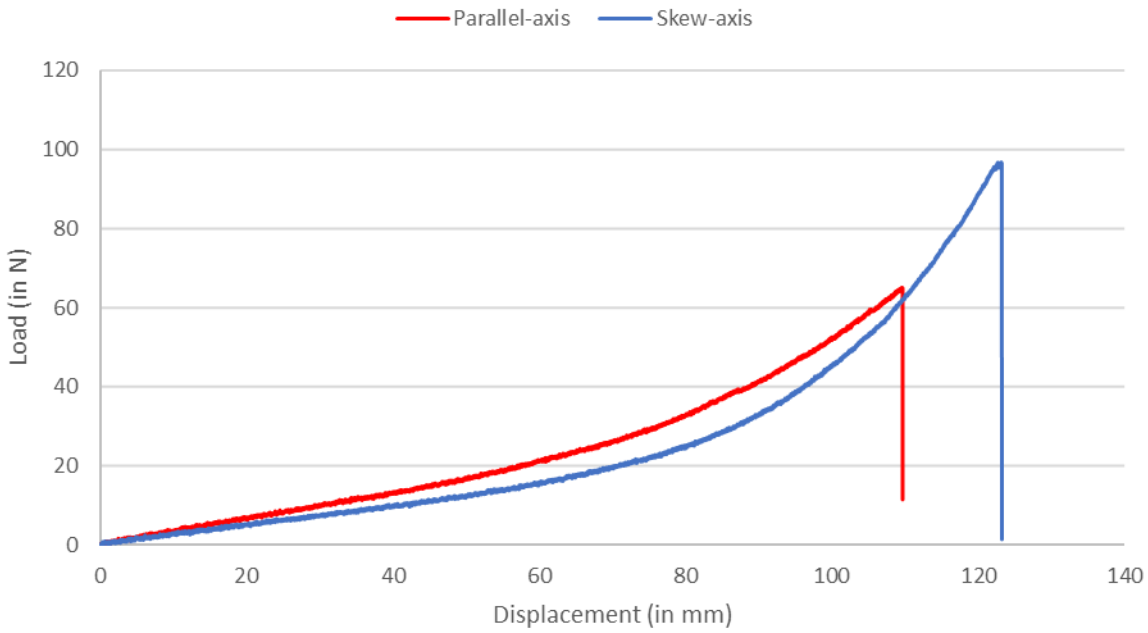

Figure 81: Load-displacement curves of linked-spiral samples.

4.2.8. Tensile testing of solid benchmark samples

Finally, a benchmark specimen was tested with a solid structure of the same thickness as the scaffoldings. The load-displacement graph is shown in Figure 82. The benchmark specimen reached a peak force before failing at 4919 N, which is 44.5 times more than the highest peak force measured for any scaffolding specimens (the double-bow X-axis with 110.6 N). However, the benchmark specimen only displaced 36.45 mm before failing, which is an elongation of 32,6% compared to 245.6%, the highest elongation of any scaffoldings (the wide-bow Y-axis, which displaced 275 mm before failing).

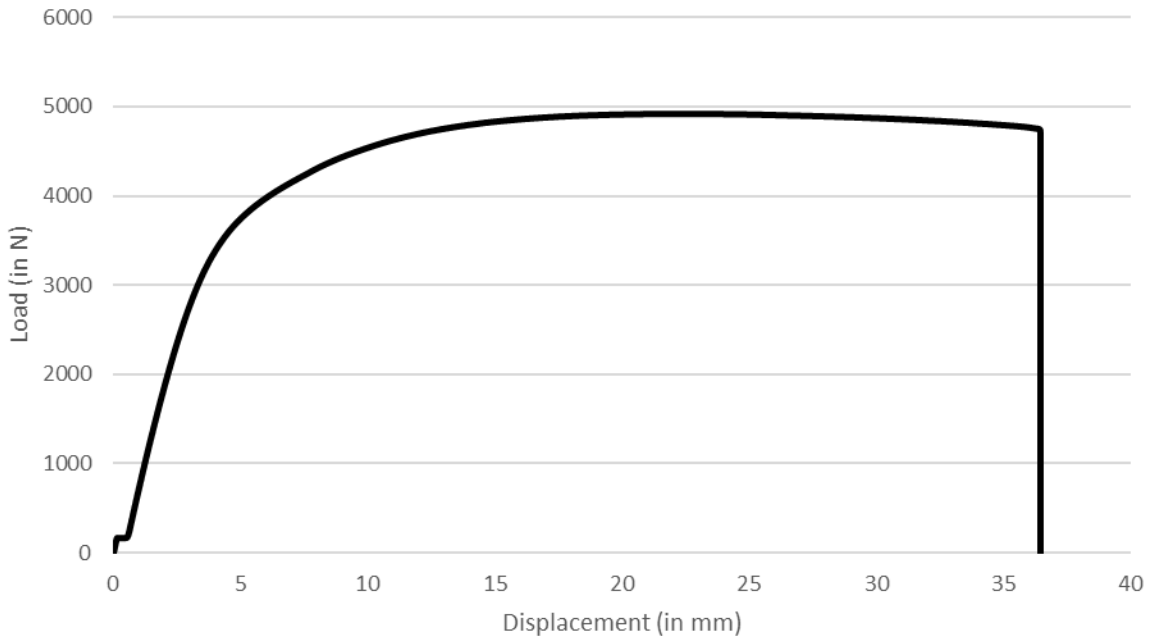

Figure 82: Load-displacement curves of benchmark solid PA 2200 specimen.

4.2.9. Polymer tensile test data collected

Figure 83 shows the load versus displacement for all the specimens (excluding the solid specimen). A trend can be seen in the correlation between the peak load and the maximum displacement. Specimens with less displacement tend to have higher peak loads, and specimens with higher displacements have lower peak loads. Further observation shows that the two directions behave relatively similar for most scaffoldings and end in the same area, except for the mirrored-spiral and the repeating-spiral.

Table 9 shows the most important data points collected from the polymer tests. From the data collected, it can be observed that scaffoldings with an axis not in line with the intended stress path (Y-axis or skew-axis samples) were able to elongate further than the in-line axis samples (X-axis and parallel-axis). There is a correlation between the number of links per node, the length of the links and the maximum load and displacement at the break. Scaffoldings with fewer links per node could elongate further and had a lower maximum load (Table 9 and Table 10). Similarly, a scaffolding with longer links could also elongate further with a lower maximum load. This observation concludes that there is a direct relationship between the number of links per node and the length of each scaffolding link. Table 10 further proves this

with the correlation coefficients. Similar results were also found in other studies (Kolken & Zadpoor, 2017; Yang et al., 2012; Overvelde et al., 2012).

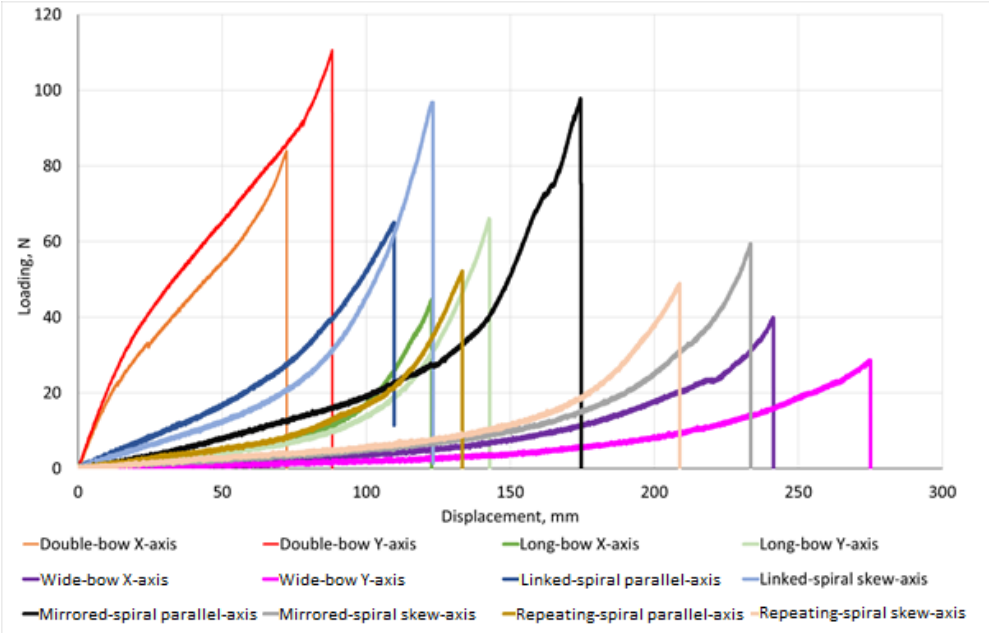

Figure 83: Loading-displacement curves of all tested L-PBF polymer samples.

Table 9: Data collected from polymer PA 2200 tensile specimens

Sample	Number of links per node	Length of the link, mm	Maximum loading, N	Displacement at the break, mm	Deformation behaviour
Wide-bow X-axis	3	18.5	40	241.4	Non-auxetic
Wide-bow Y-axis	3	18.5	28.7	275	Slightly auxetic
Double-bow X-axis	6	9.8	84.02	72.4	Non-auxetic
Double-bow Y-axis	6	9.8	110.58	88.2	Non-auxetic
Long-bow X-axis	3	12.1	44.7	122.7	Non-auxetic
Long-bow Y-axis	3	12.1	66.1	142.9	Slightly auxetic
Mirrored-spiral parallel-axis	4	21.1	97.8	174.6	Auxetic
Mirrored-spiral skew-axis	4	21.1	59.4	233.5	Non-auxetic
Repeating-spiral parallel-axis	4	20.5	52.2	133.4	Slightly auxetic
Repeating -spiral skew-axis	4	20.5	48.9	208.8	Non-auxetic
Linked-spiral Parallel-axis	4	28.7	65.1	109.7	Fully auxetic
Linked -spiral skew-axis	4	28.7	96.8	123.3	Slightly auxetic
Benchmark/Solid	-	-	4918.6	36.5	Non-auxetic

Table 10: Correlation coefficients between design features and tensile properties

	Number of links per node	Length of the link	Maximum loading	Displacement at break
Number of links per node	1	-0.295	0.677	-0.614
Length of the link		1	-0.057	0.240
Maximum loading			1	-0.597
Displacement at break				1

4.2.10. Summary

From this study, several conclusions can be drawn:

- The wide-bow scaffolding had the longest links with the least number of links per node and had the longest elongation with the lowest maximum load, making this the most compliant of the scaffoldings.
- The double-bow was the strongest scaffolding, with the highest load and the least elongation. Even though it could withstand the highest load, the double-bow is too strong and will most likely cause bone resorption on the mounting point if implemented as a cranial implant.
- The long-bow was stronger than the wide-bow but weaker than the double-bow and elongated more than the double-bow but less than the wide-bow. It also showed some signs of auxetic behaviour in the Y-axis.
- The mirrored-spiral showed high displacement and low load in the parallel-axis but low displacement and high load in the skew-axis, which is not ideal for a cranial implant as it needs to be somewhat isotropic. However, most scaffoldings showed similar deviations in the different axes. The mirrored-spiral had the largest deviation in load and the second largest in displacement.
- Unlike the other scaffoldings, the repeating-spiral had an asymmetrical structure, which resulted in the scaffolding displacing asymmetrically. The opposite ends of the scaffolding were displaced in different directions as if the scaffolding was rotating around its centre.

- The linked-spiral design was the only scaffolding that exhibited fully auxetic behaviour in the tensile testing by having a larger width than its initial width throughout the test. The linked-spiral also showed promise at being strong perpendicular to the plane of the scaffolding in the preliminary tests. This is most likely due to the merging between links making the scaffolding stronger. Finally, even though the linked-spiral had the longest link length of all the scaffoldings, it still exhibited good peak force before breaking and showed reasonable elongation.

CHAPTER 5: LASER POWDER BED FUSION TI6AL4V DYNAMICALLY RESPONSIVE SCAFFOLDINGS

5.1. FEA simulations of Ti6Al4V specimens

Two scaffoldings were selected to be printed from Ti6Al4V grade 23 alloy: wide-bow and linked-spiral. First, FEA studies were done for the wide-bow X-axis and the linked-spiral parallel-axis samples. The purpose of the FEA studies is to compare the simulation results with the actual results to determine if FEA can be used to predict the behaviour, stress levels and failure points of the scaffoldings.

For the setup of the simulations, minor changes were made to the models that will not affect the results of the FEA simulations. Firstly, the 20 mm clamping area was reduced to 2 mm. This reduces the simulation time as these parts of the specimens are only for clamping and will not affect the scaffoldings' behaviour. A 2D surface was made from the scaffolding profile, and the surface will then be defined as 2 mm in the simulation setup, see Figure 84a. This greatly reduces the simulation time without compromising the result as the scaffolding is only a 2 mm thick 2D structure. The specimens were all done with a 0.1 mm SMUS (Shell Mesh Using Surfaces)-type blended curvature-based mesh. Figure 84b shows a closeup of the meshed 2D scaffolding.

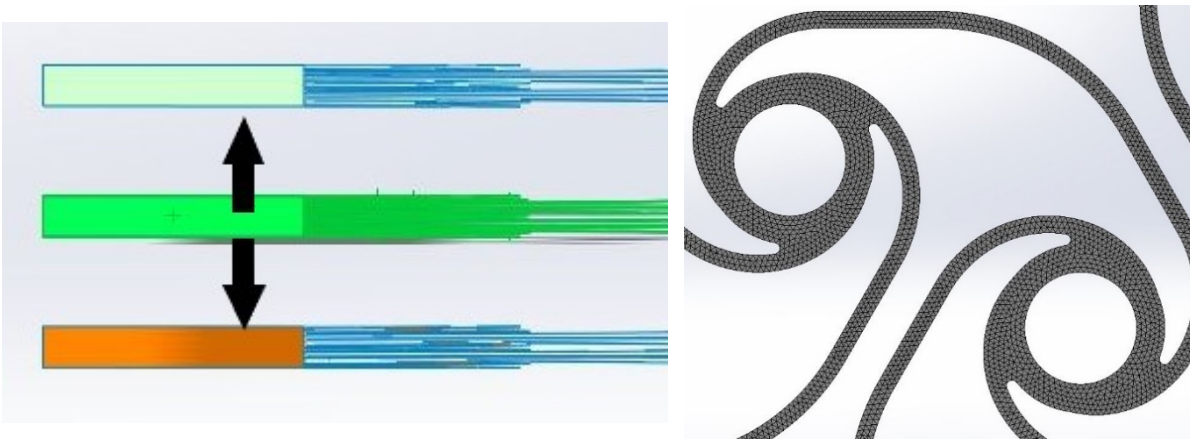

a b

Figure 84: Ti6Al4V simulation geometry setup: a) shows how the 2D surface was thickened, b) closeup of the scaffolding mesh.

Figure 85 shows the simulation setup and restraints, with the green arrows showing where the specimens are fixed, and the purple arrows indicate what surface the tensile force is applied to

and in what direction the force is moving. For Ti6Al4V simulations, a force of 1000 N was used for all the specimens. Table 4 in the methodology chapter shows the material properties used for the Ti6Al4V simulations, and the simulations were all done in large displacement mode.

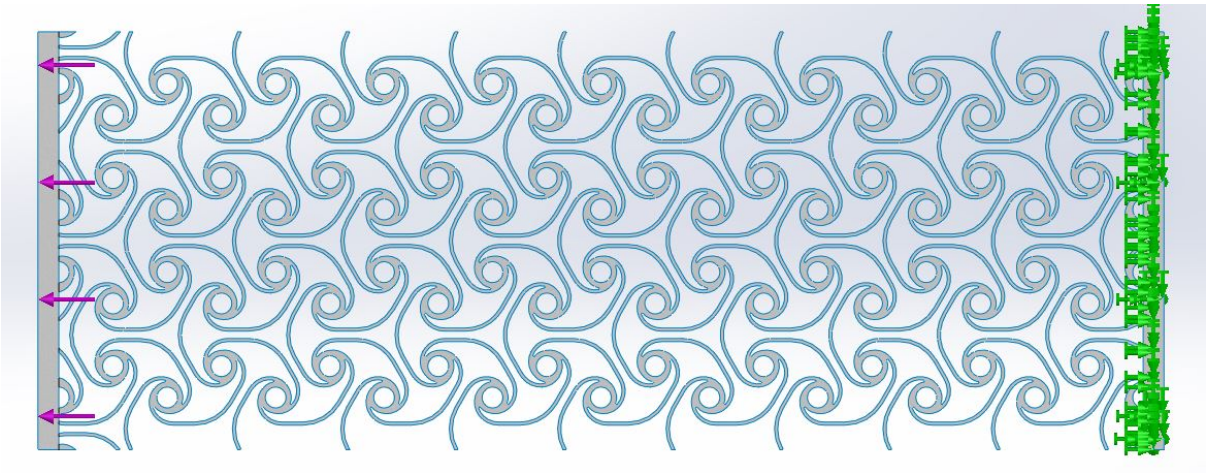

Figure 85: Ti6Al4V simulation setup.

5.1.1. Wide-bow X-axis Ti6Al4V sample

The stress distribution graph for the wide-bow X-axis is seen in Figure 86. Figure 86a shows the stress distribution diagram at the maximum stress observed, and Figure 86b shows the stress distribution diagram at the material yield point. From these images, it can be observed that in Figure 86a, most of the specimen is at a relatively low-stress level compared to the maximum stress experienced by the specimen. This is due to very high-stress concentration, which reached maximum stress of 19.67 GPa. Figure 86b shows a much more diverse diagram, where all the red sections are stress concentrations above the yield point of the material, which is 0.827 GPa.

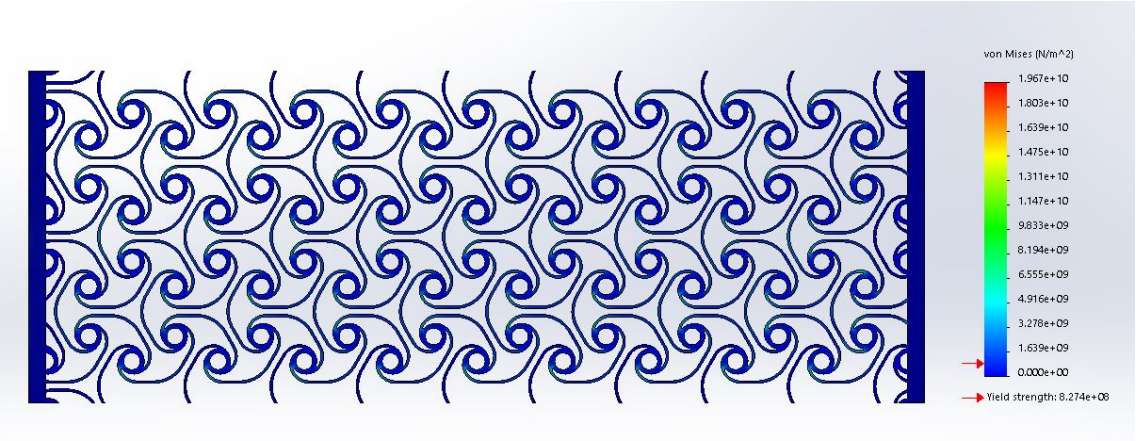

a

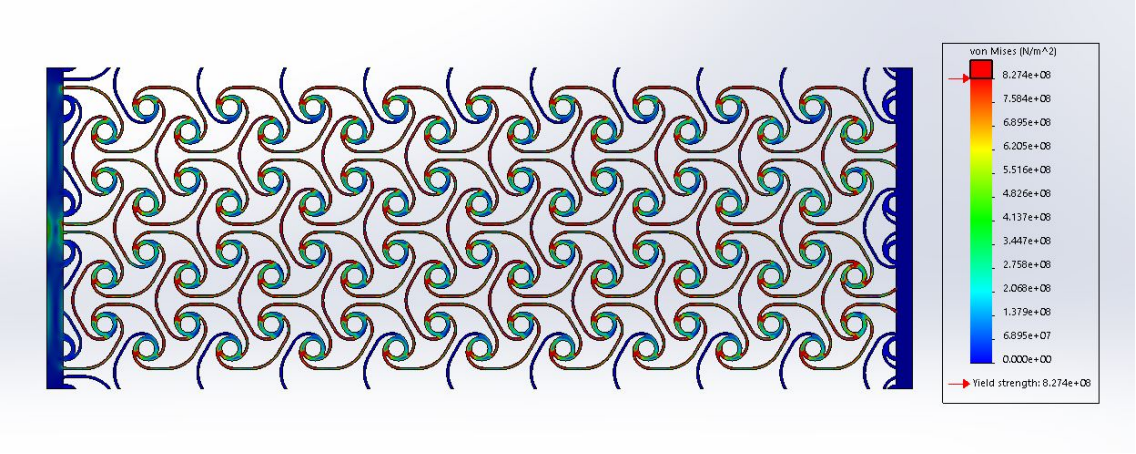

b

Figure 86: Wide-bow X-axis Ti6Al4V simulation stress distribution diagrams at 1 kN loading: a) stress distribution relative to the maximum stress observed, b) stress distribution relative to the material yield point.

On closer examination of the single patterns and nodes of the specimen in Figure 87, the stress concentrations can be seen. Figure 87a shows the stress diagram relative to maximum stress; the stress concentrations are directly at the start of the links before the link merges with the node. Focusing on a node in Figure 87c, the peak stress concentration point is found at the inner arc as the link merges with the node. Figure 87b and Figure 87d show the single pattern and node stress diagrams relative to the material's yield point; all the red-coloured sections are sections where the stress surpasses the yield point of the material and are likely points of failure. Furthermore, Figure 87b shows a pattern to the high-stress concentrations per node; each node has one link with a much higher stress concentration at the merger point. This pattern seems to repeat at each link that connects to an adjacent node in the elongation axis (the axis in which the specimen is pulled in). However, the stress concentration is only at one end of the link: the

end which would have the most searing force once the scaffolding is fully deformed (the point before the scaffolding fails). The deformation of the specimen can be seen in Figure 88.

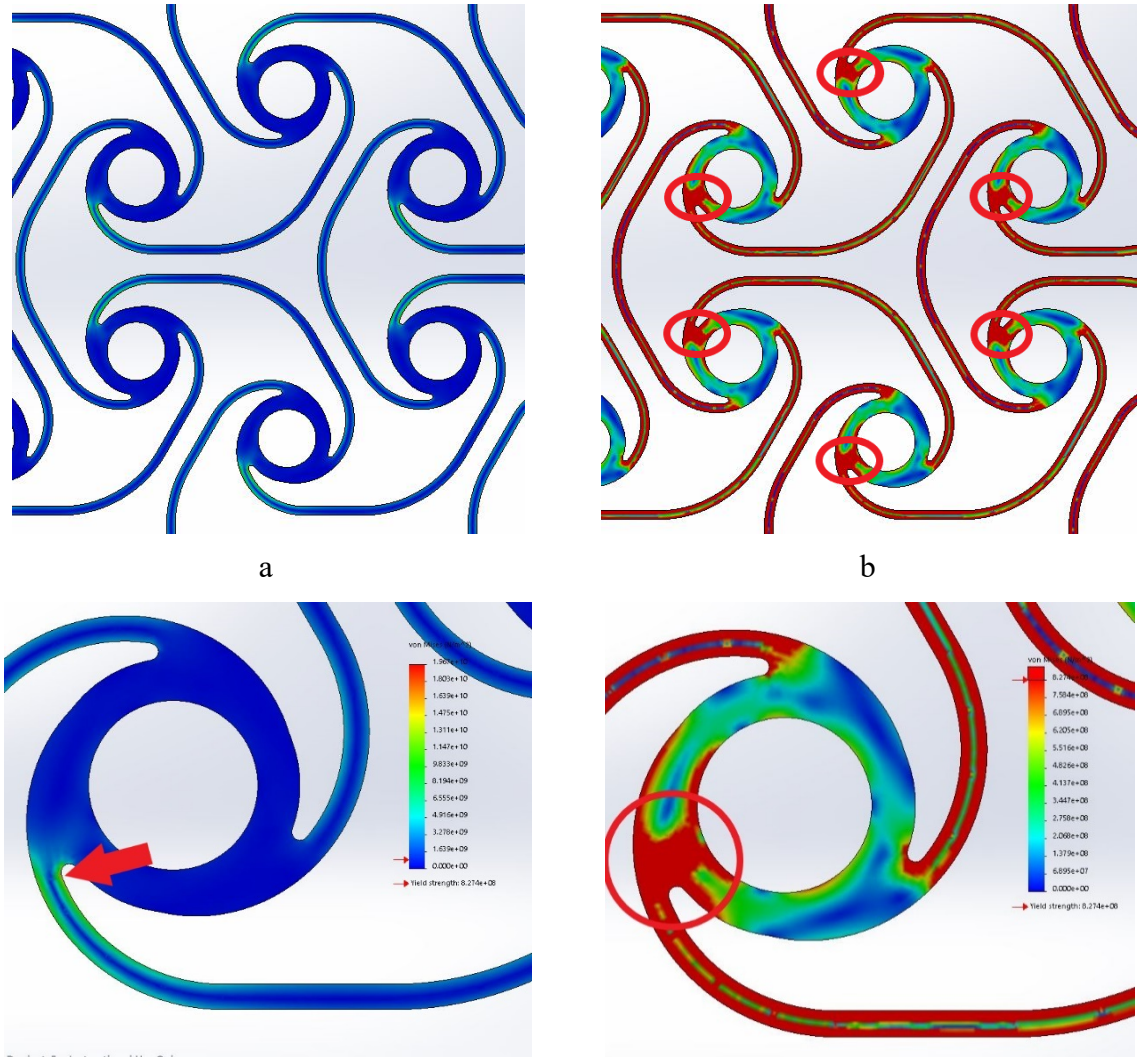

a b c d

Figure 87: Wide-bow X-axis Ti6Al4V simulations stress distribution diagram closeups (red circles show a general area where the stress concentrations on the scaffolding are high and the red arrow shows where the maximum stress on the scaffolding is located): a) single pattern relative to the maximum stress, b) single pattern relative to the yield point, c) a node relative to the maximum stress, d) a single node stress relative to the yield point.

Further simulation results of the deformation of the wide-bow X-axis specimen can be seen in Figure 88 below. Figure 88a shows the simulated deformation of the specimen, which reached a total elongation length of 190.2 mm. Auxetic behaviour can be observed from the simulation as the width of the specimen expanded as elongation continued. Figure 88b shows a closeup of a single pattern at the simulated deformation. Taking a closer look at a node in the initial state and the deformed state in Figure 88c and Figure 88d respectively, it can be seen how the node

is rotated and deformed to be able to elongate at such a high degree and how the behaviour of the scaffolding is auxetic.

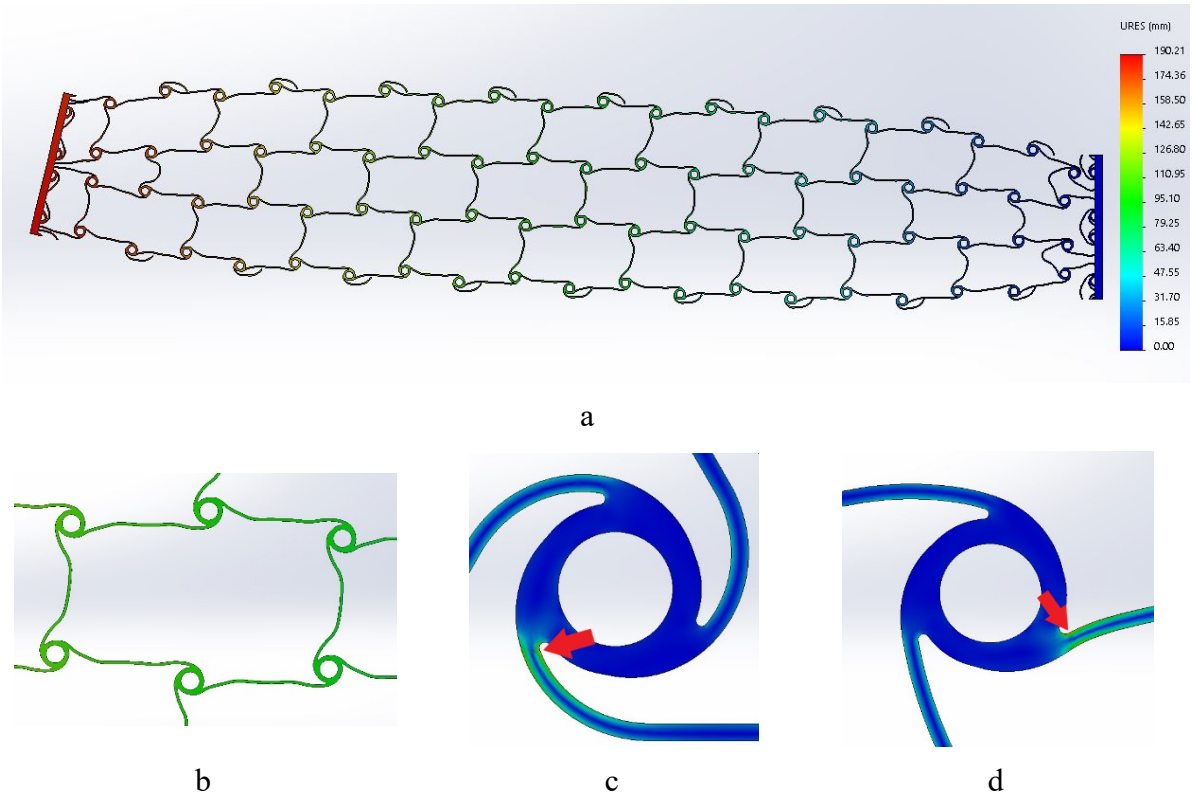

Figure 88: Wide-bow X-axis Ti6Al4V simulation deformation: a) the simulated deformation, b) closeup of a single pattern at the simulated deformation, c–d) rotation of a node with the red arrow indicating the same location.

The red arrow on both Figure 88c and Figure 88d shows the high-stress concentration point and represents the same location; this offers a good idea of the rotational deformation of the node. Therefore, it can be estimated that the node rotated about 90° from initial to final deformation. Figure 88d shows the stress diagram of a node when it is deformed and explains why only one of the links connected to the node has a high-stress concentration. This link has been pulled to deform further than the other two and is most likely experiencing shear forces as well as tensile forces.

5.1.2. Wide-bow Y-axis Ti6Al4V sample

Figure 89 shows the stress distribution graph for the wide-bow X-axis. Figure 89a and Figure 89b show the stress distribution at the maximum stress observed and the stress distribution at the material yield point. The maximum stress observed in the simulation was 21.37 GPa. Like the X-axis in the wide-bow design, the Y-axis has stress concentration points that are much

higher than the rest of the specimen (Figure 89 a). Figure 89b shows more detail of the distribution of the stresses. The red section shows stresses that exceed the material's yield point and are likely points of failure.

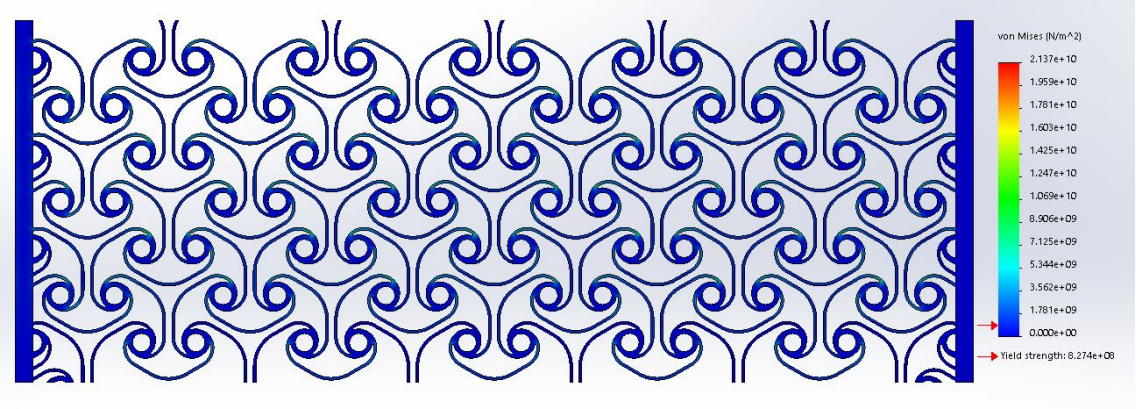

a

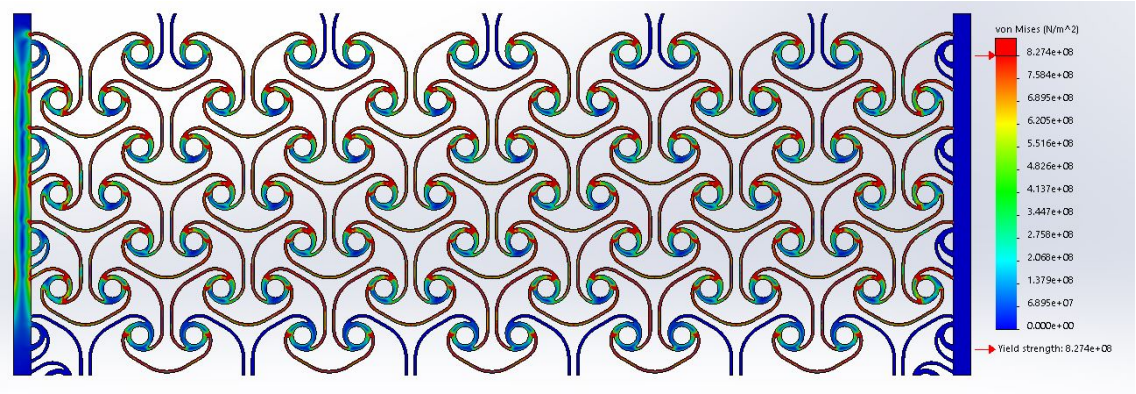

b

Figure 89: Wide-bow Y-axis Ti6Al4V simulation stress distribution diagrams at 1 kN loading: a) stress distribution relative to the maximum stress observed, b) stress distribution relative to the material yield point.

In Figure 90 , the stress distribution diagrams of a single pattern relative to the maximum stress and yield strength, respectively, can be seen. The single pattern stress diagrams show two high-stress concentrations per node. The link connecting nodes parallel to the elongation direction have relatively similar stress concentrations on both ends of the link and have the second largest concentration areas; these links are shown in Figure 90b at the number '1'. The link with the largest concentration area is shown in Figure 90b at the number '2'. This link has a high-stress concentration at one end of the link and a low-stress concentration at the other end. Furthermore, Figure 90c shows a closeup of a node with a red arrow indicating the highest stress concentration on the specimen. Figure 90d shows the stress distribution diagram relative to the material yield point on an individual node. This shows the stress concentration area of

the number ‘1’ link at the left red arrow and the high- and low-stress concentration areas for the number ‘2’ link at the top red and blue arrows, respectively.

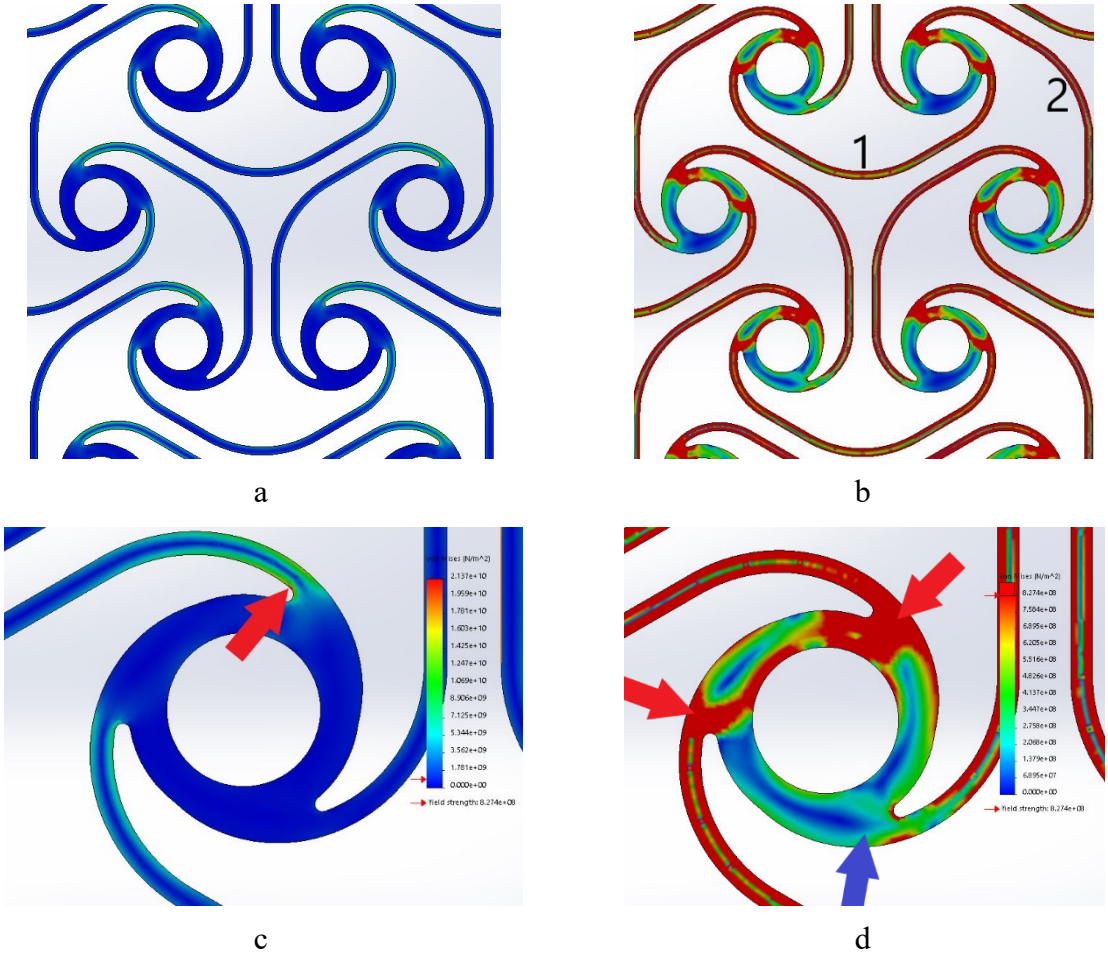

Figure 90: Wide-bow Y-axis Ti6Al4V simulations stress distribution diagram closeups: a) single pattern relative to the maximum stress, b) single pattern relative to the yield point with the ‘1’ and ‘2’ referring to the closed link, c) a node relative to the maximum stress with the red arrow indicating the location of the highest stress concentration, d) a node relative to the yield point with the red arrows showing areas with high-stress concentrations and the blue arrow showing the area with low-stress concentrations.

Figure 91 shows the Ti6Al4V simulation results for the deformation of the wide-bow Y-axis specimen. Figure 91a is the simulated deformation of the entire specimen and reached a calculated elongation of 220.13 mm. Further analysis reveals no auxetic behaviour in this axis of the scaffolding at this amount of elongation. In Figure 91b, a closeup of a single pattern at the simulated deformation, the single pattern has significantly deformed in the elongation axis while collapsing/contracting into itself in the perpendicular axis. On examination of a node in the initial state and the deformed state in Figure 91 c and d respectively, it can be seen how the node is rotated and deformed to be able to elongate.

The high-stress concentration points on the nodes are shown with the red arrow on Figure 91c and d and represents the same location. Therefore, the arrow positions give a good idea of the rotational deformation of the node, which is estimated to have rotated about 75° from the initial location. Figure 91d shows the stress diagram of a node when it is deformed. From this, it can be observed that the two links with the high-stress concentrations have deformed to their limits. The highest concentration link can be seen deforming past its limits and is most likely experiencing shear forces.

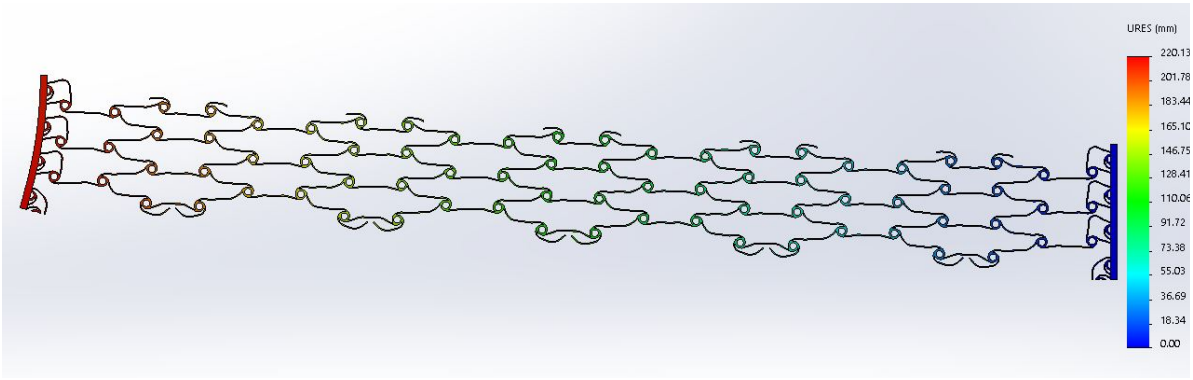

a

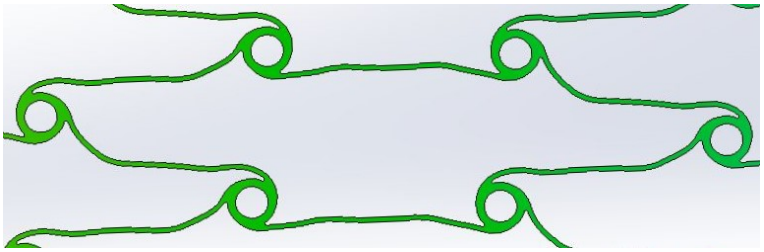

b

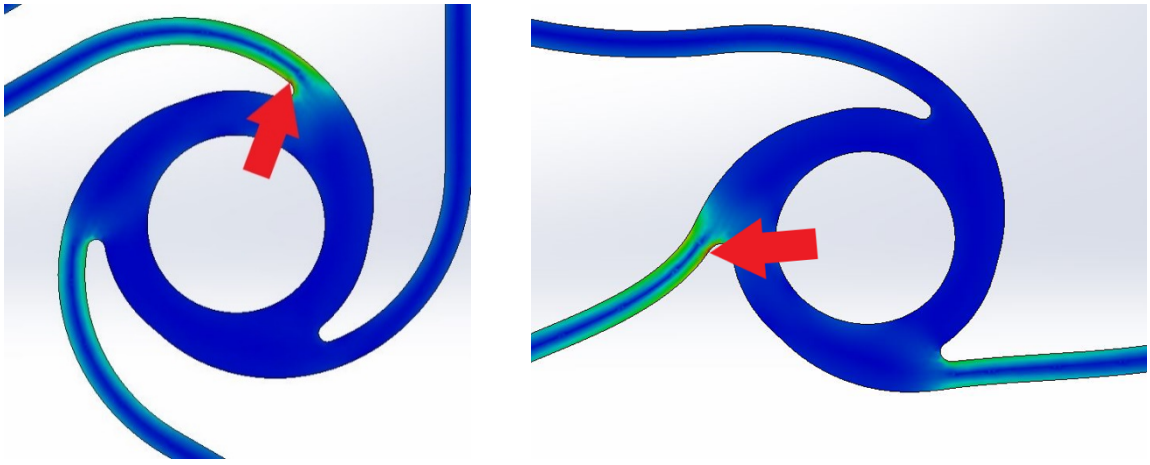

C d

Figure 91: Wide-bow Y-axis Ti6Al4V simulation deformation: a) shows the simulated deformation, b) closeup of a single pattern at the simulated deformation, c-d) rotation of a node with the red arrow indicating the same location.

5.1.3. Linked-spiral parallel-axis Ti6Al4V sample

The next simulation was for the parallel-axis of the Ti6Al4V linked-spiral, and the stress distribution diagrams can be seen in Figure 92. Figure 92a shows the stress distribution diagram relative to the maximum stress experienced by the specimen, and Figure 92b shows the stress distribution diagram relative to the yield point of the material. In Figure 92a, most stresses are relatively low, with only a few concentrated locations reaching much higher stress, to a maximum stress of 10.7 GPa. The likely points of failure of the scaffolding are seen in Figure 92b where the red section in the diagram shows stresses that exceed the material's yield point.

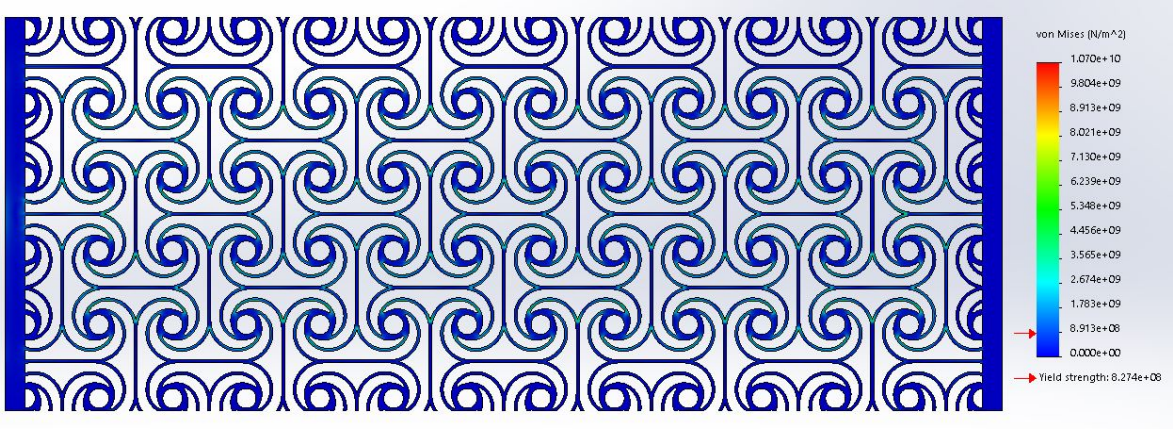

a

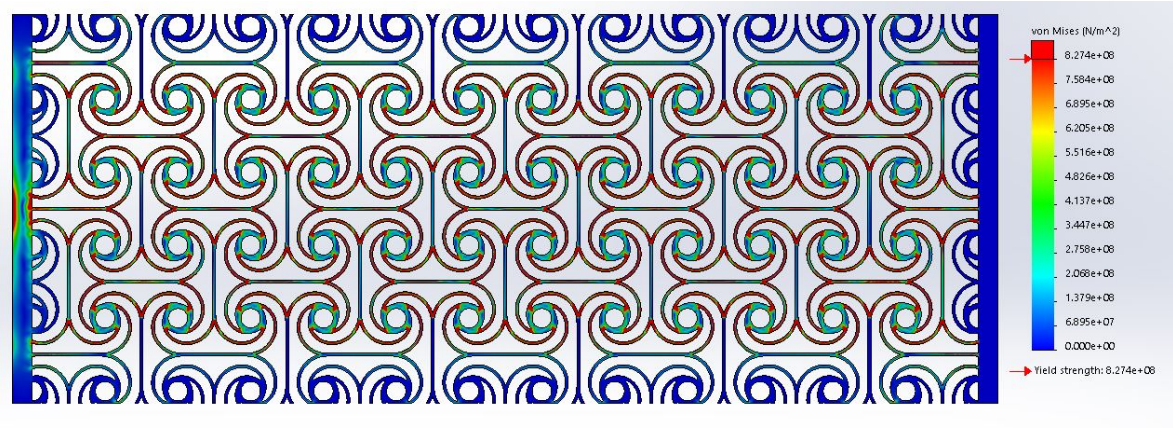

b

Figure 92: Linked-spiral parallel-axis Ti6Al4V simulations stress distribution diagrams at 1 kN loading: a) stress distribution relative to the maximum stress observed, b) stress distribution relative to the material's yield point.

The nodes and single patterns of the specimen are shown in Figure 93, where the scaffolding stress concentrations can be observed. Focusing on the single pattern in Figure 93 a and b, each link has a relatively high-stress concentration at the end of the link where it connects to the node and at the point where the links merge to form the merged-link section. Furthermore, the

links that connect to a merge-link section parallel to the elongation direction have lower and more evenly distributed forces. The links connecting to a merged-link section perpendicular to the elongation direction have higher stress concentrations at the node connection points and the merger point but lower to almost no stress in the merged-link section. On closer examination of the specimen at a single node in Figure 93c and Figure 93d, the concentration areas can be seen more clearly. Figure 93d shows the high concentrations areas with red arrows, the stresses in the merged-link section parallel to the elongation direction with the yellow arrow, and the low-stress areas of the merged-link section perpendicular to the elongation direction with the blue arrow.

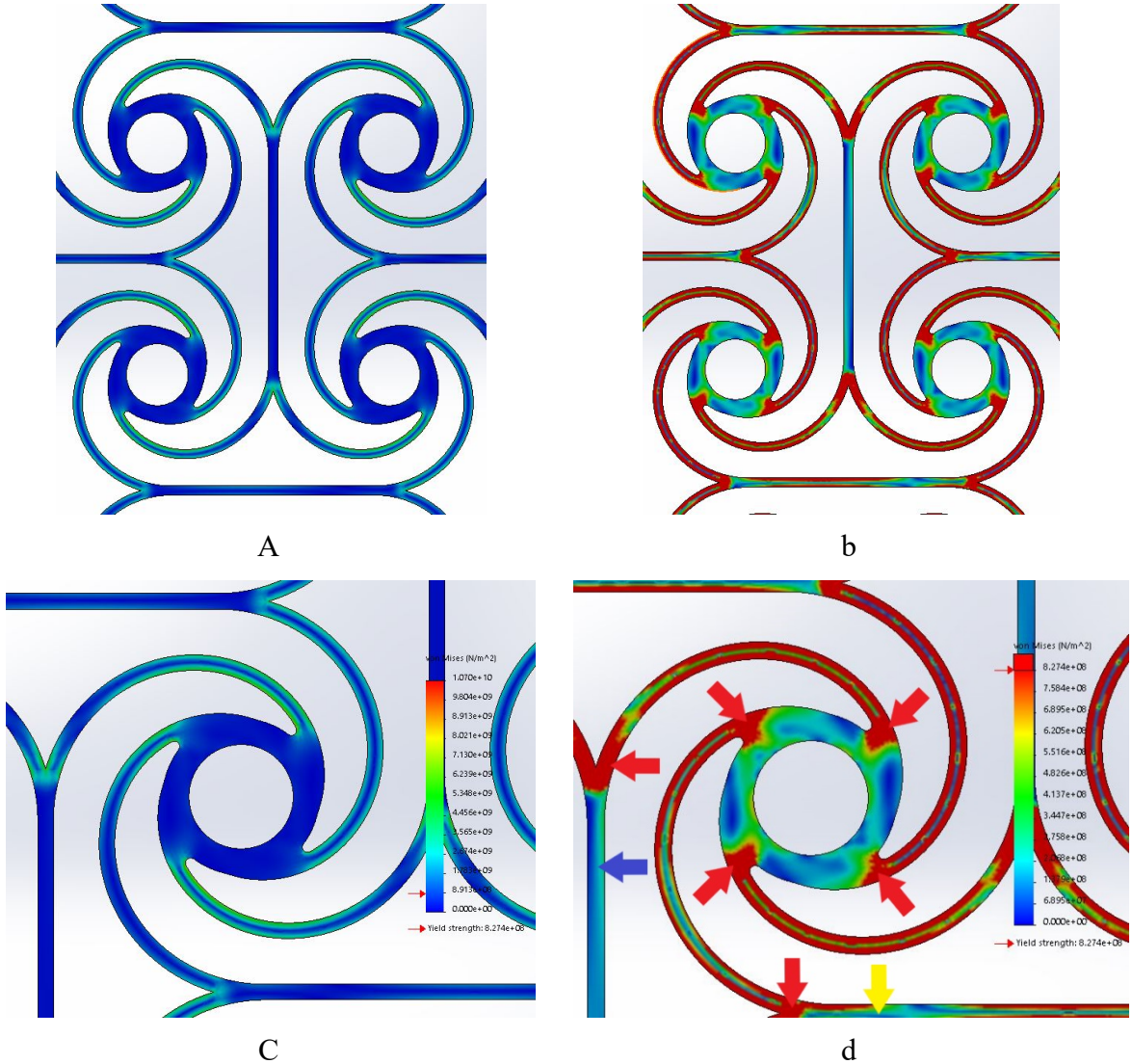

Figure 93: Linked-spiral parallel-axis Ti6Al4V simulations stress distribution diagram closeups: a) single pattern relative to the maximum stress, b) single pattern relative to the yield point, c) a node relative to the maximum stress, d) a node relative to the yield point with the red arrows showing areas with high-stress concentrations, the blue arrow showing the area with low-stress concentrations and the yellow arrow showing the merged-link section parallel to the elongation direction.

Figure 94a shows the complete deformation of the entire specimen where the specimen reached a maximum deformation length of 79.44 mm. The specimen displayed auxetic behaviour. Figure 94b shows the simulated deformation of a single pattern and how the nodes rotate when the scaffolding elongates and push the nodes away from each other, which is the cause of the auxetic behaviour. The merged-link sections parallel to the elongation direction buckle under the force of the nodes, rotating the links towards each other. However, the perpendicular merged-link sections did not buckle. This is most likely due to the links connecting adjacent nodes in the direction of elongation being under tensional force, and these pulling forces are the main factor causing the nodes to rotate.

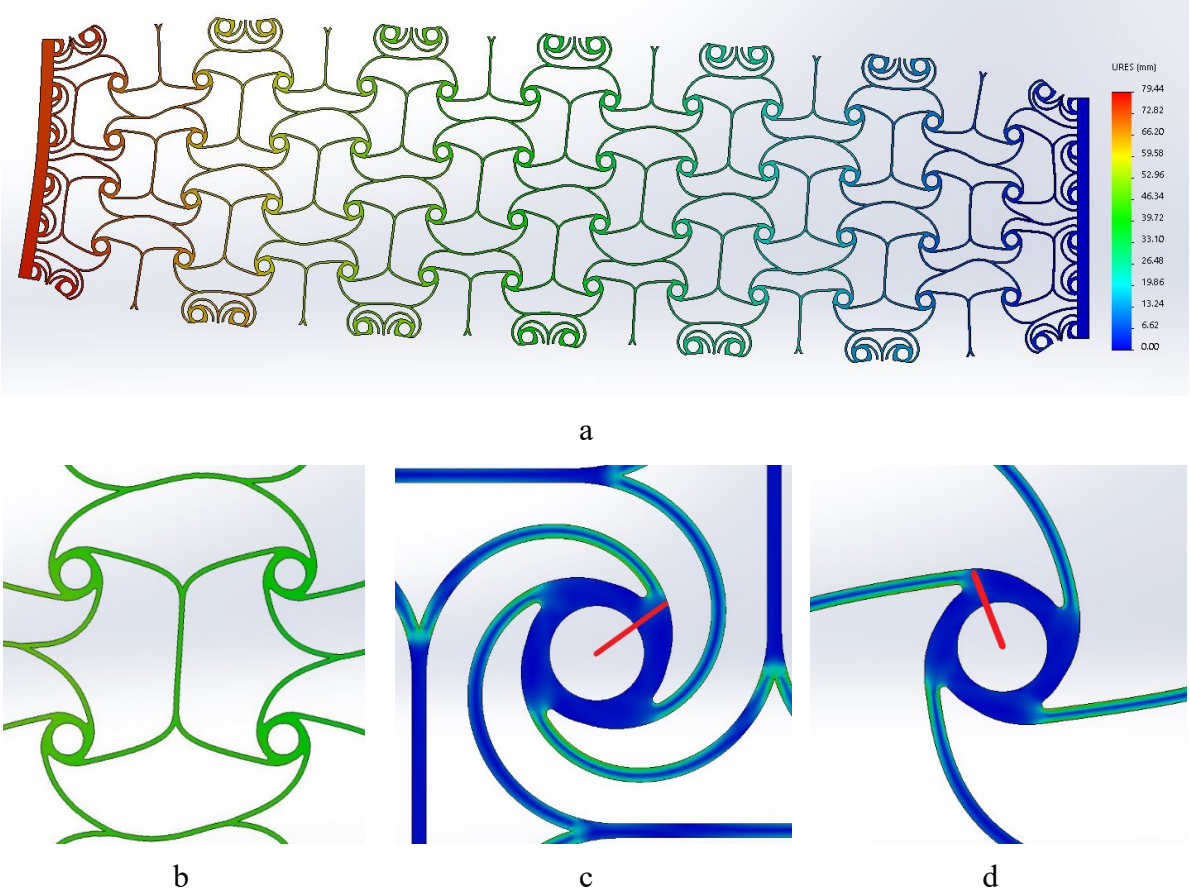

Figure 94: Linked-spiral parallel-axis Ti6Al4V simulation deformation: a) simulated deformation, b) closeup of a single pattern at the simulated deformation, c-d) rotation of a node with red lines indicating the same location.

Figure 94c and Figure 94d show the simulated stress distribution diagram of a single node's initial and deformed states from the Ti6Al4V linked-spiral in the parallel-axis. The red line on each of the figures represents the same position and is pointed from the centre of the node. This line gives a good indication of the amount of rotation the node experienced during elongation, which can be estimated to be around 80°.

5.1.4. Linked-spiral skew-axis Ti6Al4V sample

The final simulation was for the Ti6Al4V linked-spiral skew-axis design. The stress distribution diagrams for this specimen can be seen in Figure 95. The maximum stress experienced by the specimen is shown in the stress distribution diagram in Figure 95a. The stress distribution diagram relative to the material's yield point is shown in Figure 95b. In Figure 95a, most stress concentrations are relatively low. However, there are points in the scaffolding that reached stress levels up to a maximum of 10.17 GPa. Figure 95b has a more detailed stress distribution diagram; the red sections in the diagram indicate stresses that exceed the material's yield point and are likely points of failure.

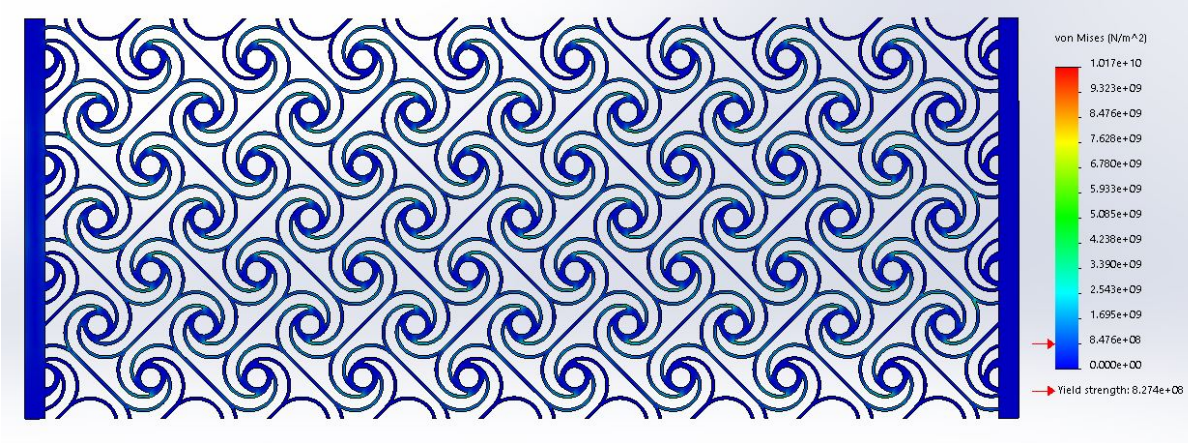

A

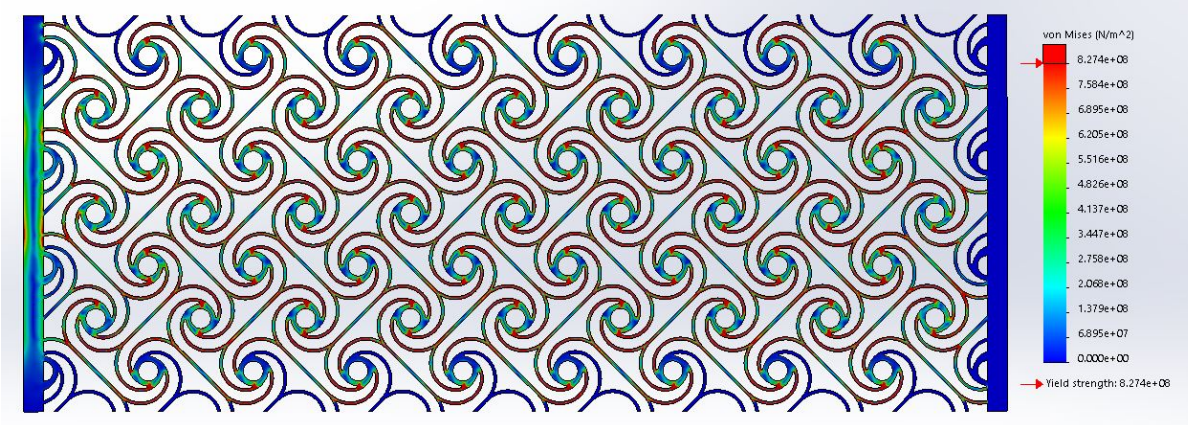

B

Figure 95: Linked-spiral skew-axis Ti6Al4V simulations stress distribution diagrams at 1 kN loading: a) stress distribution relative to the maximum stress observed, b) stress distribution relative to the material yield point.

The linked-spiral skew-axis scaffolding simulated single patterns and nodes stress concentrations are shown in Figure 96. In Figure 96a and Figure 96b, the primary stress concentrations are at the links that connect perpendicular to the elongation direction to the

nodes. It is important to note that the stress concentrations are not mirrored with the nodes but stay perpendicular to the links for each node case. The merged-link sections for both axes have similar stress distribution. This was expected as they are at the same angle relative to the elongation direction and should experience similar forces. Figure 96 c and d show the stress distribution diagrams for a single node relative to the maximum stress experienced by the specimen and relative to the yield strength of the material, respectively. In Figure 96c, the locations of the highest stress concentrations experienced by the scaffolding are indicated with red arrows. Figure 96b shows the high concentration sections perpendicular to the elongation direction with red arrows and the low-concentration sections in line with the elongation direction with blue arrows.

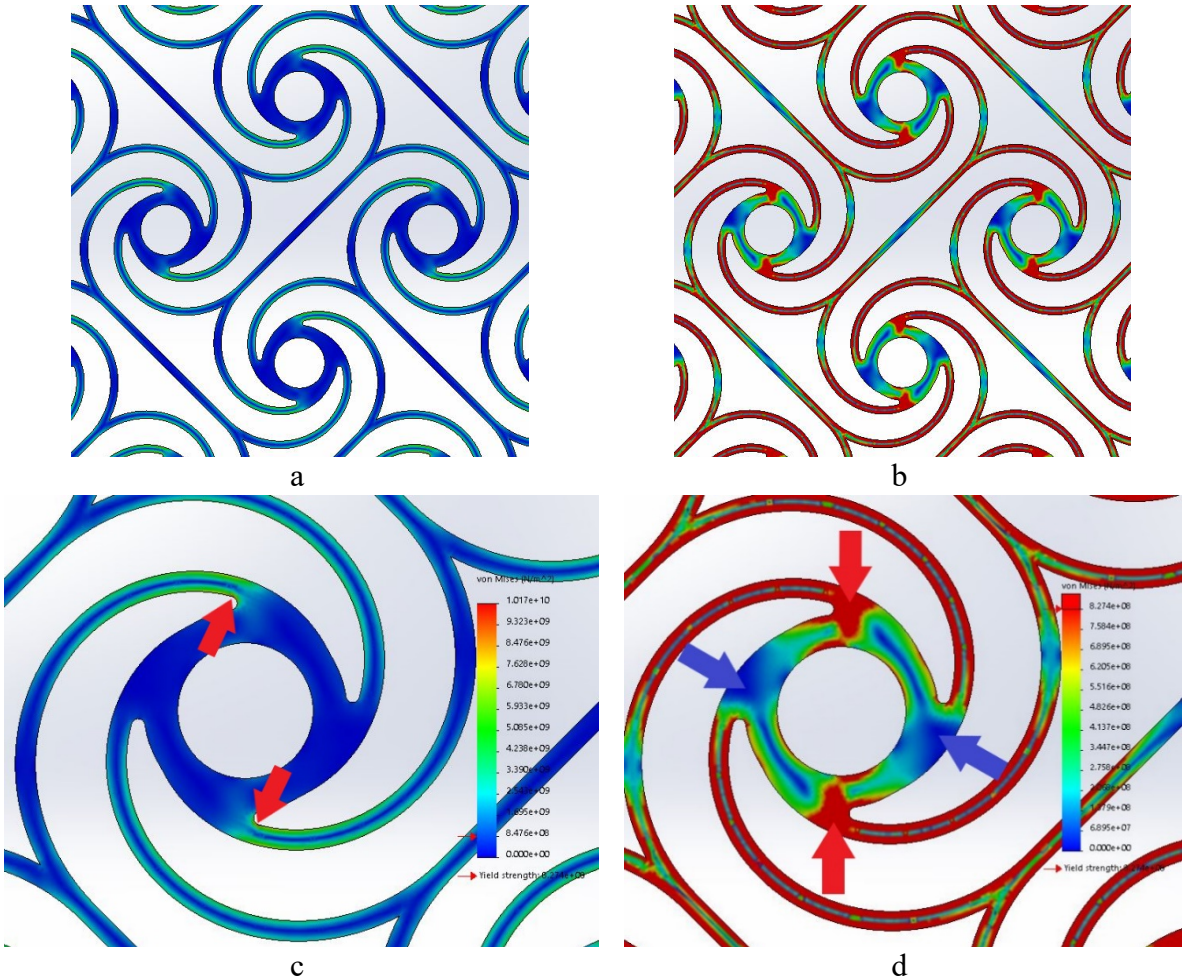

Figure 96: Closeups of linked-spiral skew-axis Ti6Al4V simulation stress distribution diagram: a) single pattern relative to the maximum stress, b) single pattern relative to the yield, c) a node relative to the maximum stress with the red arrows indicating the locations of the highest stress concentrations, d) a node relative to the yield point with the red arrows showing areas with high-stress concentrations and the blue arrows showing the areas with low-stress concentrations.

The simulated deformation of the Ti6Al4V linked-spiral skew-axis specimen can be seen in Figure 97. Figure 97a shows the entire specimen's simulated deformation and has a maximum simulated elongation of 82.5 mm. The auxetic behaviour of the specimen is observed in Figure 97a. The deformation of a single pattern seen in Figure 97b indicates that the nodes have expanded away from adjacent nodes to cause the auxetic behaviour. However, the pattern has deformed more in the elongation direction, causing the merged-link sections to warp and buckle.

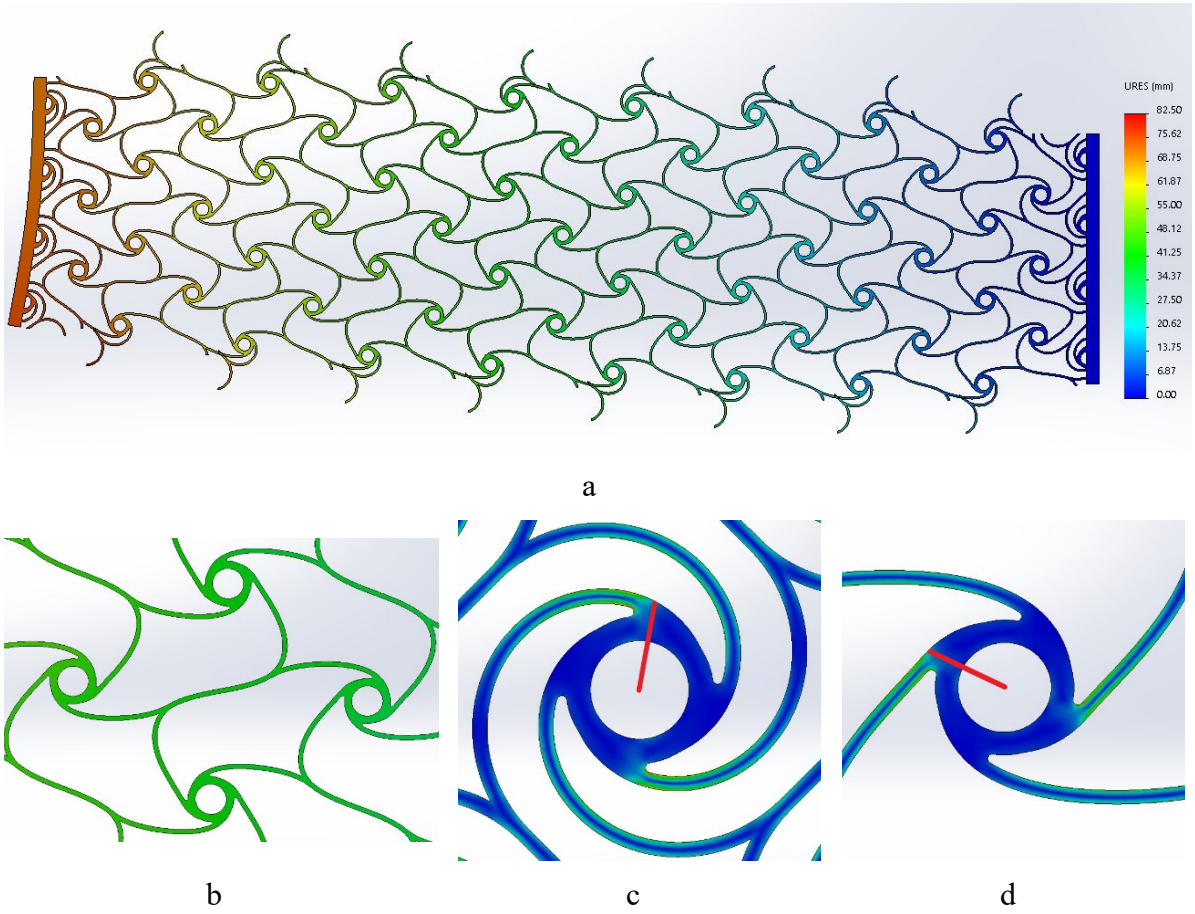

Figure 97: Linked-spiral skew-axis Ti6Al4V simulation deformation: a) the simulated deformation, b) closeup of a single pattern at the simulated deformation, c-d) rotation of a node with the red line indicating the same location.

Figure 97 c and d show the simulated stress distribution diagram of a single node's initial and deformed states from the Ti6Al4V linked-spiral in the skew-axis. The red line on each of the figures represents the same position and is pointed from the centre of the node. These lines indicate the amount of rotation that the node experienced during elongation and is estimated to be around 70°. The link with the high concentration section is seen in Figure 97 d. Compared to the arced initial shape, the links deformed into an almost straight line, while the low-stress links mostly still have an arced shape, most probably due to low stress.

5.2 Mechanical properties of Ti6Al4V scaffoldings

5.2.1. Ti6Al4V 2 x 2 cm sample CT scanning

In order to verify the dimensional accuracy of the Ti6Al4V scaffoldings, two 2 x 2 cm samples were first fabricated, see Figure 98a below. The samples were then sent for CT scanning, which provides highly accurate 3D models of the Ti6Al4V 2 x 2 cm samples. Figure 98b shows one of the models produced from the CT scan. The CT scan models were then compared to the original 3D model that the samples were fabricated from to determine the accuracy of the fabricated samples.

Figure 98c shows a wall thickness evaluation of the CT scanned model, where the majority of the wall thicknesses are near 0.32 mm, which is close to the thickness of 0.3 mm of the original design. This excludes the sections that were cut thinner and are found to be around 0.1 mm thick as the wall thickness was also thinner on the original model. The original model had a wall thickness of 0.3 mm, and this gives a maximum deviation of -0.06 mm and an average deviation of ± 0.04 mm, which is confirmed in Figure 98 e). The Ti6Al4V sample deviations are within acceptable margins, and therefore Ti6Al4V sample tensile testing can continue.

Figure 98d is a sectioned view of the original and CT scanned models overlapping; the yellow lines represent the original model, and the CT scanned model is represented by the white infill. Lastly, Figure 98e is a deviation analysis of where the original and CT scanned models overlap, and the deviation between the two models can be seen.

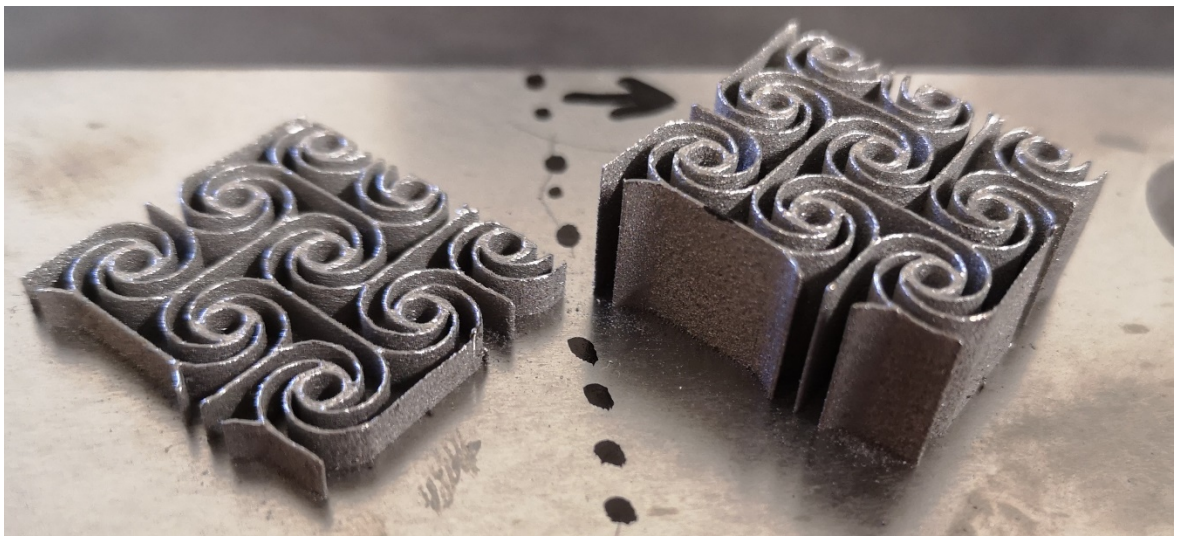

a

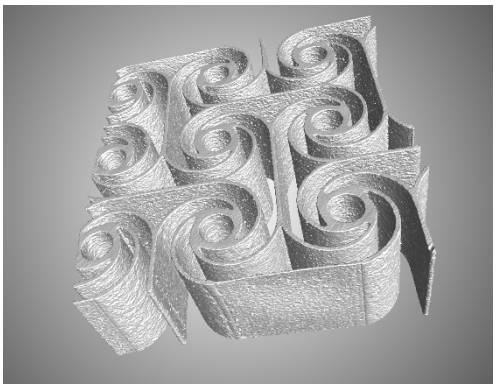

b

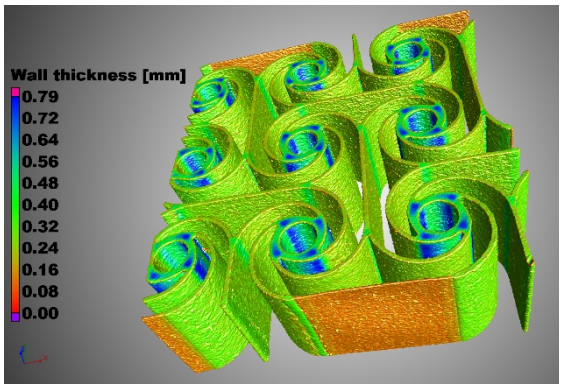

c

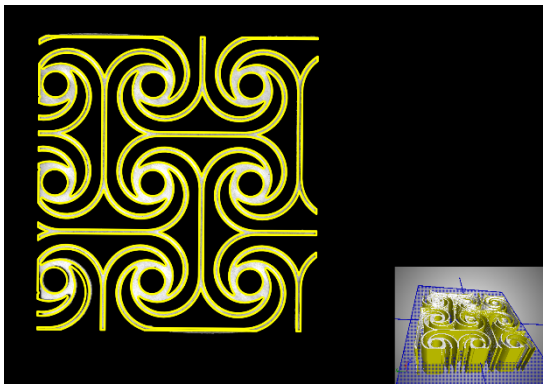

d

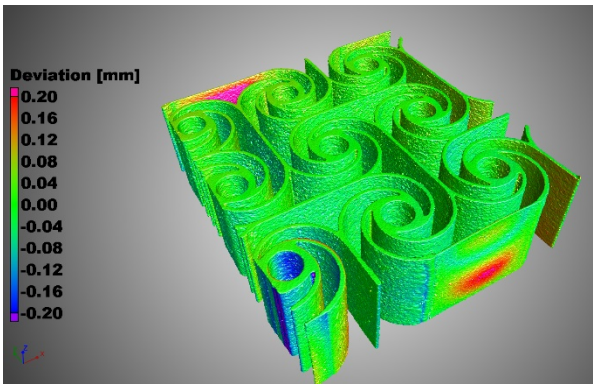

e

Figure 98: Ti6Al4V 2 x 2 cm samples: a) Ti6Al4V part, b) CT scanned model, c) wall thickness range, d) sectioned view of the CT scan model in white and the original model indicated with the yellow outline, e) representation of the amount of deviation between the CT scanned model and the original model.

5.2.2. Tensile testing of the Ti6Al4V wide-bow scaffoldings

X-axis wide-bow samples

Figure 99 below shows the tensile test of the three Ti6Al4V X-axis wide-bow specimens marked (i) to (iii). The images show the progression of the tensile tests from the initial resting state (a) to directly before failure (e) and finally after failure has occurred (f). From these images, it seems that the deformation of all three specimens is similar throughout the elongation process. All three specimens have similar horizontal expansion with vertical elongation, proving that the wide-bow is auxetic in the X-axis. However, the X-axis wide-bow specimen did not show auxetic behaviour in the polymer tensile tests. This is most likely due to the Ti6Al4V specimen having more patterns in the structure, allowing for a better representation of the scaffolding's behaviour. Furthermore, the specimens all expanded horizontally as they elongated, meaning that the specimens failed each time before the structure could collapse in on itself.

i)

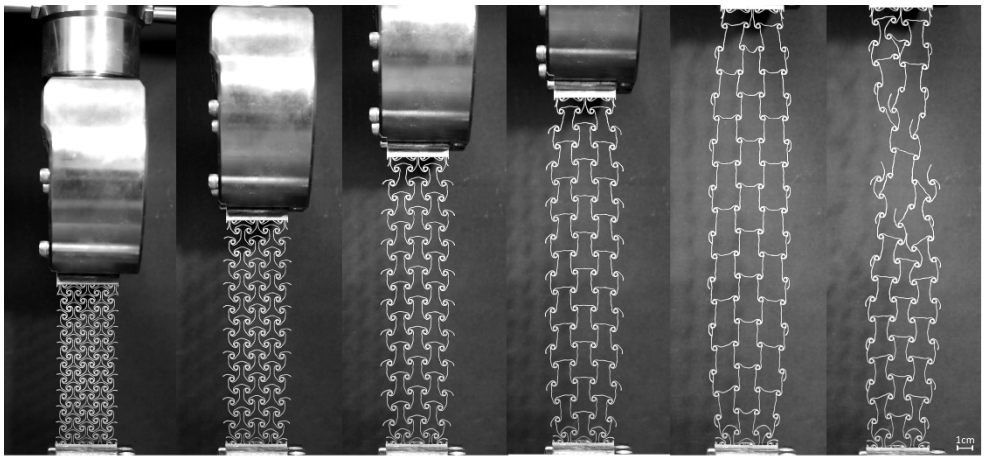

a b c d e f

ii)

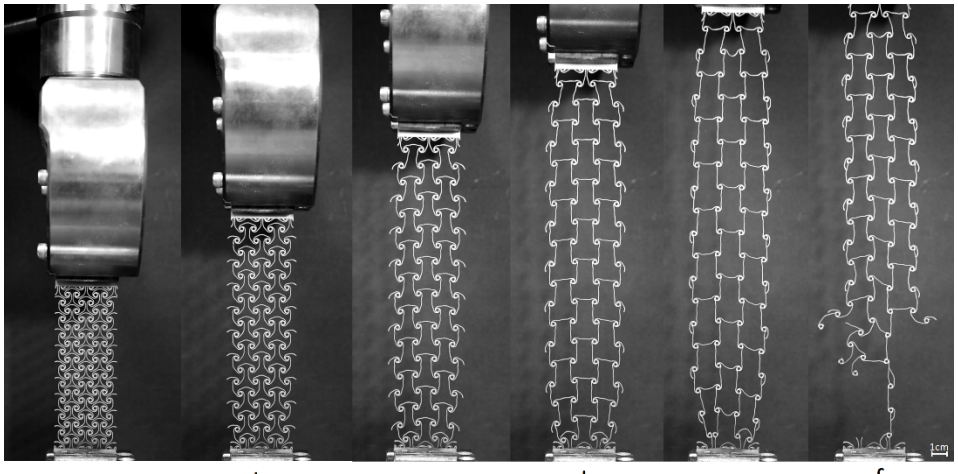

a b c d e f

iii)

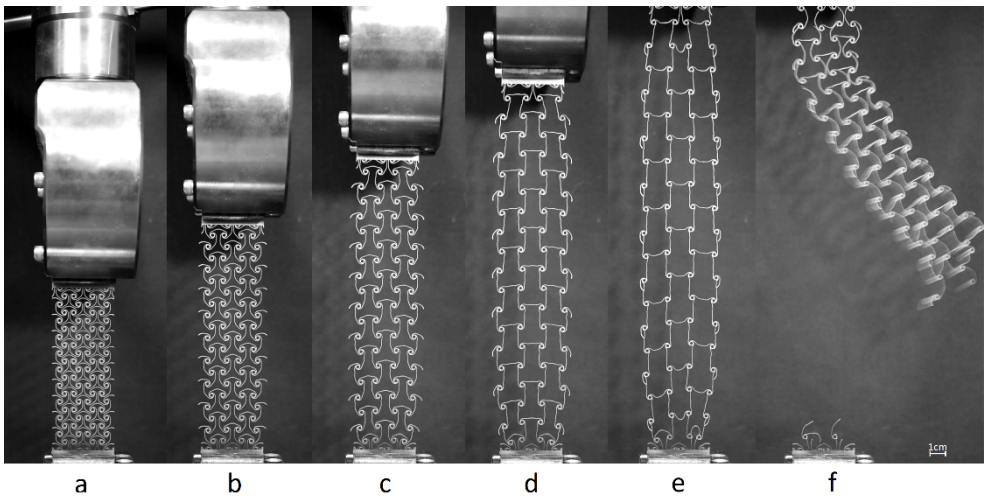

Figure 99: Tensile testing of the three Ti6Al4V X-axis wide-bow specimens: i) first specimen, ii) second specimen, iii) third specimen and a) a state of the specimen before the tensile test, b-d) deformation of the specimen during elongation, e) specimen moments before failure, f) specimen after failure had occurred.

Figure 100 is a closer view of the Ti6Al4V X-axis wide-bow specimens before and after the failure occurred. The points where the failure occurred are marked red for each specimen below. An examination of the failure point of the three specimens reveals that for both the second (ii) and the last (iii) specimens, the points of failure were concentrated at the end of the structure, similar to the polymer samples. However, the first specimen (i) broke close to the centre of the structure. The first (i) and second (ii) specimens did not fail completely, with some nodes connecting the scaffolding to both ends. It is important to note that the second specimen (ii) was quite close to complete failure. Furthermore, the third specimen (iii) suffered a complete failure, with the scaffolding completely separated from the one end.

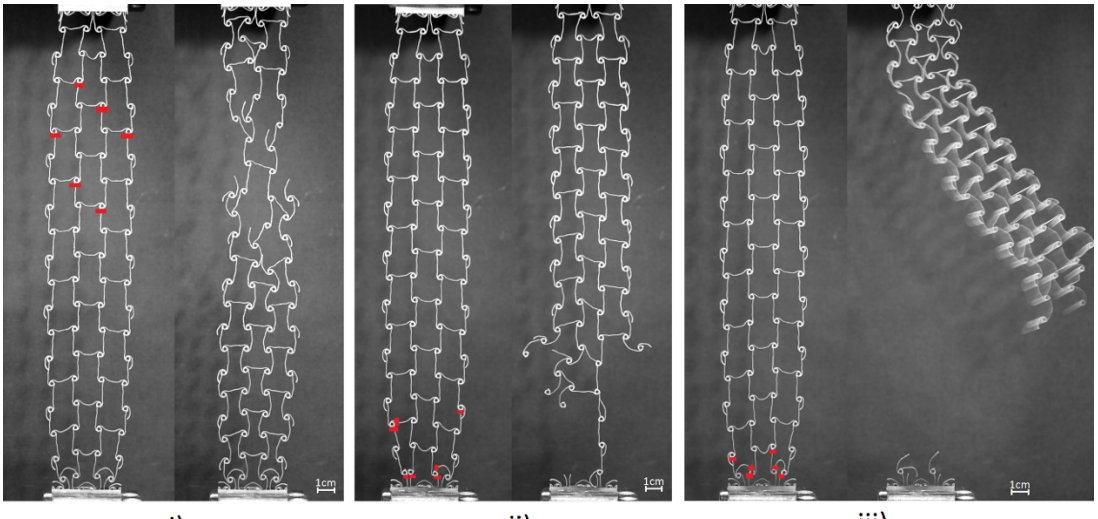

Figure 100: Failure points of Ti6Al4V X-axis wide-bow specimens (red lines indicate the points where the specimen failed): i) first specimen, ii) second specimen, iii) third specimen.

The graph in Figure 101 below shows the load-displacement curve of the three Ti6Al4V X-axis wide-bow specimens. The first specimen is shown in blue and reached a peak load of 92.5 N at a displacement of 175.5 mm before experiencing a major failure. A major failure is where the specimen does not completely fail, but the load on the specimen falls below half of the peak load that the specimen has experienced. The second specimen is shown in red and reached a peak load of 90.3 N, a displacement of 173.5 mm, before experiencing a major failure. Lastly, the third specimen is shown in green and reached a peak load of 102.8 N at a displacement of 189.1 mm before experiencing a complete scaffolding failure. The graph shows that all three specimens had similar load-displacement curves up and until 173 mm, where the scaffoldings started to fail. At the failure point, the first and second specimens failed at a relatively similar point; however, the first specimen had a sharp and drastic major failure, and the second specimen had various small link failures before two large failures occurred. The third specimen could withstand a higher load but suffered a complete failure a few moments after a small failure occurred.

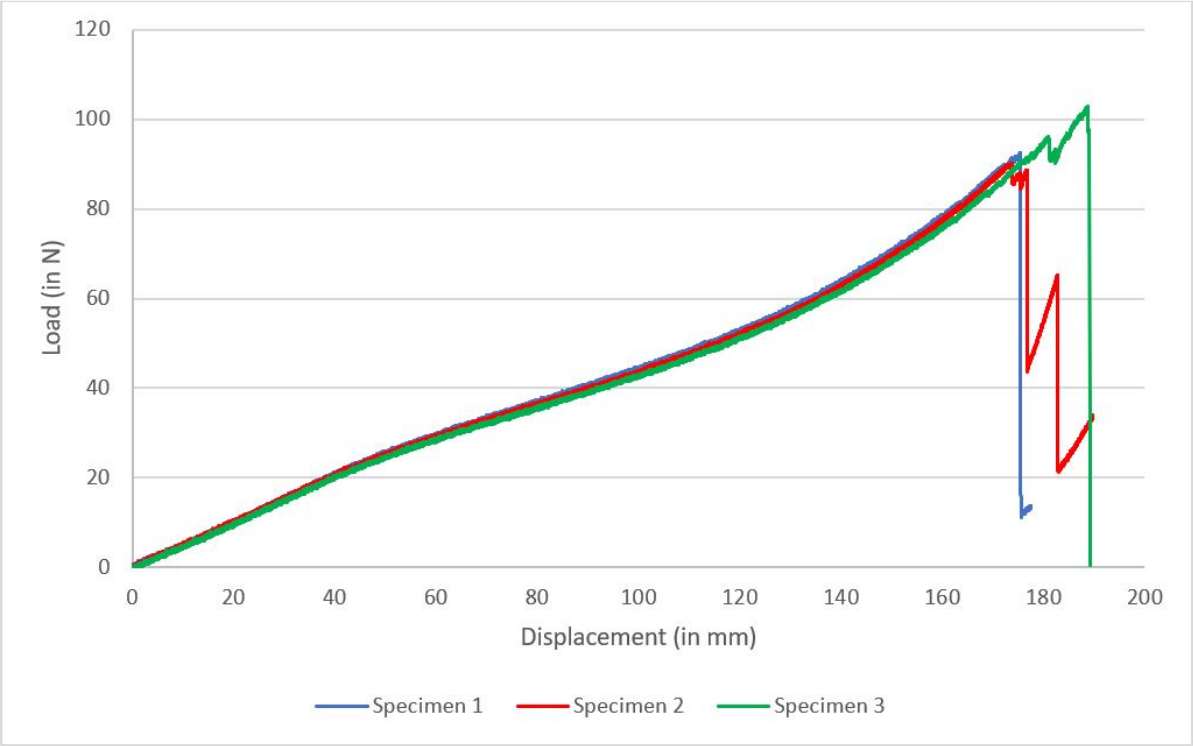

Figure 101: Load-displacement curves for tensile tests of Ti6Al4V X-axis wide-bow samples.

Y-axis wide-bow samples

The tensile tests for the three Ti6Al4V Y-axis wide-bow specimens are shown in Figure 102 marked (i) to (iii). The progression of the tensile tests can be seen from (a), which is the initial state before the tests begin to (e) the specimen moments before failure occurred and finally (f),

which shows the specimen after failure had occurred. All three specimens showed similar elongational behaviour up and until failure started to occur. In the images in Figure 102, the specimens all slowly contracted as they elongated; this is non-auxetic behaviour. This is similar behaviour to the polymer Y-axis wide-bow sample in the preliminary tensile tests, but the contraction is not as extreme as the preliminary tensile test. Furthermore, all three specimens did not suffer complete failure, leaving at least a single link connection between the two ends. The first specimen (i) shows minor damage despite suffering a major failure, the second specimen (ii) suffered more damage leaving only a single connection path after a major failure occurred, and finally, the third specimen (iii) suffered moderate damage leaving two connection paths after a major failure occurred.

i)

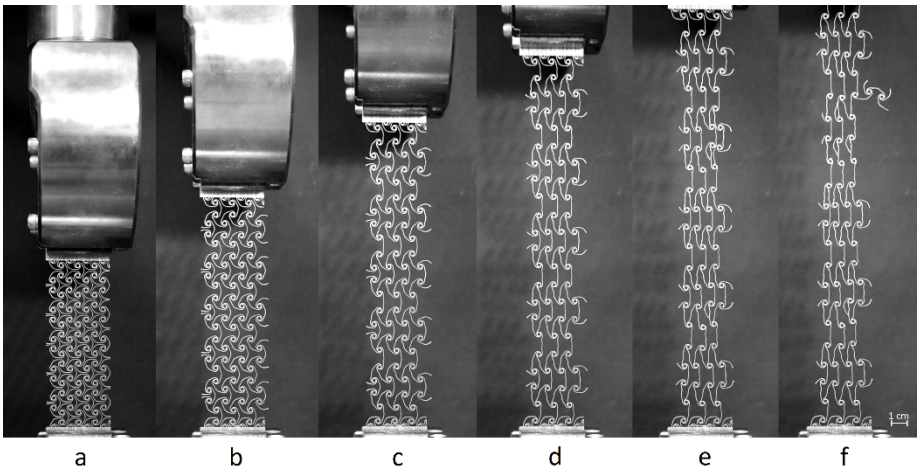

ii)

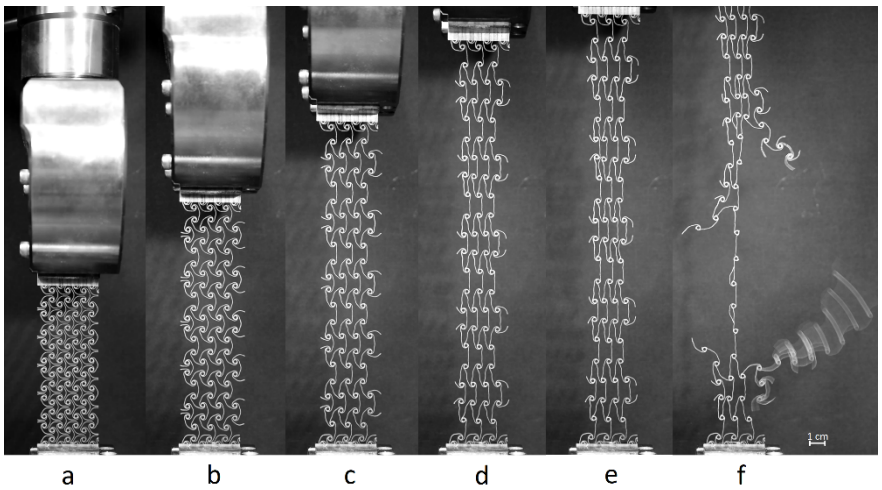

iii)

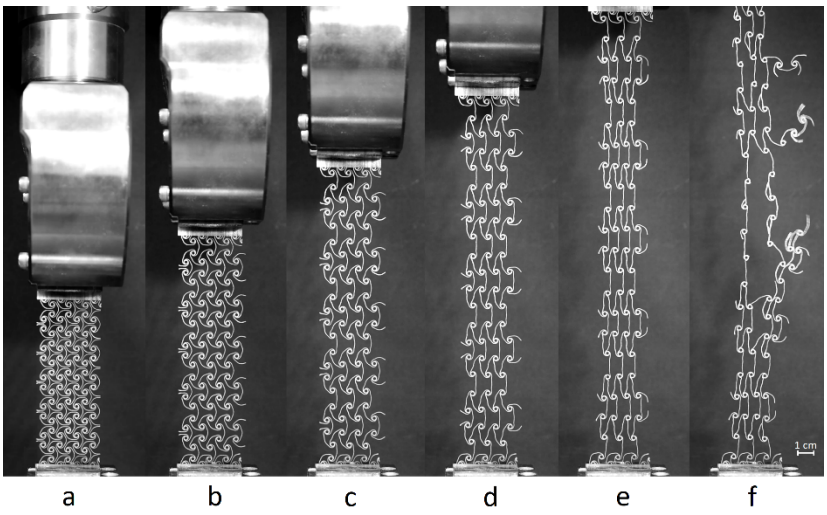

Figure 102: Tensile testing of the three Ti6Al4V Y-axis wide-bow specimens: i) first specimen, ii) second specimen, iii) third specimen and a) neutral state of the specimen before the tensile test, b-d) deformation of the specimen during elongation, e) specimen moments before failure, f) specimen after failure had occurred.

A closer view at the failure points of the three Ti6Al4V Y-axis wide-bow specimens in Figure 103 below shows the moment before failures occurred on the left of each image and after the failure occurred on the right. The points that failed are marked in red. The points where failure occurred are distributed throughout the scaffolding, with most failures occurring in or around the centre of the scaffolding. This is different to the polymer preliminary specimen that failed at the end of the scaffolding and suffered a complete failure.

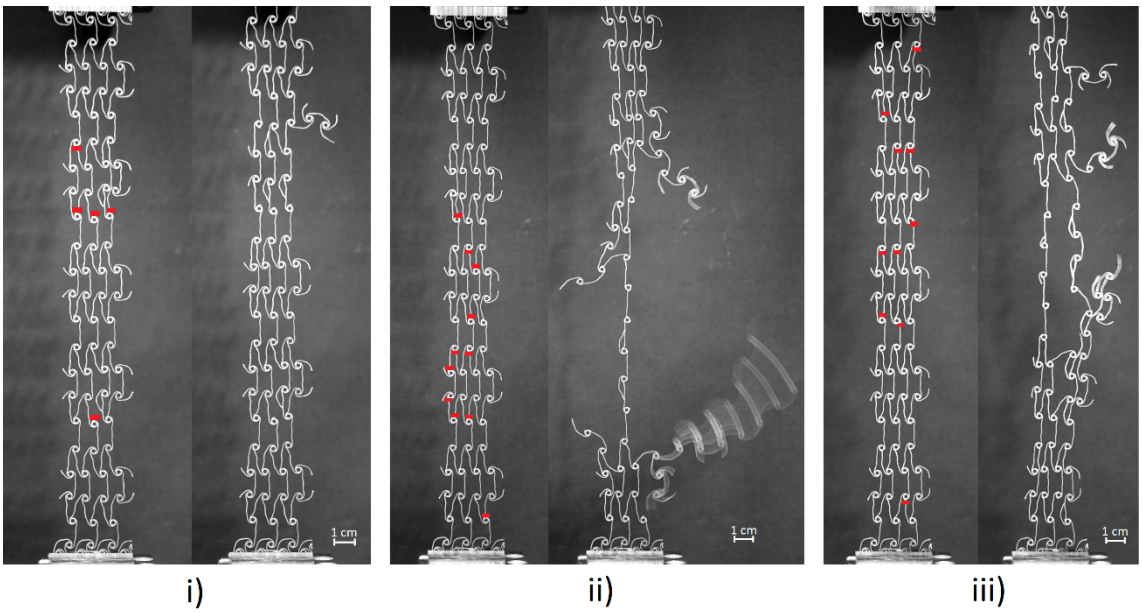

Figure 103: Failure points of Ti6Al4V Y-axis wide-bow specimens (red lines indicate the points where the specimen failed): i) first specimen, ii) second specimen, iii) third specimen.

The graph in Figure 104 below shows the load-displacement curve of the three Ti6Al4V Y-axis wide-bow specimens. The first specimen is shown in light blue and reached a peak load of 47.9 N at a displacement of 165.5 mm before experiencing a major failure. The second specimen is shown in orange and reached a peak load of 65.6 N, a displacement of 203.4 mm, before experiencing a major failure. Lastly, the third specimen is shown in purple and reached a peak load of 67.0 N at a displacement of 207.5 mm before experiencing a major failure. All three specimens had similar curves, especially the second and third specimens, which are almost indistinguishable from each other up and until about 170 mm of displacement. Furthermore, the first specimen started failing just after 155 mm of displacement, which is about 10 mm before major failure of the specimen occurred. The second and third specimens started failing at around 180 mm and only failed around 25 mm later. The first specimen had four very small failures before a major failure occurred, the second specimen had two small failures before a major failure occurred, and the third specimen had four small failures before a major failure occurred.

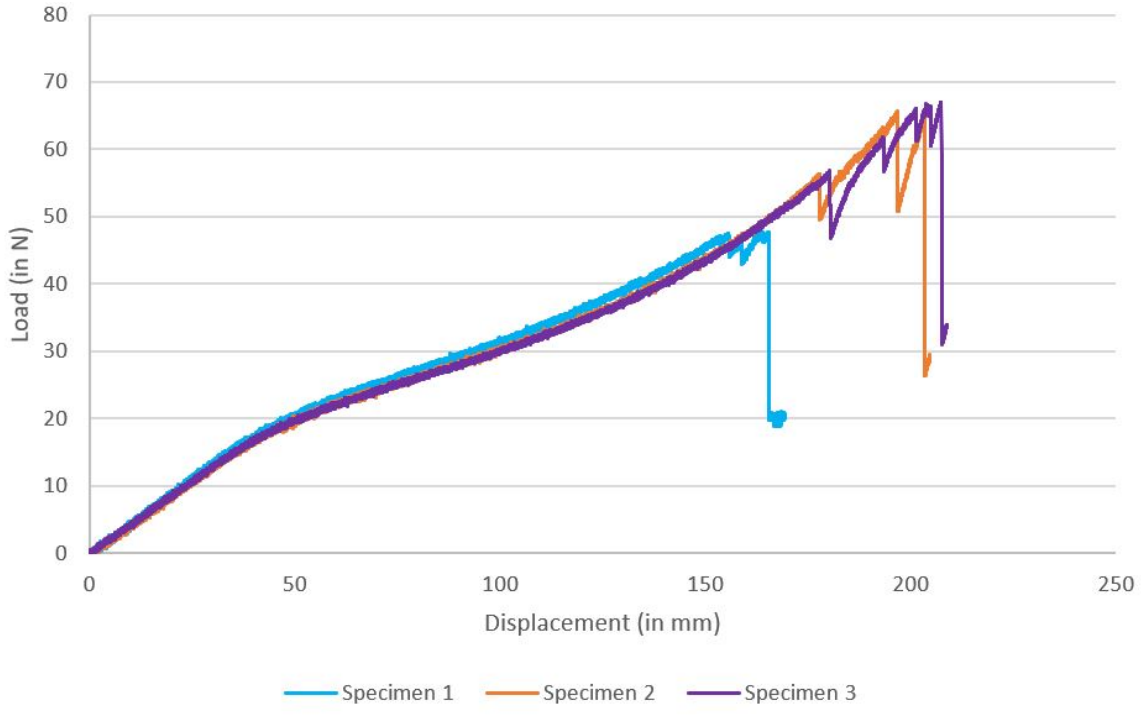

Figure 104: Load-displacement curves for tensile tests of Ti6Al4V wide-bow Y-axis samples.

Wide-bow X- and Y-axis comparison

The graph below in Figure 105 shows all the Ti6Al4V wide-bow specimen results to compare the X- and Y-axes. The X-axis specimens all reached a higher peak load than the Y-axis, but most of the Y-axis specimens reached a higher displacement before failure occurred. This is similar to what was found in the preliminary polymer tensile test for the wide-bow scaffolding.

Furthermore, the results show that failure for the first and second X-axis specimens and the second and third Y-axis specimens started just after 175 mm of displacement. Note that the Y-axis specimens took longer before having a major failure, but the X-axis specimens had a major failed almost directly after the first failure occurred; this is likely due to the X-axis being under more tension, causing more shock when a large failure occurred and resulting in a larger chain reaction. Lastly, only one of the six Ti6Al4V wide-bow specimens suffered a complete failure (the third X-axis specimens). It is also important to note that this specimen reached the highest peak load of all the wide-bow specimens, reinforcing the theory that the higher tension causes a larger chain reaction.

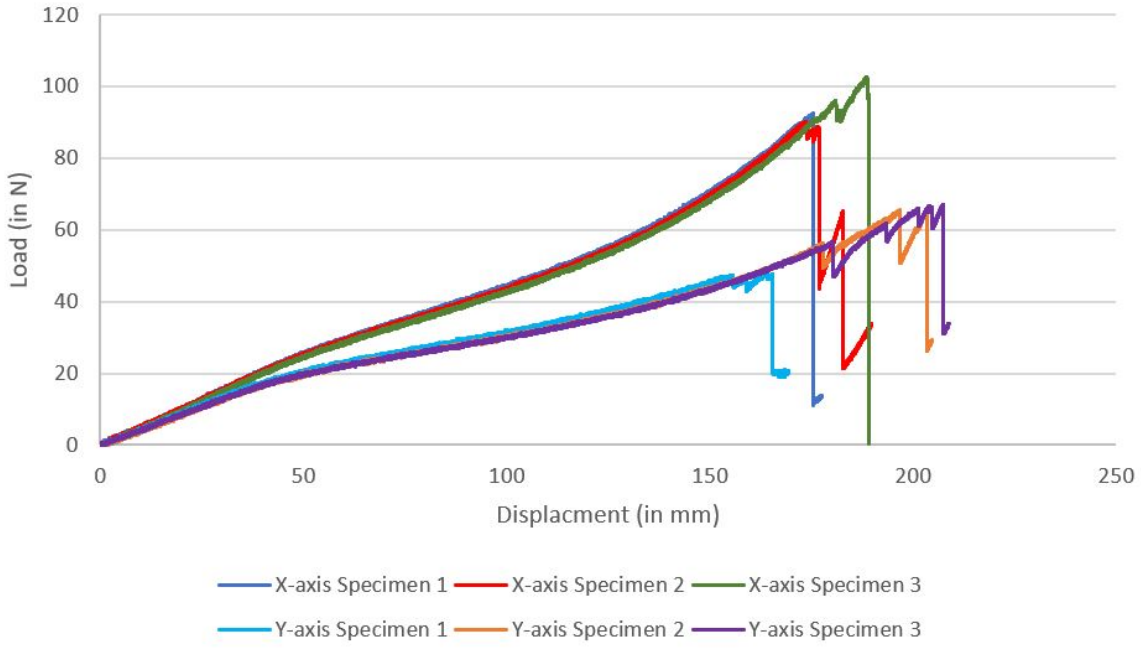

Figure 105: Load-displacement curves for tensile tests of Ti6Al4V wide-bow X- and Y-axis samples.

5.2.3. Tensile testing of the Ti6Al4V linked-spiral scaffolding

Parallel-axis linked-spiral samples

The tensile tests of the three Ti6Al4V parallel-axis linked-spiral specimens are shown in Figure 106 below, with the first specimen (i) at the top followed by the second (ii) and third (iii) specimens. Firstly, none of the specimens suffered a complete failure. Instead, all three specimens experienced a major failure where the load on the scaffolding fell below half of the peak load after a variety of link failures occurred. Furthermore, the specimens have identical horizontal expansion as they elongated until failure of the scaffoldings started to occur. The horizontal expansion with the elongation of the scaffoldings is evidence of auxetic behaviour

and was also observed for the parallel-axis of the linked-spiral in the preliminary polymer tensile test. However, in the preliminary tensile test, the parallel-axis linked-spiral specimen started to contract again before failing, but in the Ti6Al4V tensile test, the specimens started to fail before collapsing horizontally.

i)

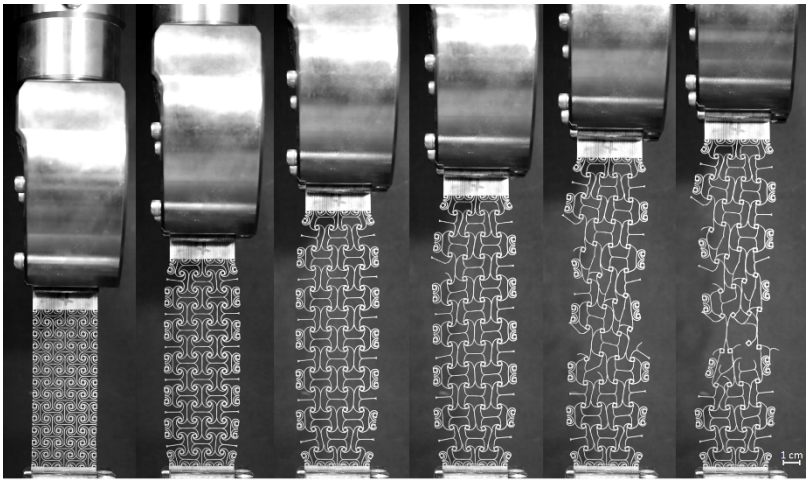

a b c d e f

ii)

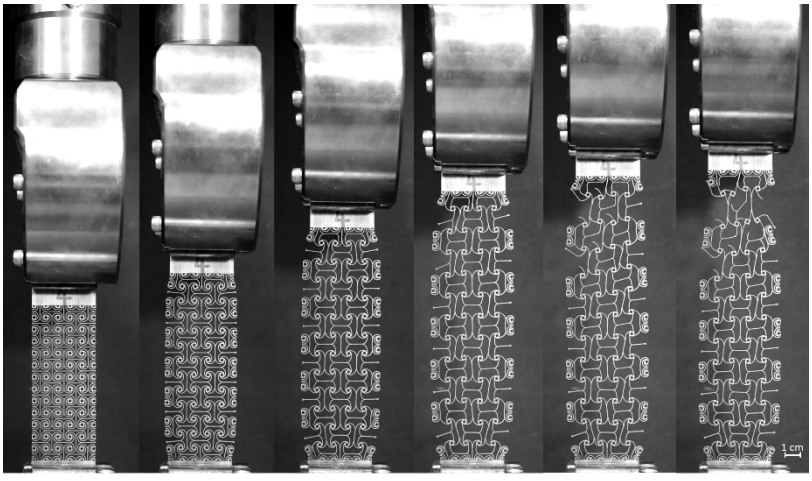

a b c d e f

iii)

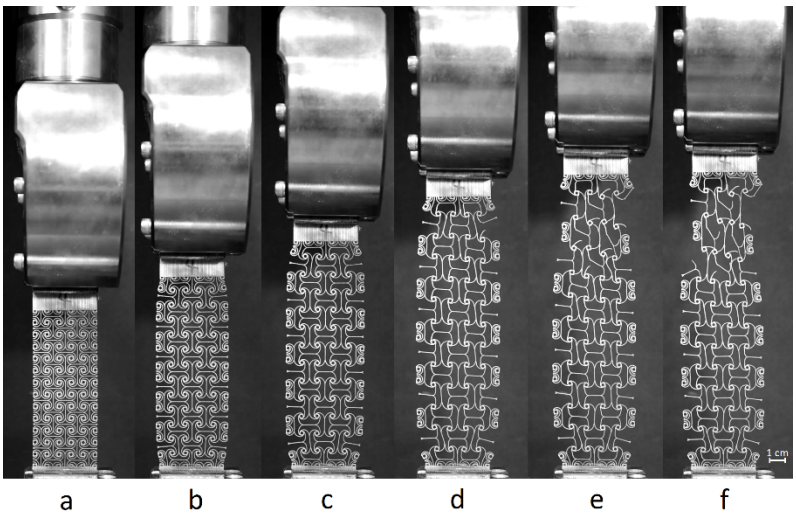

Figure 106: Tensile testing of the three Ti6Al4V parallel-axis linked-spiral specimens: i) first specimen, ii) second specimen, iii) third specimen and a) neutral state of the specimen before the tensile test, b-d) deformation of the specimen during elongation, e) specimen moments before failure, f) specimen after failure had occurred.

A closer view of the failure point of the Ti6Al4V parallel-axis linked-spiral specimens is found in Figure 107. All the specimens experienced a variety of smaller failures between links before the chain reaction that caused a major failure. Therefore, three sections were taken from the tensile testing images in Figure 106 correlating with image d-f in that order. This shows the first type of small initial failures between links before the larger major failure in blue, and the links that failed during the chain reaction that caused the major failures are shown in red. Furthermore, at the failure points, the initial and chain reaction failures are generally in the same areas for each specimen, which makes sense as this would be the weakest part of the scaffold as it has already been damaged. The failure point for the second (ii) and third (iii) specimens are located towards the end of the specimens, but the failure point of the first (i) specimen is located more to the centre of the specimen. It is noted that the first specimen (i) has more failure points than the other two specimens.

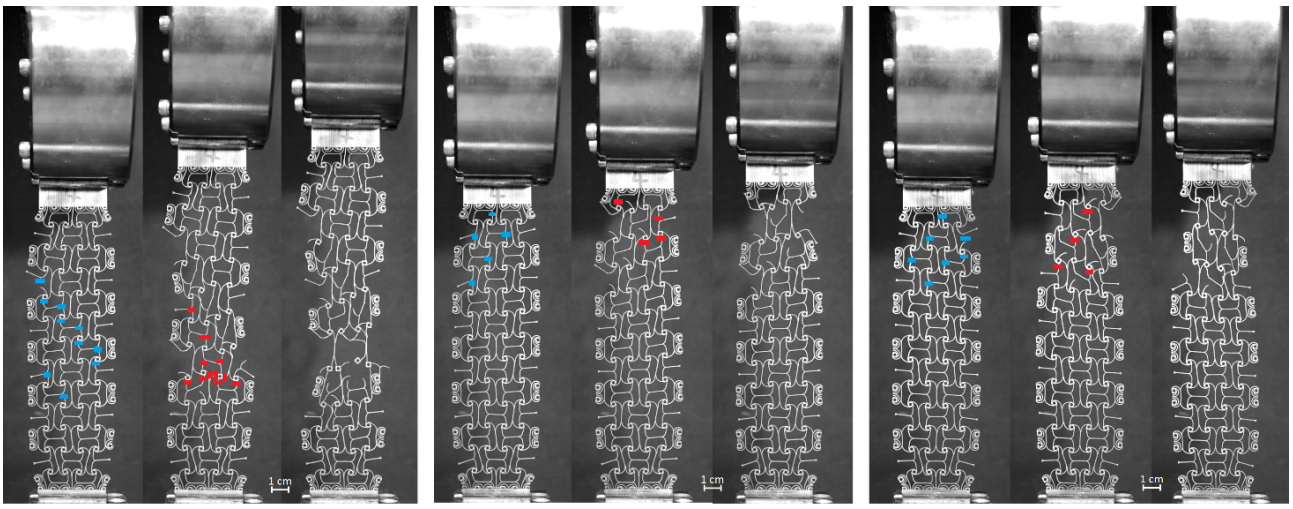

Figure 107: Failure points of Ti6Al4V parallel-axis linked-spiral specimens (blue lines indicated where the specimen failed before the major failure occurred and red lines indicate the points that failed during the occurrence of the major failure): i) first specimen, ii) second specimen, iii) third specimen.

The graph in Figure 108 displays the tensile test results of the Ti6Al4V linked-spiral parallel-axis specimens. The first specimen is shown in blue and reached a peak load of 160.9 N at a displacement of 78.4 mm before experiencing a major failure. The second specimen is shown in red and reached a peak load of 145.5 N, a displacement of 72 mm before experiencing a major failure. The third specimen is shown in green and reached a peak load of 148.6 N at a displacement of 76.5 mm before experiencing a major failure. All three specimens had an identical load-displacement curve up and until failure started to occur at around 70 mm of displacement. Additionally, the first (i) and third (iii) specimens failed at almost the same displacement as the second (ii) specimen failing after about 2 mm. Furthermore, all three specimens show evidence of the variety of initial smaller failures that occurred before the major failure with the increase and decrease of the load as the displacement continues. Note that the load peak after each failure tends to be lower than the previous spike, meaning that the scaffolding had already reached its peak load and had started to fail. This is why the test was stopped after a major failure occurred because the scaffolding would only continue to weaken until it failed completely.

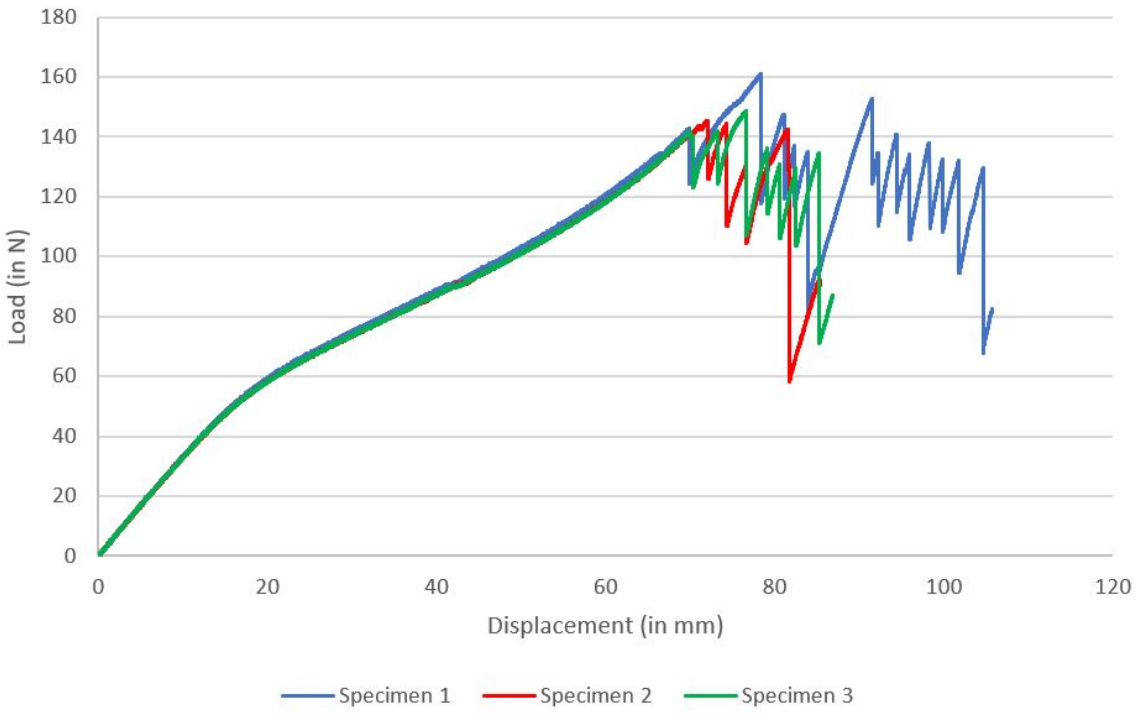

Figure 108: Load-displacement curves for tensile tests of Ti6Al4V linked-spiral parallel-axis samples.

Skew-axis linked-spiral samples

The final Ti6Al4V samples are the linked-spiral skew-axis specimens seen in Figure 109 below. As with the previous tests, the image of the first specimen (i) is at the top, followed by those of the second (ii) and third (iii) specimens. All three specimens show similar deformation with elongation until failure starts occurring. The specimens expand horizontally during elongation, confirming that the scaffolding has auxetic properties in the skew-axis direction. Similar properties were seen in the preliminary polymer test; however, the polymer scaffolding started to collapse before failure occurred, but the Ti6Al4V specimens were not able to collapse in on themselves before failure started. This was also seen in the other Ti6Al4V specimens, which means that scaling of the scaffoldings or the change from the polymer to the Ti6Al4V or a combination of both affected the behaviour of the scaffoldings.

i)

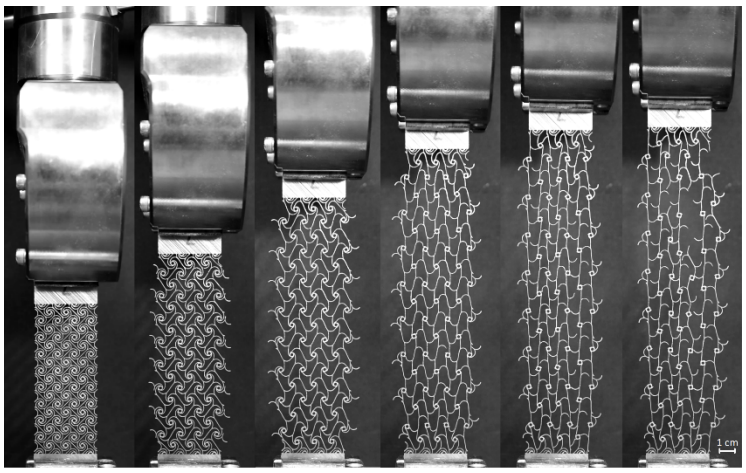

ii)

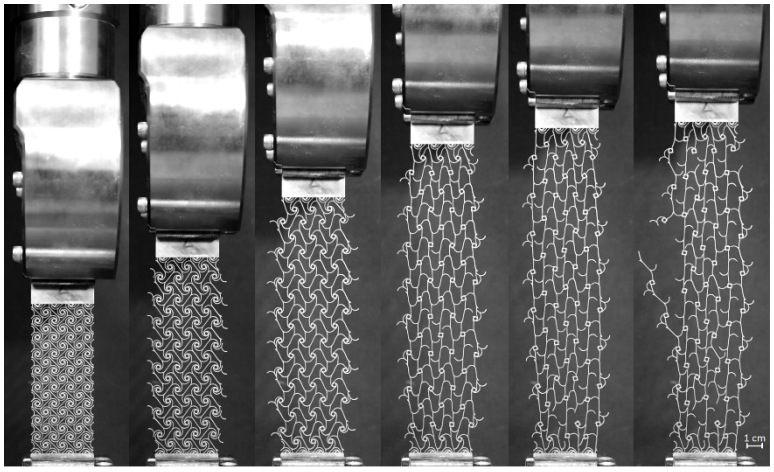

iii)

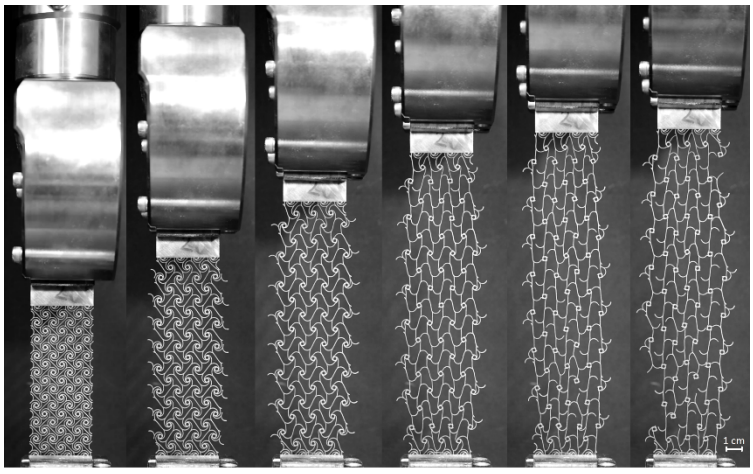

Figure 109: Tensile testing of the three Ti6Al4V skew-axis linked-spiral specimens: i) first specimen, ii) second specimen, iii) third specimen and a) neutral state of the specimen before the tensile test, b-d) deformation of the specimen during elongation, e) specimen at the moment before failure, f) specimen after failure had occurred.

At the failure points of the specimens, there is a similar occurrence in the parallel-axis that was seen in the skew-axis, where a large variety of smaller failures between links happened before

the major failure occurred. The initial smaller failures are highlighted in blue, and the major failure link breaks in red in Figure 110 below. When comparing the number of initial failures to those of the parallel-axis, there seem to be relatively more failures, and they are seen all over the specimens, not just in the centre or at the end of the specimens, as was found in the parallel-axis. The initial failures seem to be mainly between horizontally adjacent nodes. The link breaks that occurred due to the major failure are not concentrated in a general area, as noted in the parallel-axis, but are distributed across the specimen, likely due to the initial failures being spread all over the specimen and weakening the whole specimen. Finally, the major failure breaks also seem to be mainly between horizontally adjacent nodes; most likely, this is the result of the elongation rotating the nodes, pushing the adjacent horizontal nodes apart past the point where the link can bend, thus causing the link to tear off.

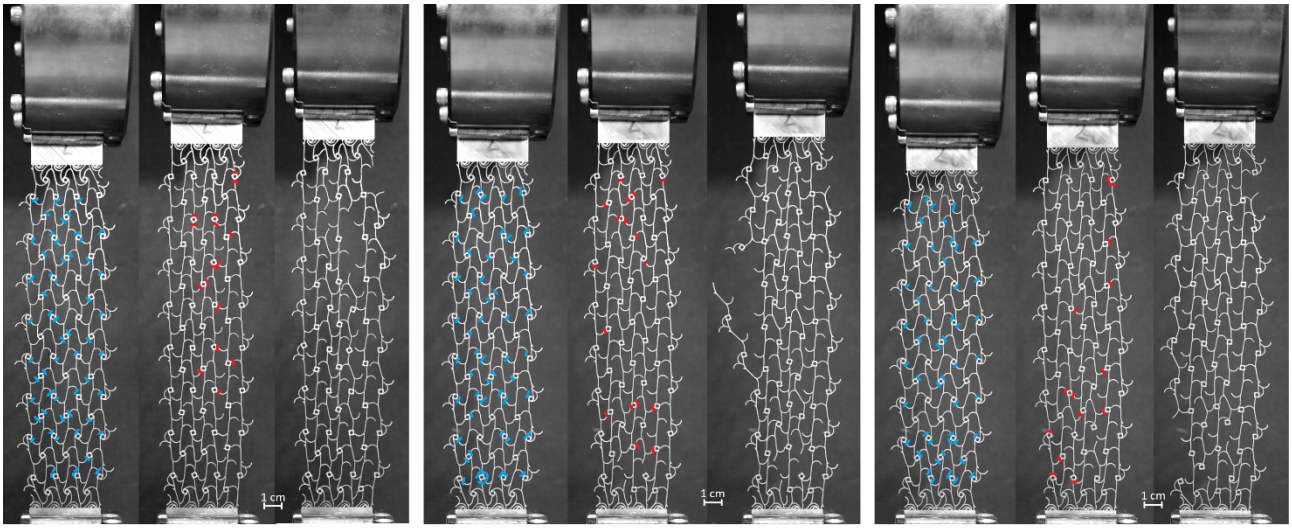

Figure 110: Failure points of Ti6Al4V skew-axis linked-spiral specimens (blue lines indicate where the specimen failed before the major failure occurred, and red lines indicate the points that failed during the occurrence of the major failure): i) first specimen, ii) second specimen, iii) third specimen.

The graph in Figure 111 below shows the tensile test results of the Ti6Al4V linked-spiral skew-axis specimens. The first specimen (light blue) reached a peak load of 365.8 N at a displacement of 111.5 mm before experiencing a major failure. The second specimen (orange) reached a peak load of 353.4 N, a displacement of 112.8 mm, before experiencing a major failure. Lastly, the third specimen (purple) reached a peak load of 331.8 N at a displacement of 110.7 mm before experiencing a major failure. The three specimens had an identical load-displacement curve until the initial failures started at around 73 mm of displacement. All three specimens reached their peak loads within a displacement range of 3 mm, which is relatively close. Curves

on the graph are relatively smooth until the initial failures start to occur, where the curves start to slowly develop larger and larger spikes until a major failure occurs. All the spikes are correlated to a break between two nodes, and as the elongation continues, more failures occur between nodes causing bigger and bigger spikes.

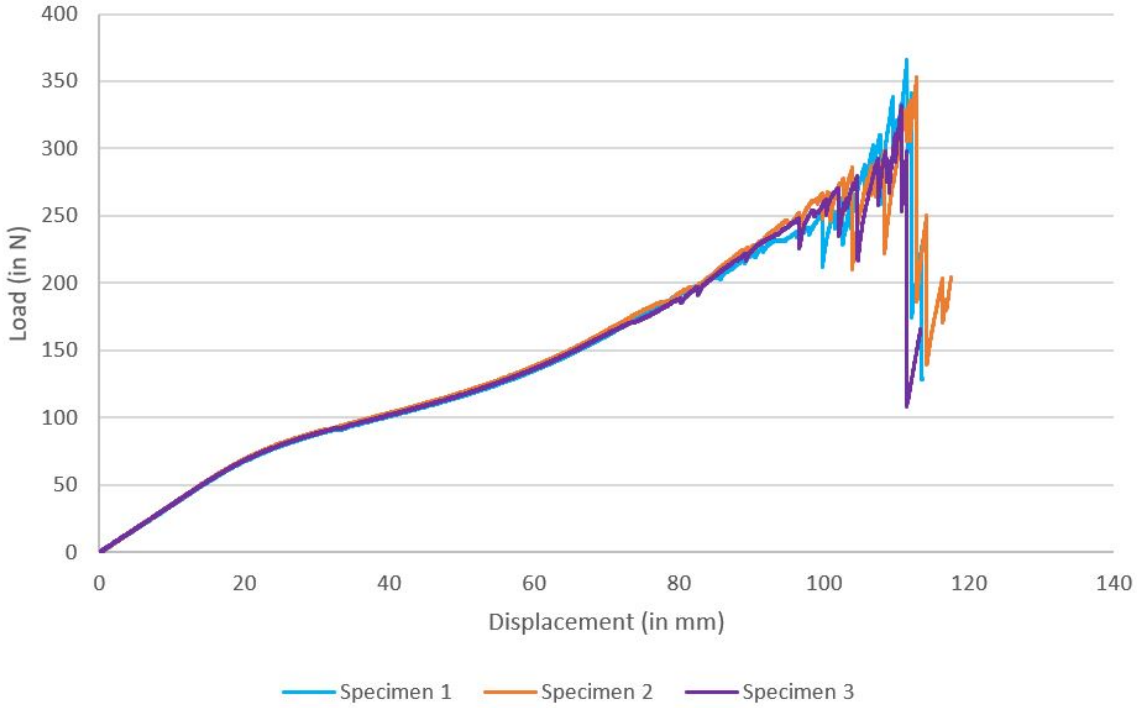

Figure 111: Load-displacement curves for tensile tests of Ti6Al4V linked-spiral skew-axis samples.

Linked-spiral parallel- and skew-axis comparison

The graph below in Figure 112 shows both the linked-spiral parallel- and skew-axis specimen results. Comparing the load-displacement curves of the two-axis specimen shows that the curves are the same for the 15 mm of elongation. After that, the parallel-axis curve load growth starts to decrease while the skew-axis curve continues to grow for 15 mm before its load growth also starts to decrease. The curves then start to run almost parallel until the specimens start to fail. The data shows that the skew-axis reached a higher peak load and longer, more extended displacement, even though the skew-axis specimens seem to have had more failure points. Furthermore, none of the linked-spiral specimens suffered a complete failure even though they were under more load than the wide-bow specimens. Most likely, this is due to the linked-spiral scaffolding structure being stronger and able to handle the chain reaction failures better, allowing it to last longer and withstand more load.

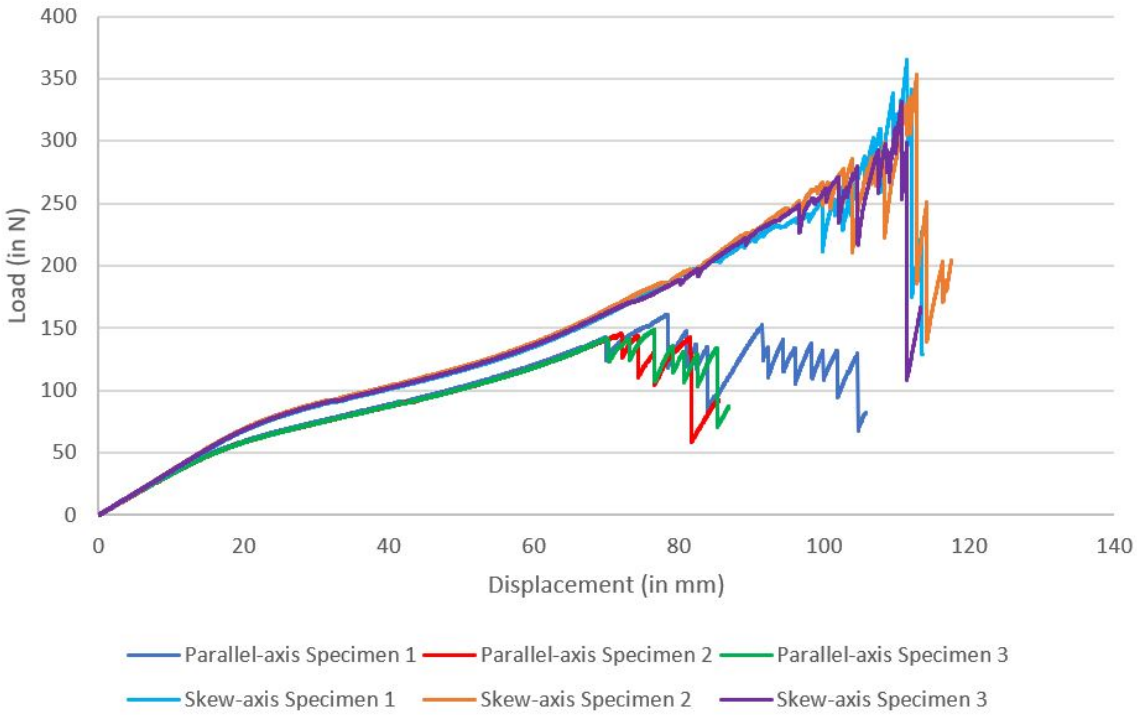

Figure 112: Load-displacement curves for tensile tests of linked-spiral parallel- and skew-axis samples.

5.2.4. Ti6Al4V tensile test data collected

Table 11 below sets out the data collected from the tensile testing of the Ti6Al4V specimens for each scaffolding type and axis direction. The wide-bow Y-axis reached the longest displacement, with the third specimen reaching a displacement of 207.5 mm at peak load. The average displacement for the wide-bow Y-axis specimens was 192.13 mm. However, it is important to note that compared to the differences between other specimen groups, the first wide-bow Y-axis specimen has a relatively large difference from its other two specimens, meaning the first specimen could be faulty. Furthermore, the linked-spiral skew-axis was able to withstand the highest peak load, with the first specimen reaching a peak load of 365.8 N at a displacement of 111.5 mm before starting to fail. The average peak load of the skew-axis specimens was 350.33 N at a displacement of 111.67 mm and is more than double the peak load of the closest specimens, which was the linked-spiral parallel-axis with an average peak load of 151.67 N at a displacement of 75.6 mm.

Finally, comparing the Ti6Al4V test data with the polymer test data in Table 9 in section 4.2.10, it is noted that the Ti6Al4V specimens can withstand higher peak loads which is correct as they are made from a stronger material. Furthermore, the Ti6Al4V specimens have a lower displacement distance than that of the polymer specimens, and this is likely due to the polymer

material allowing for more elongation in the material itself, where the Ti6Al4V would tear or fracture more easily. The following observation can be made on the auxetic behaviour of the scaffoldings; from the preliminary polymer test, the wide-bow X-axis was only slightly auxetic, but the Ti6Al4V specimens were fully auxetic as they did not collapse in on themselves. The wide-bow Y-axis Ti6Al4V specimens performed similarly to the polymer specimens as they did not show any auxetic behaviour. The linked-spiral parallel-axis Ti6Al4V specimens also performed similarly to their polymer specimens. They both showed fully auxetic behaviour. Lastly, the linked-axis skew-axis specimens were only slightly auxetic in the polymer test but fully auxetic in the Ti6Al4V test.

Table 11: Data collected from Ti6Al4V tensile tests

Sample		Number of links per node	Length of the link, mm	Maximum loading, N	Displacement at the break, mm	Deformation behaviour
Wide-bow	X-axis	3	13.2	92.5	175.5	Fully auxetic
				90.3	173.5	Fully auxetic
				102.8	189.1	Fully auxetic
				95.2	179.37	Fully auxetic
	Y-axis	3	13.2	47.9	165.5	Non- auxetic
				65.6	203.4	Non- auxetic
				67.0	207.5	Non- auxetic
				60.17	192.13	Non- auxetic
Linked-spiral	Parallel-axis	4	20.5	160.9	78.4	Fully auxetic
				145.5	72.0	Fully auxetic
				148.6	76.5	Fully auxetic
				151.67	75.63	Fully auxetic
	Skew-axis	4	20.5	365.8	111.5	Fully auxetic
				353.4	112.8	Fully Auxetic
				331.8	110.7	Fully Auxetic
				350.33	111.67	Fully auxetic

5.2.5. Summary

By comparing the results from the simulations to those from the tensile tests, it can be deduced that firstly, the stress concentrations on the simulations generally correlated to the points where the scaffolding failed. This means that the simulations could be used to simulate likely points where failure will occur. Secondly, the simulations were relatively accurate, coming within less than 10% deviation of the actual elongation length and always being more than the actual length, except for the linked-spiral skew-axis, which was out by more than 30% and less than

the actual value from the tensile test. Furthermore, the simulated deformation was quite accurate compared to the actual deformation observed in the tensile test, which means the simulations can be used to form a general idea of the deformation of the scaffoldings. Lastly, a load of 1000 N was used on the scaffoldings in the simulations. However, values obtained from the tensile tests showed actual loads ranging from 60 N to 350 N. Furthermore, the maximum stress calculated by the simulations show that the wide-bow specimens had higher stress concentrations, meaning that they would fail under a lower load, which correlates with the results obtained from the tensile test.

On the other hand, the difference between the loads on the two axes for each scaffolding is much bigger than the differences between the maximum stress calculated by the simulations. Furthermore, taking the results from the preliminary test into account in section 4.2.1., it is most likely that the maximum load calculated on the simulations would not correlate with the results from the tensile test. These simulations are not sufficiently reliable to calculate the maximum load that the AM scaffoldings could withstand due to the anisotropy of mechanical properties of L-PBF parts, its specific microstructure, and possible defects such as porosity and rough surface (Yadroitsev et al, 2021).

Chapter 6: Conclusions and future research

This study investigated the development of DRS produced by AM. Several methods were investigated to create the DRS, and various designs were studied. Six of the designs were fabricated in polymer and underwent preliminary testing. Thereafter, two designs were fabricated from Ti6Al4V ELI alloy and tested along different directions to observe their properties, deformation behaviour and failure.

First, a literature review was done on relevant topics and methods that could be beneficial in developing the DRS. Topology optimisation and lattice structures seemed promising. They are methods of creating the optimal geometrical structures for a specific situation in order for the part to have mechanical properties that would be the most efficient for the given boundary conditions. Compliant mechanisms refer to the method of utilising the elastic deformation of a rigid material by decreasing the thickness and increasing the length of the material to transfer movement, force, or energy. Metamaterials are artificially composed materials engineered to exhibit properties that often do not occur in nature and are typically arranged in a repeating pattern that is on milli-, micro- or even nanometer scale, allowing materials that show zero or negative mechanical parameter values such as auxetic materials (materials with a negative Poisson's ratio).

Creating a scaffolding that possesses elements of topology optimisation, lattice structures, compliant mechanisms and metamaterials on a milli- to micrometre scale would be difficult with any conventional subtractive manufacturing processes. Therefore, AM was selected for the fabrication of the DRS. L-PBF is an AM process and was selected to fabricate the metallic scaffolding specimens as it possesses the required accuracy and capability of fabricating in metallic materials. The SLS AM process was selected for the preliminary test of the different scaffolding designs as it is relatively similar to the L-PBF AM process but utilises polymer materials.

For the materials, Ti6Al4V and PA 2200 was chosen for the final and preliminary tests, respectively. Ti6Al4V is a titanium alloy, the most popular material used for medical implants. It has an outstanding strength-to-weight ratio, fatigue resistance, high corrosion resistance and biocompatibility, making it perfect for implants. PA 2200 is based on polyamide 12 powder but has a higher crystallinity and melting point than polyamide 12. PA 2200 also contains stabilisers against heat and oxidation, making it a good choice for medical devices and implant material.

Six initial designs were selected for the scaffolding designs to undergo preliminary testing. These designs consist of two different categories, with three designs in each category. The first is the hexagonal category with single patterns consisting of six nodes arranged in a hexagon. The second is the square category which has a single pattern of four nodes in a square arrangement. These patterns were chosen as they can repeat infinitely in all directions. For the tests, the structures would need to be deformed in a single direction or axis; therefore, it was decided to make specimens in two directions.

For the hexagonal scaffoldings, the directions chosen were the X- and Y-axis (with a 90° offset angle), with the square scaffolding identical in the X- and the Y-axis. Therefore, a direction parallel to the X- or Y-axis was selected with a skew direction that offset at an angle of 45° to the X- or Y-axis. This resulted in a total of 12 specimens for the preliminary tests. After the preliminary tests, the two most promising scaffolding designs were selected and converted to metallic designs. These specimens were tested in the two different axes, but three of each specimen were tested to determine the specimen consistency and reliability.

Numerical simulations were done and analysed to be compared with real-life test data done by tensile testing the specimens to determine their load-displacement properties and their mechanical deformation with elongation. From the preliminary tests, the wide-bow specimens showed the longest elongation and the lowest peak loads, making them the most compliant of the scaffoldings and therefore selected as one of the final scaffoldings. The linked-spiral scaffolding showed the most auxetic behaviour and potential to be DRS and was selected as the second of the final scaffoldings. From the Ti6Al4V tensile tests, the wide-bow specimens still had the longest elongation and lowest peak load but showed auxetic behaviour, unlike the preliminary tests with plastic samples. The linked-spiral specimens could withstand higher loads and were more auxetic than the other patterns.

Literature review shows that the human skull is about 90% fully developed by the age of five to seven years and is only left with 10% growth until the late teens or early twenties when the skull is fully developed (Salam et al., 2018; Cabraja et al., 2009; Kwiecien et al., 2018). This means that there would most likely only be a 10% growth in the cranial fracture size, but this would depend on the shape of the fracture if the skull grows slower or faster in different directions and how much bone would grow into the fracture. A cranial fracture of 100 mm in diameter with a growth of 10%, the scaffolding would need to elongate roughly 10 mm. From the force-over-displacement graphs, it was found that for the wide-bow, there would be a tensile force of around 4 N on the skull, and for the linked-spiral, a tensile force of around

40 N. However, the thickness of the scaffoldings can be changed to be below the level that bone resorption starts to occur, or it can be increased to provide more protection if the load is sufficiently below the bone resorption load.

Future work entails further investigation into the behaviour of the scaffoldings when they are subjected to elongation in multiple directions at once. The auxetic properties mean that the scaffoldings would expand in the direction perpendicular to elongation. However, if the scaffolding expands in both directions, would the load resisting elongation be less due to the auxetic behaviour, and how would the scaffoldings mechanically deform under these circumstances? Furthermore, investigations on impact forces perpendicular to the scaffolding plane could be done to see how the force is transferred to the mounting points, how much the scaffolding deforms perpendicular to the scaffolding plane and the scaffolding mechanical deformation during impact. This could go even further by fixing the scaffolding on a surface that is not flat (e.g., the shape of a skull) and testing the scaffolding properties and behaviours with different impact forces.

Finally, three-dimensional DRS can be developed and tested, going further than extruded two-dimensional geometries, and allowing for even more complex behaviours.

REFERENCES

3D Printing Systems SA, 2021. UP Mini ES. [online] Available at: https://3dprintingsystems.co.za/3d-printers/up-mini-2-es/ [Accessed 2 June 2021].

Al-Tamimi, A.A., Peach, C., Fernandes, P.R., Cseke, A. and Bartolo, P.J., 2017. Topology optimisation to reduce the stress shielding effect for orthopedic applications. Procedia Cirp, 65, pp.202-206.

allevi3d.com, (2020). Infill Pattern Options In Slic3r. [online] Available at: https://www.allevi3d.com/infill-options-in-slic3r/ [Accessed 18 June 2020].

AMFG, 2019. The additive manufacturing landscape, https://amfg.ai/wp-content/uploads/2019/08/The-Additive-Manufacturing-Landscape-2019_Whitepaper.pdf

ASTM, I.S.O., 2015. ASTM 52900-15 Standard Terminology for Additive Manufacturing—General Principles—Terminology. ASTM International, West Conshohocken, PA, 3(4), p.5.

Bansal, G., Singh, D.B., Virk, H.S., Devrani, A. and Bhandari, A., 2020. Microstructural characterisation, applications and process study of various additive manufacturing processes: A review. Materials Today: Proceedings.

Bellini, C., Berto, F., Di Cocco, V., Iacoviello, F.. Mocanu, L.P., Razavi, S. M. J., 2021. Additive manufacturing processes for metals and effects of defects on mechanical strength: a review. Procedia Structural Integrity. 33, pp. 498-508.

Benedetti, M., Du Plessis, A., Ritchie, R.O., Dallago, M., Razavi, S.M.J. and Berto, F., 2021. Architected cellular materials: A review on their mechanical properties towards fatigue-tolerant design and fabrication. Materials Science and Engineering: R: Reports, 144, p.100606.

Bertoldi, K., Vitelli, V., Christensen, J. and Van Hecke, M., 2017. Flexible mechanical metamaterials. Nature Reviews Materials, 2(11), pp.1-11.

Bijukumar, D.R., McGeehan, C. and Mathew, M.T., 2018. Regenerative medicine strategies in biomedical implants. Current Osteoporosis Reports, 16(3), pp.236-245.

Blakey-Milner, B., Gradl, P., Snedden, G., Brooks, M., Pitot, J., Lopez, E., Leary, M., Berto, F. and Du Plessis, A., 2021. Metal additive manufacturing in aerospace: A review. Materials & Design, p.110008.

Bobbert, F.S.L. and Zadpoor, A.A., 2017. Effects of bone substitute architecture and surface properties on cell response, angiogenesis, and structure of new bone. Journal of Materials Chemistry B, 5(31), pp.6175-6192.

Borzan, C.S.M., Dudescu, M.C., Ceclan, V., Trif, A., Ridzon, M. and Berce, P., 2016. PA 2200 vs PMMA: Comparison Between the Mechanical Proprieties Obtained for the 2 Biocompatible Materials. Mat. Plast, 53, p.1.

Bose, S., Ke, D., Sahasrabudhe, H. and Bandyopadhyay, A., 2018. Additive manufacturing of biomaterials. Progress in Materials Science, 93, pp.45-111.

Bourell, D.L., 2016. Perspectives on additive manufacturing. Annual Review of Materials Research, 46, pp.1-18.

Bückmann, T., Schittny, R., Thiel, M., Kadic, M., Milton, G.W. and Wegener, M., 2014. On three-dimensional dilational elastic metamaterials. New Journal of Physics, 16(3), p.033032.

Cabraja, M., Klein, M. and Lehmann, T.N., 2009. Long-term results following titanium cranioplasty of large skull defects. Neurosurgical Focus, 26(6), p.E10.

Challagulla, N.V., Rohatgi, V., Sharma, D. and Kumar, R., 2020. Recent developments of nanomaterial applications in additive manufacturing: a brief review. Current Opinion in Chemical Engineering, 28, pp.75-82.

Chang, B., Song, W., Han, T., Yan, J., Li, F., Zhao, L., Kou, H. and Zhang, Y., 2016. Influence of pore size of porous titanium fabricated by vacuum diffusion bonding of titanium meshes on cell penetration and bone ingrowth. Acta Biomaterialia, 33, pp.311-321.

Chen, F., Gu, Y., Xu, G., Cui, Y., Chang, H. and Zhou, L., 2020. Improved fracture toughness by microalloying of Fe in Ti-6Al-4V. Materials & Design, 185, p.108251.

Chen, N. and Frank, M., 2019. Process planning for hybrid additive and subtractive manufacturing to integrate machining and directed energy deposition. Procedia Manufacturing, 34, pp.205-213.

Chen, X., Ji, Q., Wei, J., Tan, H., Yu, J., Zhang, P., Laude, V. and Kadic, M., 2020. Light-weight shell-lattice metamaterials for mechanical shock absorption. International Journal of Mechanical Sciences, 169, p.105288.

Correa, J. and Ferreira, P., 2015. Analysis and design for rapid prototyping mechanism using hybrid flexural pivots. Procedia Manufacturing, 1, pp.779-791.

CRPM, 2021. EOSINT M 280. [online] Available at: http://www.crpm.co.za/wp-content/uploads/2017/07/EOS_M280_Metal-Machine.pdf [Accessed 2 June 2021].

Cuellar, J.S., Smit, G., Plettenburg, D. and Zadpoor, A., 2018. Additive manufacturing of non-assembly mechanisms. Additive Manufacturing, 21, pp.150-158.

Culbreath, C.J., Gaerke, B., Taylor, M.S., McCullen, S.D. and Mefford, O.T., 2020. Effect of infill on resulting mechanical properties of additive manufactured bioresorbable polymers for medical devices. Materialia, p.100732.

Daminabo, S.C., Goel, S., Grammatikos, S.A., Nezhad, H.Y. and Thakur, V.K., 2020. Fused deposition modeling-based additive manufacturing (3D printing): techniques for polymer material systems. Materials Today Chemistry, 16, p.100248.

Dana, H.R., Barbe, F., Delbreilh, L., Azzouna, M.B., Guillet, A. and Breteau, T., 2019. Polymer additive manufacturing of ABS structure: Influence of printing direction on mechanical properties. Journal of Manufacturing Processes, 44, pp.288-298.

Deckard, C.R., University of Texas System, 1989. Method and apparatus for producing parts by selective sintering. U.S. Patent 4,863,538.

Dede, E.M. and Hulbert, G.M., 2008. Computational analysis and design of lattice structures with integral compliant mechanisms. Finite Elements in Analysis and Design, 44(14), pp.819-830.

Dede, E.M. and Hulbert, G.M., 2009. Topology optimisation of structures with integral compliant mechanisms for mid-frequency response. Structural and Multidisciplinary Optimisation, 39(1), pp.29-45.

Dong, L., 2020. Mechanical responses of Ti-6Al-4V cuboctahedral truss lattice structures. Composite Structures, 235, p.111815.

Du Plessis, A., Broeckhoven, C., Yadroitsava, I., Yadroitsev, I., Hands, C.H., Kunju, R. and Bhate, D., 2019. Beautiful and functional: a review of biomimetic design in additive manufacturing. Additive Manufacturing, 27, pp.408-427.

EOS PA2200, 2021. Polyamide 12 Nylon. [online] Available at: https://www.eos.info/en/additive-manufacturing/3d-printing-plastic/sls-polymer-materials/polyamide-pa-12-alumide [Accessed 8 November 2021].

EOS SLS, 2021. EOS P 396. [online] Available at: https://www.eos.info/en/additive-manufacturing/3d-printing-plastic/eos-polymer-systems/eos-p-396 [Accessed 2 June 2021].

EOS, 2021, Feinpolyamide PA 2200 for EOSINT P, [online] Available at: https://www.adelaide.edu.au/writingcentre/sites/default/files/docs/harvard-referencing-guide.pdf [Accessed 26 May 2021].

Evans, K.E., Nkansah, M.A., Hutchinson, I.J. and Rogers, S.C., 1991. Molecular network design. Nature, 353(6340), pp.124-124.

Fowler, R.M., 2012. Investigation of compliant space mechanisms with application to the design of a large-displacement monolithic compliant rotational hinge. [online] Available at: https://scholarsarchive.byu.edu/etd/3305 [Accessed 05 January 2022].

Gatt, R., Wood, M.V., Gatt, A., Zarb, F., Formosa, C., Azzopardi, K.M., Casha, A., Agius, T.P., Schembri-Wismayer, P., Attard, L. and Chockalingam, N., 2015. Negative Poisson's ratios in tendons: an unexpected mechanical response. Acta Biomaterialia, 24, pp.201-208.

Ghilan, A., Chiriac, A.P., Nita, L.E., Rusu, A.G., Neamtu, I. and Chiriac, V.M., 2020. Trends in 3D printing processes for biomedical field: opportunities and challenges. Journal of Polymers and the Environment, 28(5), pp.1345-1367.

Greaves, G.N., Greer, A.L., Lakes, R.S. and Rouxel, T., 2011. Poisson's ratio and modern materials. Nature Materials, 10(11), pp.823-837.

Hashemi, M.S., Kraus, K.H. and Sheidae, A., 2020. Optimum Design of Printable Tunable Stiffness Metamaterial for Bone Healing. arXiv preprint arXiv:2006.13496.

Housholder, R.F., Hico Western Products Co, 1981. Molding process. U.S. Patent 4,247,508.

Javaid, M. and Haleem, A., 2018. Additive manufacturing applications in medical cases: A literature based review. Alexandria Journal of Medicine, 54(4), pp.411-422.

Kiener, L., Saudan, H., Cosandier, F., Perruchoud, G. and Spanoudakis, P., 2019. Innovative concept of compliant mechanisms made by additive manufacturing. In MATEC Web of Conferences, vol. 304, p. 07002. EDP Sciences.

Kim, H.S. and Cho, Y.M., 2009. Design and modeling of a novel 3-DOF precision micro-stage. Mechatronics, 19(5), pp.598-608.

Kinnear, A, 2016, Direct metal laser sintering of multiple material structures for biomedical applications, Master thesis, Central University of Technology, Free State, Bloemfontein.

Kwiecien, G.J., Rueda, S., Couto, R.A., Hashem, A., Nagel, S., Schwarz, G.S., Zins, J.E. and Gastman, B.R., 2018. Long-term outcomes of cranioplasty: titanium mesh is not a long-term solution in high-risk patients. Annals of Plastic Surgery, 81(4), pp.416-422.

Kok, Y., Tan, X.P., Wang, P., Nai, M.L.S., Loh, N.H., Liu, E. and Tor, S.B., 2018. Anisotropy and heterogeneity of microstructure and mechanical properties in metal additive manufacturing: A critical review. Materials & Design, 139, pp.565-586.

Kolken, H.M. and Zadpoor, A.A., 2017. Auxetic mechanical metamaterials. RSC advances, 7(9), pp.5111-5129.

Kruis, J., Cosandier, F., Perruchoud, G., Kiener, L. and Saudan, H., 2019. 6 Design principles for SLM-based compliant mechanisms. [online] Available at: https://www.euspen.eu/knowledge-base/AM19111.pdf [Accessed 05 January 2022].

Kruth, J.P., Leu, M.C. and Nakagawa, T., 1998. Progress in additive manufacturing and rapid prototyping. CIRP Annals-Manufacturing Technology, 47(2), pp.525-540.

Kumar, S., 2003. Selective laser sintering: a qualitative and objective approach. Jom, 55(10), pp.43-47.

Le Roux, P.A., Laubscher, R.F. and Schubert, A., 2020. Machining for an increased fatigue life for a Ti-6Al-4V ELI component. Procedia CIRP, 87, pp.462-468.

Li, C., Pisignano, D., Zhao, Y. and Xue, J., 2020. Advances in medical applications of additive manufacturing. Engineering, 6(11), pp.1222-1231.

Ling, M., Cao, J., Howell, L.L. and Zeng, M., 2018. Kinetostatic modeling of complex compliant mechanisms with serial-parallel substructures: a semi-analytical matrix displacement method. Mechanism and Machine Theory, 125, pp.169-184.

Liu, Y., Dong, Z., Ge, J., Lin, X. and Liang, J., 2019. Stiffness design of a multilayer arbitrary BCC lattice structure with face sheets. Composite Structures, 230, p.111485.

López-Castro, J.D., Marchal, A., González, L. and Botana, J., 2017. Topological optimisation and manufacturing by Direct Metal Laser Sintering of an aeronautical part in 15-5PH stainless steel. Procedia Manufacturing, 13, pp.818-824.

Lu, T.J., Valdevit, L. and Evans, A.G., 2005. Active cooling by metallic sandwich structures with periodic cores. Progress in Materials Science, 50(7), pp.789-815.

Maconachie, T., Leary, M., Lozanovski, B., Zhang, X., Qian, M., Faruque, O. and Brandt, M., 2019. SLM lattice structures: Properties, performance, applications and challenges. Materials & Design, 183, p.108137.

Meiners, W., Wissenbach, K. and Gasser, A., 1998. Shaped body especially prototype or replacement part production. DE Patent, 19.

Mierzejewska, Ż.A., Hudák, R. and Sidun, J., 2019. Mechanical properties and microstructure of DMLS Ti6Al4V alloy dedicated to biomedical applications. Materials, 12(1), p.176.

Miranda, G., Sousa, F., Costa, M.M., Bartolomeu, F., Silva, F.S. and Carvalho, O., 2019. Surface design using laser technology for Ti6Al4V-hydroxyapatite implants. Optics & Laser Technology, 109, pp.488-495.

Mizzi, L., Mahdi, E.M., Titov, K., Gatt, R., Attard, D., Evans, K.E., Grima, J.N. and Tan, J.C., 2018. Mechanical metamaterials with star-shaped pores exhibiting negative and zero Poisson's ratio. Materials & Design, 146, pp.28-37.

MTS, 2021. MTS Criterion® Series 40 Electromechanical Universal Test Systems. [online] Available at: https://www.mts.com/cs/groups/public/documents/library/mts_006225.pdf [Accessed on 2 June 2021].

Nagesha, B.K., Dhinakaran, V., Shree, M.V., Kumar, K.M., Chalawadi, D. and Sathish, T., 2020. Review on characterisation and impacts of the lattice structure in additive manufacturing. Materials Today: Proceedings, 21, pp.916-919.

Nicolaou, Z.G. and Motter, A.E., 2012. Mechanical metamaterials with negative compressibility transitions. Nature Materials, 11(7), pp.608-613.

Niknam, H., Sarvestani, H.Y., Jakubinek, M.B., Ashrafi, B. and Akbarzadeh, A.H., 2020. 3D printed accordion-like materials: A design route to achieve ultrastretchability. Additive Manufacturing, 34, p.101215.

Overvelde, J.T.B., Shan, S. and Bertoldi, K., 2012. Compaction through buckling in 2D periodic, soft and porous structures: effect of pore shape. Advanced Materials, 24(17), pp.2337-2342.

Pal, S., Lojen, G., Kokol, V. and Drstvenšek, I., 2019. Reducing porosity at the starting layers above supporting bars of the parts made by Selective Laser Melting. Powder Technology, 355, pp.268-277.

Patel, A., Gupta. U.S., Gehlot, V., Jayant, J., M.L. Jain, 2018. A review of rapid prototyping in medical implants. International Journal of Advance Research in Science and Engineering, 7(4), pp. 244-258.

Patterson, A.E., Messimer, S.L. and Farrington, P.A., 2017. Overhanging features and the SLM/DMLS residual stresses problem: Review and future research need. Technologies, 5(2), p.15.

Peng, C., Tran, P., Nguyen-Xuan, H. and Ferreira, A.J.M., 2020. Mechanical performance and fatigue life prediction of lattice structures: Parametric computational approach. Composite Structures, 235, p.111821.

Peto, M., Ramírez-Cedillo, E., Hernández, A. and Siller, H.R., 2019. Structural design optimization of knee replacement implants for Additive Manufacturing. Procedia Manufacturing, 34, pp.574-583.

Portela, C.M., Greer, J.R. and Kochmann, D.M., 2018. Impact of node geometry on the effective stiffness of non-slender three-dimensional truss lattice architectures. Extreme Mechanics Letters, 22, pp.138-148.

Rahimizadeh, A., Nourmohammadi, Z., Arabnejad, S., Tanzer, M. and Pasini, D., 2018. Porous architected biomaterial for a tibial-knee implant with minimum bone resorption and bone-implant interface micromotion. Journal of the Mechanical Behavior of Biomedical Materials, 78, pp.465-479.

Rovira, D.S., Nielsen, H.M., Taboryski, R. and Bunea, A.I., 2021. Additive manufacturing of polymeric scaffolds for biomimetic cell membrane engineering. Materials & Design, p.109486.

Salam, A.A., Ibbett, I. and Thani, N., 2018. Paediatric cranioplasty: a review. Interdisciplinary Neurosurgery, 13, pp.59-65.

Sigmund, O., 1994. Design of material structures using topology optimisation. Doctoral dissertation, Technical University of Denmark.

Surjadi, J.U., Gao, L., Du, H., Li, X., Xiong, X., Fang, N.X. and Lu, Y., 2019. Mechanical metamaterials and their engineering applications. Advanced Engineering Materials, 21(3), p.1800864.

Szymczyk, P., Łabowska, M.B., Detyna, J., Michalak, I. and Gruber, P., 2020. A review of fabrication polymer scaffolds for biomedical applications using additive manufacturing techniques. Biocybernetics and Biomedical Engineering.

Van Der Walt, J.G. and Nsengimana, J., 2016. State of the art of Additive Manufacturing for polymeric medical implants. 17th Annual Conference of the Rapid Product Development Association of South Africa.

Vayre, B., Vignat, F. and Villeneuve, F., 2012. Designing for additive manufacturing. Procedia CIRP, 3, pp.632-637.

Vilardell, A.M., Takezawa, A., Du Plessis, A., Takata, N., Krakhmalev, P., Kobashi, M., Yadroitsava, I. and Yadroitsev, I., 2019. Topology optimisation and characterisation of Ti6Al4V ELI cellular lattice structures by laser powder bed fusion for biomedical applications. Materials Science and Engineering: A, 766, p.138330.

Wei, H., Wang, L., Niu, X., Deng, Y., Zhang, Y. and Cheng, J., 2018. Stiffness characteristics of a laser beam melted (LBM) additive-manufactured flexure mechanism. Procedia CIRP, 78, pp.144-148.

Wei, H., Wang, L., Niu, X., Zhang, J. and Simeone, A., 2018. Fabrication, experiments, and analysis of an LBM additive-manufactured flexure parallel mechanism. Micromachines, 9(11), p.572.

Wohlers, T.T., Campbell, I., Diegel, O., Huff, R., Kowen, J., 2019. Wohlers Report 2019: 3D printing and additive manufacturing state of the industry. Wohlers Associates, Inc., 369 p.

Wohlers, T.T., Campbell, I., Diegel, O., Kowen, J., Huff, R., Mostow, N., 2021. Wohlers Report 2021: 3D Printing and Additive Manufacturing: Global State of the Industry. Wohlers Associates, Inc., 374p.

Wu, J., Clausen, A. and Sigmund, O., 2017. Minimum compliance topology optimisation of shell–infill composites for additive manufacturing. Computer Methods in Applied Mechanics and Engineering, 326, pp.358-375.

Yadroitsau, I., 2008. Direct manufacturing of 3D objects by selective laser melting of metal powders. Doctoral dissertation, Saint-Etienne.

Yadroitsev, I., Krakhmalev, P., Yadroitsava, I. and Du Plessis, A., 2018. Qualification of Ti6Al4V ELI alloy produced by laser powder bed fusion for biomedical applications. JOM, 70(3), pp.372-377.

Yadroitsava, I., Du Plessis, A. and Yadroitsev, I., 2019. Bone regeneration on implants of titanium alloys produced by laser powder bed fusion: A review. Titanium for Consumer Applications, pp.197-233.

Yadroitsev, I., Yadroitsava, I., Du Plessis, A. and MacDonald, E., 2021. Fundamentals of laser powder bed fusion of Metals. Elsevier, Amsterdam, Netherlands, 654 p.

Yan, C., Hao, L., Hussein, A. and Young, P., 2015. Ti–6Al–4V triply periodic minimal surface structures for bone implants fabricated via selective laser melting. Journal of the Mechanical Behavior of Biomedical Materials, 51, pp.61-73.

Yang, L., Harrysson, O., West, H. and Cormier, D., 2012. Compressive properties of Ti–6Al–4V auxetic mesh structures made by electron beam melting. Acta Materialia, 60(8), pp.3370-3379.

Yang, S., Tang, Y. and Zhao, Y.F., 2015. A new part consolidation method to embrace the design freedom of additive manufacturing. Journal of Manufacturing Processes, 20, pp.444-449.

Yaragatti, N. and Patnaik, A., 2020. A review on additive manufacturing of polymers composites. Materials Today: Proceedings.

Yong, Y.K., 2016. A new preload mechanism for a high-speed piezoelectric stack nanopositioner. Mechatronics, 36, pp.159-166.

Yoon, C., Chang, M.J., Chang, C.B., Song, M.K., Shin, J.H. and Kang, S.B., 2018. Medial tibial periprosthetic bone resorption and its effect on clinical outcomes after total knee arthroplasty: Cobalt-chromium vs titanium implants. The Journal of Arthroplasty, 33(9), pp.2835-2842.

Yu, X., Zhou, J., Liang, H., Jiang, Z. and Wu, L., 2018. Mechanical metamaterials associated with stiffness, rigidity and compressibility: A brief review. Progress in Materials Science, 94, pp.114-173.

Yu, Y.Q. and Zhang, N., 2019. Dynamic modeling and performance of compliant mechanisms with inflection beams. Mechanism and Machine Theory, 134, pp.455-475.

Zhan, W., He, X., Yang, J., Lai, J. and Zhu, D., 2020, August. Optimal design method for 3-DOF planar compliant mechanisms based on mapping matrix constraints. Structures, vol. 26, pp. 1-5. Elsevier.

Zhang, W.N., Wang, L.Z., Feng, Z.X. and Chen, Y.M., 2020. Research progress on selective laser melting (SLM) of magnesium alloys: a review, Optik, pp. 163842 207.

Zhou, Y.H., Li, W.P., Zhang, L., Zhou, S.Y., Jia, X., Wang, D.W. and Yan, M., 2020. Selective laser melting of Ti–22Al–25Nb intermetallic: Significant effects of hatch distance on microstructural features and mechanical properties. Journal of Materials Processing Technology, 276, p.116398.

Zhu, B., Zhang, X., Zhang, H., Liang, J., Zang, H., Li, H. and Wang, R., 2020. Design of compliant mechanisms using continuum topology optimisation: A review. Mechanism and Machine Theory, 143, p.103622.

Zindani, D. and Kumar, K., 2019. An insight into additive manufacturing of fiber reinforced polymer composite. International Journal of Lightweight Materials and Manufacture, 2(4), pp.267-278.